Microphase-separated Structure and Mechanical Properties of Cycloaliphatic Diisocyanate-based Polythiourethanes, Polyurethanes, and Polyurethane Ionomers

ラーマワティ

https://doi.org/10.15017/4060106

出版情報：九州大学, 2019, 博士（工学）, 課程博士
バージョン：
権利関係：

Microphase-separated Structure and Mechanical Properties of Cycloaliphatic Diisocyanate-based Polythiourethanes, Polyurethanes, and Polyurethane Ionomers

脂環式ジイソシアネートを用いたポリチオウレタン、ポリウレタンおよびポリウレタンアイオノマーのミクロ相分離構造と力学特性に関する研究

RAHMAWATI

August, 2019

Microphase-separated Structure and Mechanical Properties of Cycloaliphatic Diisocyanate-based Polythiourethanes, Polyurethanes, and Polyurethane Ionomers

A Thesis Submitted

In Partial Fulfillment of the Requirements

For the Degree of

Doctor of Engineering

By

Rahmawati

to the

DEPARTMENT OF CHEMISTRY AND BIOCHEMISTRY

GRADUATE SCHOOL OF ENGINEERING

KYUSHU UNIVERSITY

Fukuoka, Japan

August, 2019

TABLE OF CONTENTS

LIST OF FIGURES

LIST OF TABLES

Chapter 1

Introduction

1.1 Introduction

There has been an increasing interest in the development of materials in all aspects of life. Among them, polyurethanes (PUs) have played important roles in our daily life. PUs are unique materials having many superior properties, such as high Young's modulus, large tensile strength, and large elongation at break, which enables them to be modified for various purposes. For that reason, PUs have been extensively used in a wide range of applications, from automotive, electronics, textile, and medical application.[1-1~5)] Hitherto, numerous research on PUs have been carried out in order to either obtaining more superior properties of PUs or exploring novel potential applications of PUs. For example, the modification of PUs by using dithiol chain extender to form polythiourethanes (PTUs) have been scrutinized to obtain materials with good optical and adhesive properties.[1-6~8)] In addition, polyurethane ionomers (PUIs) have also been considered to be used as adhesives, coatings, conductive polymers and biomedical elastomers.[1-9~12)] The main features of PUs, PTUs, and PUIs are their specific interactions that will trigger the interacting moieties to spontaneously form aggregates which crosslink the polymer, and improve their mechanical properties.[1-13~15)] Therefore, an insight into the microphase-separated structure-property relationship is

essential for both adjusting the material properties and expanding their potential applications.

PU elastomers are produced typically by the reaction between polyol, diisocyanate and small molecule diol or diamine chain extender. Figure 1.1 shows chemical reactions involved in polyurethane preparation.

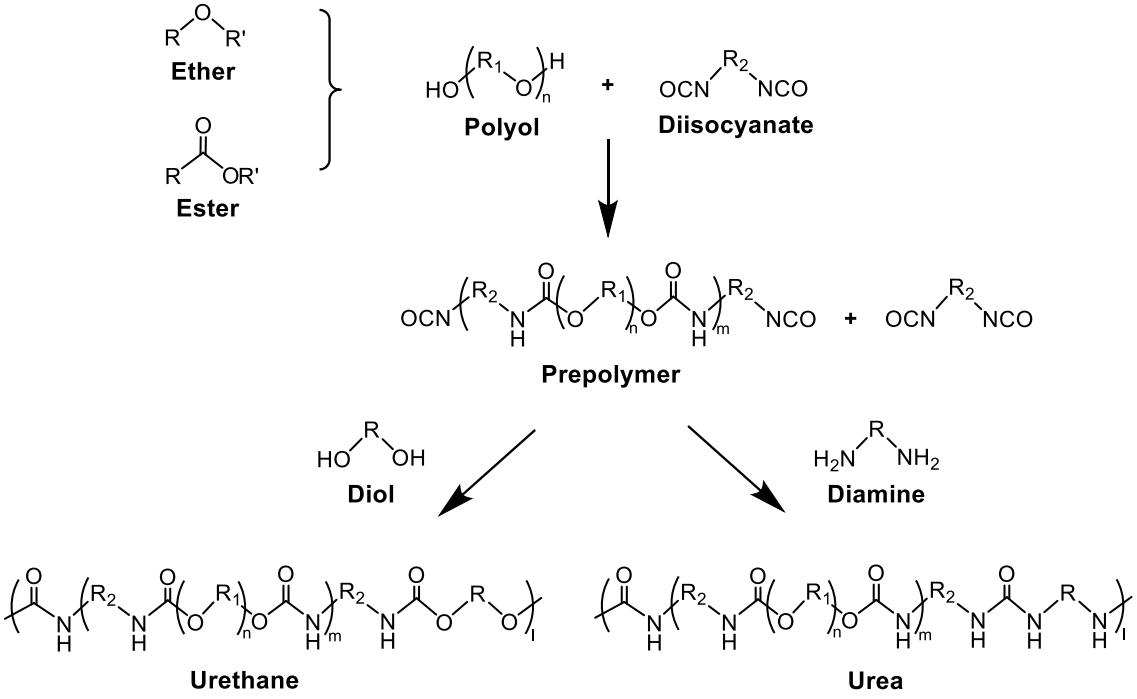

Figure 1.1 Chemical reactions involved in polyurethane preparation. [1-2)]

The resulting polymer may be considered as a copolymer of polyol and diisocyanate-chain extender sequences called soft segment and hard segment, respectively. The thermodynamic incompatibility between the hard and soft segments induces microphase separation in the PUs. The hard segments tend to

associate into domains which act as physical crosslinking points and filler particles in the soft segment matrix. The degree to which these two copolymers phase separate significantly influence the mechanical properties of the materials.[1-16~19] Whereas, the degree of phase separation depends on the interaction parameter and the degree of polymerization.[1-20] By varying the chemical structure, composition of the starting components, and the preparation conditions, PUs with broad-spectrum properties can be obtained.[1-21~22]

One of the most essential component of a PU is diisocyanate, which can be either aromatic or aliphatic. The most important aromatic diisocyanates are 4,4-diphenylmethane diisocyanate (MDI) and 2,4-tolylene diisocyanate (TDI), which can be seen in Figure 1.2. MDI has been applied to various polyurethane products, especially, elastomer which requires high tensile strength, modulus and thermal stability.[1-23,24] This is because the hard segment chains can easily crystallize and form hydrogen bonds in the hard segment domains. However, these aromatic diisocyanate-based PUs turn yellow when exposed to light for a long time due to the formation of a quinoid structure of aromatic ring. PUs based on aliphatic and cycloaliphatic diisocyanates are used to overcome this problem. However, the

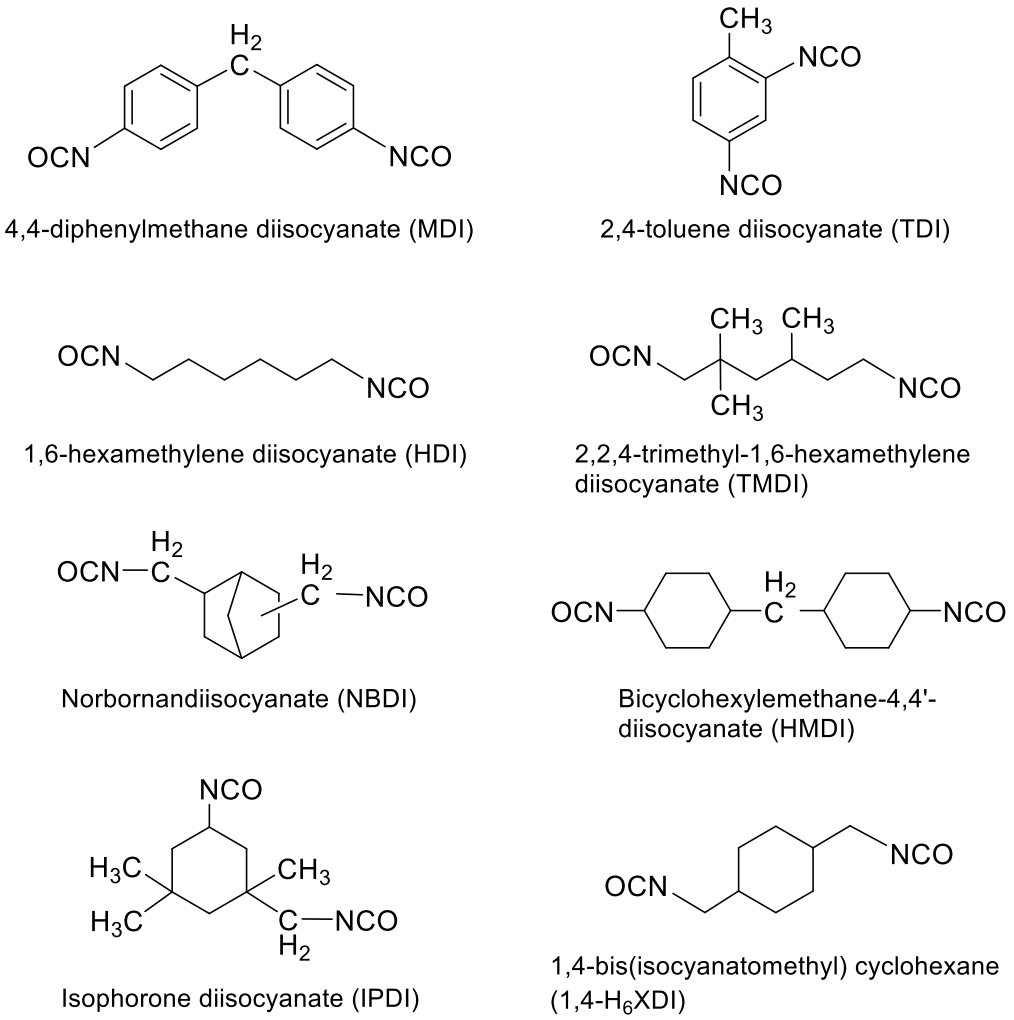

Figure 1.2 Structure of diisocyanates.

development of aliphatic diisocyanate-based PUs does not satisfy the industrial demands. The 1,6-hexamethylene diisocyanate (HDI) usually give hard materials due to its high crystallizability. The 2,2,4-trimethyl-1,6-hexamethylene diisocyanate (TMDI), isophorone diisocyanate (IPDI), and norbornandiisocyanate (NBDI) possess asymmetric structure, whereas the bicyclohexylmethane-4,4'-diisocyanate (HMDI) is

mixture of isomers. This leads to inferior mechanical properties due to weak cohesive force between the hard segment chains.[1-22,25,26)]

The 1,4-bis(isocyanatomethyl) cyclohexane (1,4-H_6XDI) is expected to have a good mechanical properties and do not turn yellow when exposed to light. The high symmetry of 1,4-H_6XDI leads to the well-organized hard segment domains, resulting in superior mechanical properties compared to MDI-based PUs, even though their degree of overall microphase separation is almost the same.[1-27)] In addition, the PUs properties can be tailored by modifying the hard segment content. However, there have no report on the effect of methylene length of the chain extender on microphase-separated structure and mechanical properties of 1,4-H_6XDI-based PUs although it can be predicted according to Born et al.[1-28)] In this thesis, the effect of methylene length of the chain extender of 1,4-H_6XDI-based PU is investigated quantitatively in terms of the degree of microphase separation and mechanical properties.

As well as PUs, PTUs are comprised of the soft and hard segments, which tend to form a microphase-separated structure in the nanometer scale due to their thermodynamic incompatibility. This microphase-separated structure strongly influences the mechanical properties of PTUs. Only a few works

on the physical properties of PTUs have been reported so far. Li et al.[1-6] reported that PU and PTU produced from HDI trimer and 1-hexanol or 1-hexanethiol show approximately equivalent physical and mechanical properties as a result of similar extent of hydrogen bonding. Besides, polythiourethanes have higher refractive index values compared to their polyurethane counterpart. Furthermore, Shin et al.[1-29] found that the hard and soft segment molecular weight and ratio, and the hard segment chemical structure have a strong influence on the microphase separation and correlated with tensile properties of the PTUs. However, there have been no study on the effect of diol and dithiol chain extender on the microphase-separated structure and mechanical properties of 1,4-H_6XDI-based PUs and PTUs.

Another important topic in the PTUs subject is their morphological dynamics during deformation. The majority of existing literature on PUs has mainly focused on studying the structure-property relationship in order to obtain more superior materials.[1-16,30] Several studies involve a comprehensive analysis of the deformation behavior. Bonart et al. studied the morphology development of PUs under uniaxial extension and found that the morphology of the hard segment domains is diverse and orientation of hard segments along the stretch direction develops under the applied strain.[1-13,31] Seymour et

al.[1-32] reported that the orientation of hard segments is affected mainly by the hard segment length, while soft segment orientation is less affected by polymer composition. Besides, the hard segment orientation is also influenced by the type of ordering inside the hard segment domains. In addition, Estes et al.[1-33] found that the hard segment domains have a tendency to retain a partially oriented conformation after the stress is removed, whereas the soft segments return to an unoriented state. Moreover, Kimura et al.[1-34] studied the hard segment domain orientation by small-angle polarized light scattering. Lee et al.[1-35] reported the uniaxial deformation of PU elastomers using Fourier transform infrared (FTIR) and synchrotron small-angle X-ray scattering (SAXS) methods and found that the deformation behavior of PU elastomers depends on the orientation of the hard segment domains in the initial state.

In this thesis, the structure-properties relationship of 1,4-H_6XDI-based PTUs during uniaxial deformation will be discussed, in order to attain rationale for engineering and design of the PTUs for specific applications. Furthermore, the X-ray absorption fine structure (XAFS) method is utilized, in addition to *in situ* SAXS/WAXD method, to obtain more detail information about the structural parameter in the short-range order.

Another type of PU that will be discussed in this thesis is the PU ionomer. PU ionomer can be defined as a copolymer consisting of a backbone with a minority of the repeat units carrying acid or tertiary nitrogen groups that are completely or partially neutralized or quaternized to form salts. The energetic incompatibility between polar ionic groups and the nonpolar polymer back bond generates aggregation of ionic groups into ionic rich domains, called ion multiplets, which may grow larger become ion clusters. This aggregates act as reinforcing fillers, thermally reversible crosslinks, and ion transport pathways that have a prominent effect on the mechanical and transport properties of PUIs.[1-36~39] The morphology and properties of ionomers are influenced by several factors, including, among others, the degree of ionization, the compatibility of the polymer backbone and the ionic groups, the nature of the pendant anion, and the neutralizing cation.[1-38,40~42]

Investigation of the morphology of PU ionomers was conducted using X-ray scattering, which is a powerful method for studying the nanoscale morphology of ionomers. Several models have been proposed to interpret the scattering data of ionomers.[1-40,43] The most widely accepted scattering model is the Yarusso-Cooper modified hard-sphere model. This model suggests that the ionomer peak arises from the interparticle

scattering between the spherical ionic aggregates arranged with liquid-like order in the lower electron density matrix. The modification of Yarusso-Cooper model is proposed by Kinning and Thomas[1-44] and Ding et al.[1-45], which combine the Percus-Yevick total correlation function[1-46] that account the correlation between all particles in the system into the structural factor instead of three-body interference function.[1-47] Although both models fit the ionomer SAXS peak well, Percus-Yevick total correlation function was shown to be more suitable for systems of high packing fraction.[1-44] However, there have been no report on the effect of degree of neutralization on the microphase-separated structure and mechanical properties of PU ionomers consisting non-ionic hard segment domains.

1.2 Objective

Regardless of the relative importance of PUs, PTUs, and PUIs, there has been limited research directed toward understanding the microphase separation in these materials and the role of uniaxial elongation on the microphase-separated structure of PTUs. The microphase separation has been studied using a number of techniques, most notably small-angle X-ray scattering.[1-17,18] SAXS is one of the few techniques that allow one to get representative quantitative information about the

structure, obtained from an average over macroscopic samples. Generally, features on a length scale of 1 to 100 nm are accessible by SAXS, which corresponds to the typical size for the structure parameters of semi crystalline polymers. SAXS is, therefore, the method of choice if detailed quantitative information about the semi crystalline morphology is desired.[1-48] SAXS also allows dynamic studies of polymer films and fibers during tensile deformation, which give important information on the changes of structure and morphology during deformation that can be related to the macroscopic properties of polymers. In addition, several models of the microstructure of ionomers derived from the analysis of SAXS data. For instance, the intraparticle interference models proposed by MacKnight et al.[1-43] and the interparticle interference models proposed by Yarusso and Cooper.[1-40]

Despite the remarkable contribution of the existing literature on the microphase-separated structure and mechanical properties of PUs, PTUs, and PUIs, it has some noteworthy limitations. For instance, most of the existing literature on PTU attempts to find the synthesis route, enhance the refractive index, and observe the potential application.[1-6~8,49] However, fundamental understanding of the structure-property relationship is required for engineering and design of PTUs for specific

applications.

The objective of this thesis, therefore, is to study the relationship between the microphase-separated structure and mechanical properties of 1,4-H_6XDI-based PTUs, PUs, and PUIs.

1.3 Thesis structure

The discussion about the structure-property relationship of polyurethane family in this thesis is divided into several parts, as follows. Chapter 1 describes the background, purpose, and composition of this research. In Chapter 2, the microphase separated structure and mechanical properties of cycloaliphatic diisocyanate-based PTU elastomers are evaluated and compared to PU elastomers. The effect of methylene length of the chain extenders on the microphase-separated structure and mechanical properties of PTU and PU were also examined. In Chapter 3, the uniaxial deformation behavior of PTU elastomers was studied using in-situ SAXS/WAXD and XAFS methods, including the influence of methylene length of the chain extenders on deformation behavior. The structure-property relationships of cycloaliphatic diisocyanate-based polyurethane ionomers consisting non-ionic hard segment domains were described in Chapter 4. Finally, the discussion about structure-property relationships of PTUs, PUs and PU ionomers will be concluded

in Chapter 5. The framework of this thesis is provided in Figure 1.3.

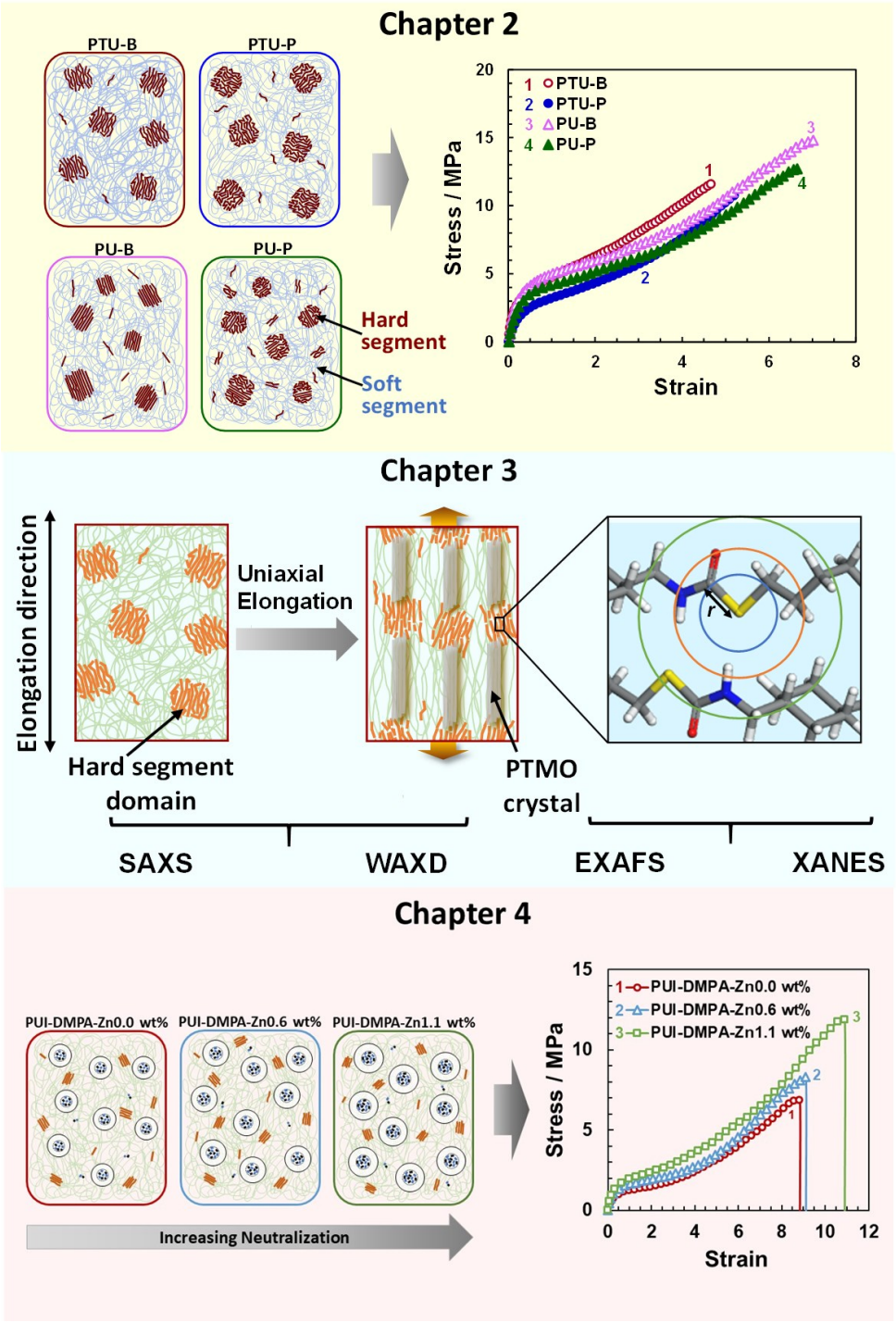

Figure 1.3 Framework of the thesis.

References

1-1) A. Takahara, J. Tashita, T. Kajiyama, M. Takayanagi, W.J. MacKnight, *Polymer*, **26**, 978-986, (1985).

1-2) "Szycher's Handbook of Polyurethanes", M. Szycher, CRC Press, Boca Raton, (2012).

1-3) "Polyurethane elastomers: from morphology to mechanical aspects", C. Prisacariu, Springer Science & Business Media, (2011).

1-4) "Polyurethanes in biomedical applications", N.M. Lamba, K.A. Woodhouse, S.L. Cooper, CRC press, (1997).

1-5) A. Takahara, J. Tashita, T. Kajiyama, M. Takayanagi, W.J. MacKnight, *Polymer*, **26**, 987-996, (1985).

1-6) Q. Li, H. Zhou, D.A. Wicks, C.E. Hoyle, D.H. Magers, H.R. McAlexander, *Macromolecules*, **42**, 1824-1833, (2009).

1-7) M. Tanaka, S. Kuma, M. Funaya, S. Kobayashi, *US 20050131203A1*, (2005).

1-8) M. Fedurco, M. Ribezzo, A. Delfino, *US 2016O122460A1*, (2016).

1-9) S. Hsu, H. Xiao, H. Szmant, K. Frisch, *J. Appl. Polym. Sci.*, **29**, 2467-2479, (1984).

1-10) B.K. Kim, Y.M. Lee, *J. Macromol. Sci., Pure Appl. Chem.*, **29**, 1207-1221, (1992).

1-11) R.B. Dickinson, J.A. Nagel, R.A. Proctor, S.L. Cooper, *J. Biomed. Mater. Res.*, **36**, 152-162, (1997).

1-12) P. Król, B. Król, L. Subocz, P. Andruszkiewicz, *Colloid. Polym. Sci.*, **285**, 177-183, (2006).

1-13) R. Bonart, *J. Macromol. Sci.,Phys.,* **2**, 115-138, (1968).

1-14) S.L. Cooper, A.V. Tobolsky, *J. Appl. Polym. Sci.*, **10**, 1837-1844, (1966).

1-15) F.S. Bates, *Science*, **251**, 898-905, (1991).

1-16) Z.S. Petrovic, J. Ferguson, *Prog. Polym. Sci.*, **16**, 695-836, (1991).

1-17) J.T. Koberstein, R.S. Stein, *J. Polym. Sci., Part B: Polym.*

Phys., **21**, 1439-1472, (1983).

1-18) R. Bonart, E.H. Müller, *J. Macromol. Sci., Phys.*, **10**, 345-357, (1974).

1-19) C.G. Vonk, *J. Appl. Crystallogr.* , **6**, 81-86, (1973).

1-20) "Principles of Polymer Chemistry", P.J. Flory, Corenell University Press, Ithaca, (1953).

1-21) K. Kojio, T. Fukumaru, M. Furukawa, *Macromolecules*, **37**, 3287-3291, (2004).

1-22) K. Kojio, S. Nakashima, M. Furukawa, *Polymer*, **48**, 997-1004, (2007).

1-23) Z.S. Petrović, J. Budinski-Simendić, *Rubber Chem. Technol.*, **58**, 685-700, (1985).

1-24) Z.S. Petrović, J. Budinski-Simendić, *Rubber Chem. Technol.*, **58**, 701-712, (1985).

1-25) M.V. Pandya, D.D. Deshpande, D.G. Hundiwale, *J. Appl. Polym. Sci.*, **32**, 4959-4969, (1986).

1-26) H.F. Hespe, A. Zembrod, F.J. Cama, C.W. Lantman, S.D. Seneker, *J. Appl. Polym. Sci.*, **44**, 2029-2035, (1992).

1-27) S. Nozaki, S. Masuda, K. Kamitani, K. Kojio, A. Takahara, G. Kuwamura, D. Hasegawa, K. Moorthi, K. Mita, S. Yamasaki, *Macromolecules*, **50**, 1008-1015, (2017).

1-28) L. Born, H. Hespe, J. Crone, K. Wolf, *Colloid. Polym. Sci.*, **260**, 819-828, (1982).

1-29) J. Shin, H. Matsushima, J.W. Chan, C.E. Hoyle, *Macromolecules*, **42**, 3294-3301, (2009).

1-30) J.W.C. Bogart, P.E. Gibson, S.L. Cooper, *J. Polym. Sci., Part B: Polym. Phys.,* **21**, 65-95, (1983).

1-31) R. Bonart, L. Morbitzer, G. Hentze, *J. Macromol. Sci., Phys.*, **3**, 337-356, (1969).

1-32) R.W. Seymour, A. Allegrezza Jr, S.L. Cooper, *Macromolecules*, **6**, 896-902, (1973).

1-33) G. Estes, R. Seymour, S.L. Cooper, *Macromolecules*, **4**, 452-457, (1971).

1-34) I. Kimura, H. Ishihara, H. Ono, N. Yoshihara, S. Nomura,

H. Kawai, *Macromolecules*, **7**, 355-363, (1974).
1-35) H.S. Lee, S.R. Yoo, S.W. Seo, *J. Polym. Sci., Part B: Polym. Phys.*, **37**, 3233-3245, (1999).
1-36) A. Eisenberg, *Macromolecules*, **3**, 147-154, (1970).
1-37) Y.S. Ding, R.A. Register, C.-z. Yang, S.L. Cooper, *Polymer*, **30**, 1221-1226, (1989).
1-38) Y.S. Ding, R.A. Register, C.-z. Yang, S.L. Cooper, *Polymer*, **30**, 1204-1212, (1989).
1-39) H.S. Xu, C.Z. Yang, *J. Polym. Sci., Part B: Polym. Phys.*, **33**, 745-751, (1995).
1-40) D.J. Yarusso, S.L. Cooper, *Macromolecules*, **16**, 1871-1880, (1983).
1-41) S.A. Visser, S.L. Cooper, *Macromolecules*, **24**, 2576-2503, (1991).
1-42) S.A. Visser, S.L. Cooper, *Polymer*, **33**, 920-929, (1992).
1-43) W.J. MacKnight, W.P. Taggart, R.S. Stein, *J. Polym. Sci., Polym. Symp.*, **45**, 113-128, (1974).
1-44) D.J. Kinning, E.L. Thomas, *Macromolecules*, **17**, 1712-1718, (1984).
1-45) Y.S. Ding, R.A. Register, C.-z. Yang, S.L. Cooper, *Polymer*, **30**, 1213-1220, (1989).
1-46) J.K. Percus, G.J. Yevick, *Phys. Rev.*, **110**, 1, (1958).
1-47) G. Fournet, *Acta Crystallogr.*, **4**, 293-301, (1951).
1-48) Q. Guo. Polymer morphology: principles, characterization, and processing. John Wiley & Sons, 2016.
1-49) A. Nagai, B. Ochiai, T. Endo, *Macromolecules*, **37**, 7538-7542, (2004).

Chapter 2

Microphase-separated Structure and Mechanical Properties of Cycloaliphatic Diisocyanate-based Thiourethane Elastomers

2.1 Introduction

Polyurethane (PU) has been fascinating for more than 60 years. Recently, different types of polyurethane, such as hydroxyl PU,[2-1~4] phenolic PU,[2-5] sulfur containing PU,[2-6,7] and inorganic filler – another polymer–containing PU,[2-8] have been synthesized to improve PU properties. Polythiourethanes (PTUs) are members of the PU family, which can be obtained by the reaction between isocyanate and dithiol – instead of diol – as the chain extender. When polymer materials include sulfur atoms, the refractive index will be generally increased, resulting in materials with potential for optical application. Another expected and attainable property of sulfur-including materials is an adhesive property. Sulfur atoms can form strong bonds with a metal surface and sometimes exhibit a good adhesive property. Therefore, there is an expectation that PTUs may possess some properties that PUs do not possess. Some researchers have reported on the physical properties of thiourethane.[2-9~14] Li et al. investigated a series of hard segment models for urethane, thiourethane, and dithiourethane compounds. They found that the hydrogen bond strength of urethane is somewhat similar to thiourethane, while dithiourethane shows a lower propensity for hydrogen bonding compared to the urethane and thiourethane. Their findings suggest that the hydrogen bond strength and

fraction, and the structure of diisocyanate makes a contribution to the physical and mechanical properties of polyurethane, polythiourethane, and polydithiourethane.[2-11] In addition, Shin et al. studied the impact of phase separation on the mechanical properties of PTUs in terms of the hard and soft segment molecular weight and ratio, and the hard segment chemical structure. They found that the aforementioned factors have a strong influence on Young's modulus and elongation at break and tensile strength.[2-12] However, there are no reports on the effect of the dithiol and diol chain extender on the microphase-separated structure and mechanical properties.

The purpose of this study is to investigate the effect of dithiol and diol, and the methylene length of the chain extender on the microphase-separated structure and mechanical properties of PTU and PU elastomers using differential scanning calorimetry (DSC), small-angle X-ray scattering (SAXS), wide-angle X-ray diffraction (WAXD), dynamic viscoelastic property measurement, and tensile testing. To evaluate the effect of dithiol and diol, and the methylene length of the chain extender on the microphase-separated structure, dithiol and diol with two types of methylene length for the chain extender were used, which polymerized with poly(oxytetramethylene) glycol (PTMG) and 1,4-bis(isocyanatomethyl)cyclohexane (1,4-H_6XDI). Since

the dithiol group has a different character compared to the diol group, there is the expectation that the elastomers obtained from this chain extender exhibit various properties that have not been obtained before.

2.2 Experimental

2.2.1 Materials

1,4-bis(isocyanatomethyl)cyclohexane (FORTIMO™ 1,4-H_6XDI, produced by Mitsui Chemicals Inc.) and Poly(oxytetramethylene) glycol (PTMG: M_n = 1800, Asahi Kasei Chemicals Co., Ltd., Japan) were employed as the diisocyanate and polyol, respectively. 1,4-butanedithiol (BDT), 1,5-pentanedithiol (PDT), 1,4-butanediol (BD), and 1,5-pentanediol (PD) (FUJIFILM Wako Pure Chemicals Co., Ltd., Japan) were used as chain extenders, with a hard segment weight fraction of approximately 16%. All chain extenders were purified by distillation, whereas 1,4-H_6XDI was used without further purification.

2.2.2 Synthesis of PTU Elastomers

The four segmented polythiourethane and polyurethane were prepared by a prepolymer method in bulk using PTMG, 1,4-H_6XDI and the chain extender. Figure 2.1 shows the synthetic

scheme for PTU and PU. The fractions of hard segment were ca. 16 wt%. PTMG was dried under reduced pressure with dry nitrogen. Prepolymers were synthesized from 1,4-H_6XDI and PTMG with the ratio of $K = [NCO]_{iso}/[OH]_{PTMG} = 1.40$, at 80 °C for 3 h under N_2 atmosphere. As a catalyst, dibutyltin dilaurate (DBTL, FUJIFILM Wako Pure Chemical Co., Ltd. Japan) was added. The extent of the prepolymer reaction was observed by

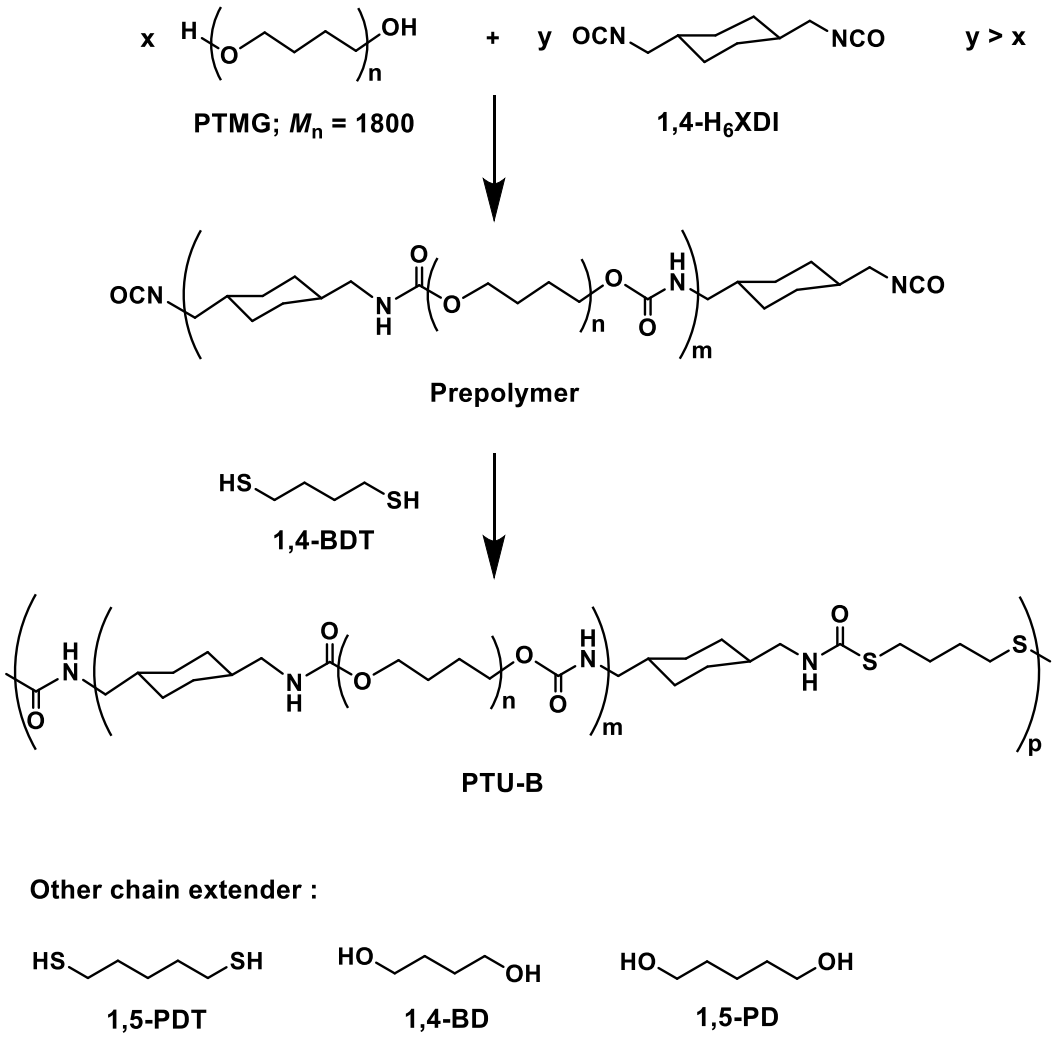

Figure 2.1 Reaction scheme for PTU-B using a prepolymer method.

using an amine equivalent method, and, then, stopped when the reaction ratio for the NCO groups reached over 90%. To remove the air inside, the obtained prepolymer was degassed in vacuum. The chain extender was added to the prepolymer with a ratio of $[NCO]_{pre}/[SH]$ and $[NCO]_{pre}/[OH]$ equal to 1.02, where $[NCO]_{pre}$ is the number of moles of NCO groups in the prepolymer, [SH] and [OH] are the number of moles of SH and OH groups, respectively. After agitating, the product was poured into a mold consisting of two aluminum plates with a 2-mm-thick spacer and heated at 110 °C for 24 h to perform polymerization.

2.2.3 Evaluation of Gel Fraction and Degree of Swelling

To investigate the network structure of PTU and PU, the gel fraction and the degree of swelling were evaluated. N,*N*-dimethylacetamide (DMAc) and toluene were used as a polar and nonpolar solvent, respectively. The gel fraction, G, was defined as $G = W_b/W$, where W is the initial weight, and W_b is the dried weight after swelling with a solvent. The degree of swelling, Q, was defined as $Q = 1 + [(W_a - W_b)/d_s/(W_b/d_p)]$, where W_a, d_s, and d_p is the weight of the samples swollen to an equilibrium state, density of the solvent and density of the elastomers, respectively.

2.2.4 Evaluation of Microphase-separated Structure

A Fourier transform infrared (FT-IR) spectroscopic measurement was conducted to evaluate the hydrogen bond state for the hard segment. A Spectrum One FT-IR spectrometer (PerkinElmer), Mercury cadmium telluride (MCT) detector, and attenuated total reflectance (ATR) accessory (Ge crystal, 45°) were employed for measurements. All FT-IR spectra were acquired at a resolution of 4 cm^{-1} with 32 scans.

Differential scanning calorimetric (DSC) thermograms were obtained using a DSC (DSC6220, SII EXSTAR 6000, Seiko Instruments) from -140 to 240 °C with a heating rate of 10 °C min^{-1} under a N_2 atmosphere.

The molecular aggregation structure was evaluated by synchrotron radiation X-ray analyses at the Frontier Softmaterial Beamline (FSBL, BL03XU) in the SPring-8 facility in Japan.[2-15,16)] Simultaneous wide-angle X-ray diffraction (WAXD) and small-angle X-ray scattering (SAXS) measurements can be conducted in this beamline. The wavelength and size of the X-ray beam was 0.1 nm and 150 μm x 150 μm. A PILATUS 1 M (DECTRIS, Ltd., pixel size of 172 μm) was used to obtain scattering in the small-angle region with a camera length of ca. 4 m. A flat panel detector was employed for WAXD measurements with a camera length of 74 mm. Scattering patterns were

measured with an exposure time of 200-500 ms. The data were processed using the FIT-2D (Ver. 12.077, Andy Hammersley/ ESRF, Grenoble, France).

2.2.5 Evaluation of Mechanical Properties

Temperature dependence of dynamic viscoelastic functions were obtained with a dynamic viscoelastometer (RHEOVIBRON DDV-01FP, ORIENTEC). Measurements were performed from -145 to 240 °C with a heating rate of 1 °C min^{-1} under N_2 atmosphere. The dimension of the specimens used was 30 mm x 5 mm x 0.3 mm. The applied frequency was 11 Hz.

Tensile testing was carried out with EZ-Graph (Shimadzu, Japan) at room temperature. The dimension of the samples was 100 mm x 5 mm x 2 mm. The initial length and elongation rate were 30 mm and 10 mm min^{-1}, respectively.

2.3 Results and Discussion

2.3.1 Gel Fraction and Degree of Swelling

Table 2.1 shows the basic properties including the degree of swelling, density, and gel fraction of the PTU and PU elastomers (abbreviation denotes the type of polymer and chain extender). All samples were soluble in dimethylacetamide (DMAc), indicating the existence of only physical crosslinks that

Table 2.1 Basic properties of the PTU and PU elastomers.

Sample	Density ($g\ cm^{-3}$)	Gel fraction, G (%)		Degree of swelling, Q	
		Toluene	DMAc	Toluene	DMAc
PTU-B	1.02	98.5±0.3	Soluble	2.23±0.05	Soluble
PTU-P	1.02	71.7±0.5	Soluble	2.82±0.04	Soluble
PU-B	1.02	99.3±0.4	Soluble	2.16±0.03	Soluble
PU-P	1.02	79.4±0.3	Soluble	2.81±0.04	Soluble

undergo dissociation in the polar solvent. The gel fraction of elastomers prepared using a BD-based chain extender swollen by toluene were approximately 99%, implying that the physical crosslinking network is well-developed. Moreover, the degree of swelling in toluene for elastomers with PD-based chain extenders is larger than that for BD-based chain extenders, suggesting less ordered hard segment chains. The influence of the methylene length of the chain extender on the degree of swelling for PU is stronger than that for PTU.

2.3.2 Hydrogen Bonding State of the Hard Segment Chain

The hydrogen bonding state for the PTU and PU elastomers was assessed by ATR-FTIR analysis (Figure 2.2). The stretching vibrations of the NH groups and carbonyl bands indicate the presence of thiourethane and urethane moieties. The NCO stretching band at 2260 cm^{-1} was not observed in all spectra,

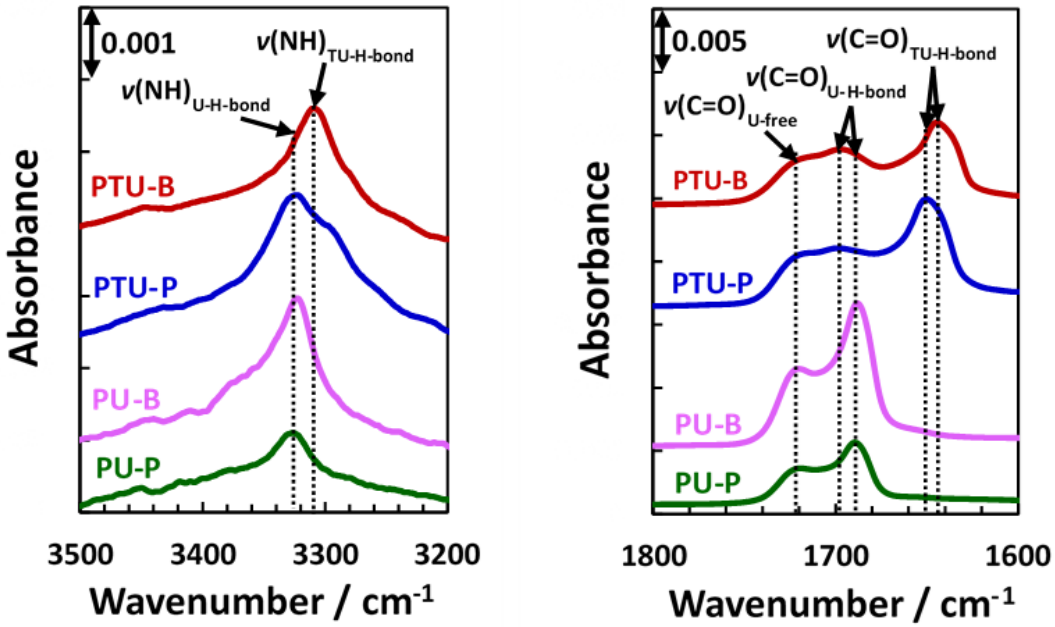

Figure 2.2 ATR-FT-IR spectra of PTU and PU elastomers. (a) NH stretching (ν(NH), (b) C=O stretching (ν(C=O) bands.

indicating that the reaction occurred properly. Absorption bands at approximately 1722, 1705 and 1688 cm^{-1} correspond to urethane carbonyl free ($\nu(C=O)_{U\text{-}free}$), disordered and ordered hydrogen bonded carbonyl groups of urethane ($\nu(C=O)_{U\text{-}H\text{-}bond}$) stretching vibrations, respectively.[2-17] Whereas, thiourethane carbonyl free ($\nu(C=O)_{TU\text{-}free}$) and hydrogen bonded carbonyl groups of thiourethane ($\nu(C=O)_{TU\text{-}H\text{-}bond}$) stretching vibrations appear at approximately 1670-1640 cm^{-1}.[2-18~20] The NH stretching region at approximately 3450, 3290-3310 and 3300-3350 cm^{-1} are assigned to urethanes NH free ($\nu(NH)_{free}$), hydrogen-bonded NH groups with ether oxygen ($\nu(NH)_{ether}$) of

PTMG and urethane carbonyl groups ($\nu(NH)_{U\text{-}carbonyl}$) stretching vibration, respectively.[2-21,22] In addition, the bands at approximately 3301-3332 cm^{-1} arise from the hydrogen-bonded NH moiety of the thiourethane group ($\nu(NH)_{TU\text{-}H\text{-}bond}$).[2-11,18]

2.3.3 Hard Segment Crystal Structure

WAXD measurements were conducted to examine the hard segment crystal structures of the PTUs and PUs. Figure 2.3 exhibits WAXD profiles for the PTUs, PUs together with the related hard-segment models for comparison. The PTU-B showed a weak peak and shoulders at q = 12.1, 13.7 and 16.1 nm^{-1}, which

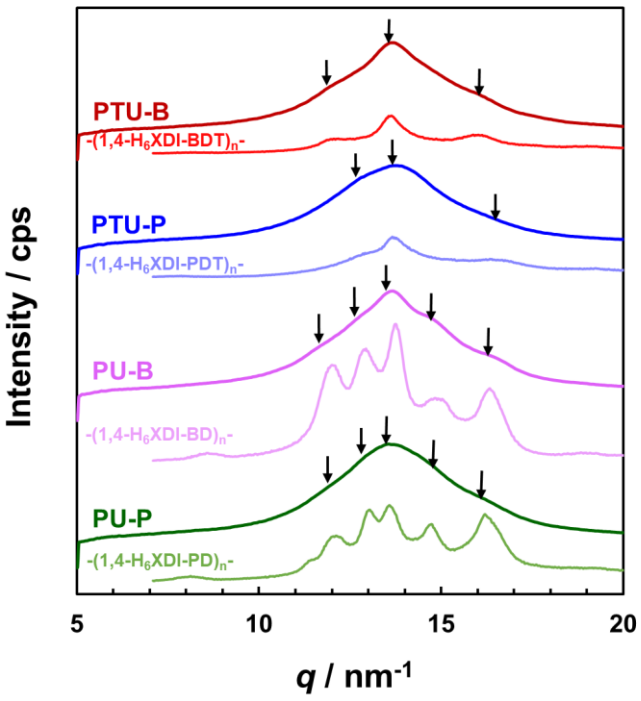

Figure 2.3 WAXD profiles for the PTUs, PUs and the related hard segment models.

correspond well to the –(1,4-H_6XDI-BDT)$_n$– model. A weak peak and shoulders were also observed for PU-B at q = 12.1, 13.0, 13.8, 15.0 and 16.4 nm^{-1}, which correspond well to peaks of the –(1,4-H_6XDI-BD)$_n$– model. These results suggest that there exist crystalline hard segment domains, consistent with the related hard segment model in PU-B. In contrast, the WAXD profile for PTU-P and PU-P only exhibited an amorphous halo at approximately 13.8 nm^{-1}. The crystalline peaks cannot be observed due to overlap with an amorphous halo of the soft segment.[2-23,24] This result implies that the elastomers with a PD-based chain extender possess less ordered crystalline hard segment chains.[2-25]

2.3.4 Microphase-separated Structure

Figure 2.4 shows DSC thermograms for the PTU and PU elastomers. For all samples, a baseline shift was observed at approximately -72 °C. This can be assigned to the glass transition temperatures of the soft segment chains ($T_{g,S}$) for the PTUs and PUs. The $T_{g,S}$ value for the PTUs is slightly lower than that for PUs, indicating that the PTUs possess a stronger degree of microphase separation. It is well-known that an increasing $T_{g,S}$ for PU elastomers is a consequence of increasing phase mixing. An exothermic peak corresponding to reorganized-

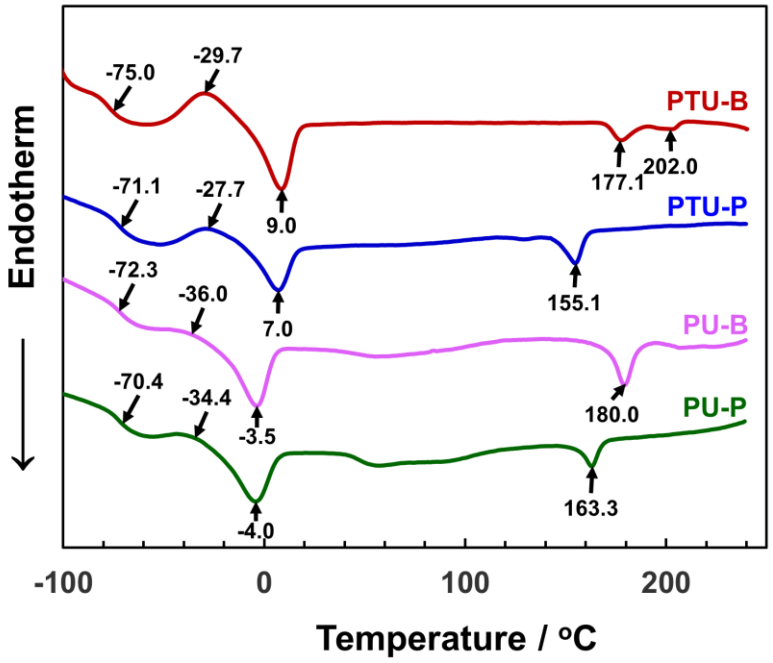

Figure 2.4 DSC thermograms for the PTU and PU elastomers.

crystallization of activated PTMG chains and an endothermic peak being assignable to the melting of crystallized PTMG chains ($T_{m,S}$) were measured at approximately -36 to -27 and -4 to 10 °C, respectively.

Exothermic peaks for the PTUs were larger than those for the PUs because of the difficulty of reorganized-crystallization of the soft segments during the heating process.[2-26~28] In contrast, the soft segment in the PUs can easily crystallize with the cooling process. Furthermore, PTUs showed a lower melting temperature ($T_{m,H}$) compared to the PUs, indicating that the ordering and lamella thickness of the hard segment of the PTUs are lower and smaller than for PUs, respectively. In addition,

elastomers with a PD-based chain extender show a lower $T_{m,H}$ in comparison with elastomers with the BD-based chain extender. This is due to the lack of molecular symmetry, curved molecules, and relatively large distances of the hydrogen bond in elastomers with a PD-based chain extender.[2-29)]

To obtain particular insight for the microphase-separated structure of PTU and PU elastomers, a SAXS measurement was conducted. Figure 2.5 shows the SAXS profiles and calculated three-dimensional correlation functions for the PTU and PU elastomers. Scattering peaks with a broad shape are observed in

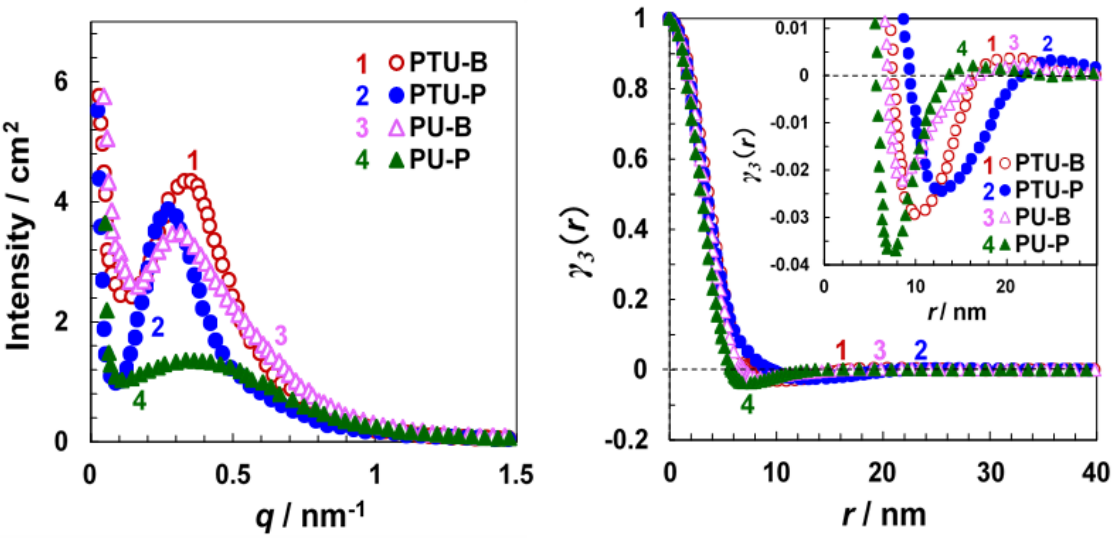

(a) (b)

Figure 2.5 (a) SAXS profiles and (b) calculated three-dimensional correlation functions for the PTU and PU elastomers.

the q range 0.1-1.0 nm^{-1}. The peak is assigned to the spacing between hard segment domains in the microphase-separated

system.

The spacing between hard segment domains was defined from analysis of three-dimensional correlations functions, $\gamma_3(r)$, from the following equation:

$$\gamma_3(r) = \frac{1}{Q}\int_0^\infty q^2 I(q)\frac{\sin(qr)}{qr}dq \qquad (2.1)$$

The diffuse boundary thickness was obtained from Porod's law, with the quantitative analysis for the microphase separation evaluation determined by the calculation method proposed by Vonk,[2-30] Bonart and Muller,[2-31] and Kobersteinand Stein [2-32]

The overall degree of phase separation for a complete phase separated two-phase system is defined as the ratio of the experimental electron density variance to the theoretical variance

$$\overline{\Delta\eta^{2\prime}}/\overline{\Delta\eta_c^2} \qquad (2.2)$$

with the theoretical electron density variance assuming complete phase separation is defined as

$$\overline{\Delta\eta_c^2} = \emptyset_{HS}\emptyset_{SS}(\eta_{HS} - \eta_{SS})^2 \qquad (2.3)$$

where $\emptyset_{HS}$ and η_{HS} are the volume fractions and electron densities of the hard segment, respectively.

The experimental electron density variance can be calculated from the background corrected intensities for one-dimensional scattering data using Porod's invariant Q

$$\overline{\Delta\eta^{2\prime}} = cQ = c\int_0^\infty [I(q) - I_b(q)]q^2 dq \quad (2.4)$$

with the effects of diffuse phase boundaries calculated from

$$\overline{\Delta\eta^{2\prime\prime}} = c\int_0^\infty \frac{[I(q) - I_b(q)]q^2}{H^2(q)} dq \quad (2.5)$$

where

$$c = \frac{1}{2\pi^2 i_e N_A^2} = 1.76 \times 10^{-24}\, mol^2/cm^2 \quad (2.6)$$

N_A is Avogadro's number, and i_e is Thompson's constant for the scattering from one electron. $H(q)$ is the function characterizing the shape and size of the interfacial boundary between two phases and $I_b(q)$ is the background intensity due to thermal density fluctuation. For a sigmoidal-shaped interface

$$H(q) = \exp\left(-\frac{\sigma^2 q^2}{2}\right) \quad (2.7)$$

and for a linear-gradient model

$$E \cong \sqrt{2\pi\sigma} \quad (2.8)$$

with $E = 0$ and $H(q) = 1$ for a sharp interface. σ is the width of the boundary layer whose value is obtained from the scattering intensity calculated using Porod's law

$$I(q) = \frac{K_p}{q^4}\exp(-\sigma^2 q^2) + I_b(q) \quad (2.9)$$

where K_p, σ, and I_b are estimated by fitting the scattering curves at large q values.

The obtained results can be seen in Table 2.2. PTUs exhibit a greater value of the overall degree of microphase

Table 2.2 The domain spacing, boundary thickness, and degree of microphase separation in the PTU and PU elastomers.

Sample	*d*-spacing / nm		Overall phase separation $(\overline{\Delta\eta^{2\prime}}/\overline{\Delta\eta_c^2})$	Diffuse boundary mixing $(\overline{\Delta\eta^{2\prime\prime}}/\overline{\Delta\eta^{2\prime}})-1$	Phase mixing within domains $(\overline{\Delta\eta_c^2}/\overline{\Delta\eta^{2\prime\prime}})-1$	Boundary thickness/nm	
	Bragg's law	3D-Correlation function				σ	E
PTU-B	18.6	20.2	0.35	0.02	1.76	0.19	0.46
PTU-P	23.5	25.2	0.26	0.03	2.67	0.21	0.52
PU-B	20.2	21.9	0.25	0.02	2.94	0.17	0.42
PU-P	15.1	15.7	0.17	0.03	4.85	0.17	0.43

The hard segment densities were obtained by modeling the crystal structure of hard segment models (Appendix Table 2A.1, Figure 2A.1, and 2A.2).

separation compared to PUs, which is influenced by both diffuse boundary mixing $(\overline{\Delta\eta^{2\prime\prime}}/\overline{\Delta\eta^{2\prime}})-1$ and phase mixing within domains $(\overline{\Delta\eta_c^2}/\overline{\Delta\eta^{2\prime\prime}})-1$. Although the diffuse boundary mixing is about the same, the contribution of phase mixing within domains leads to an obviously different value for the overall phase separation. In addition, PTUs possess a broader diffuse microphase boundary thickness compared to PUs. This can be due to the difference in the length distribution of the hard segment or soft segment and hard-soft segment compatibility.[2-23,32,33] Moreover, the phase mixing within domains for PTUs was smaller than for PUs, suggesting that a lower amount of hard segments (excess isocyanate blocks) are dissolved in the matrix or soft segments included in the hard segment domains.[2-31] Thus, we can state that the phase mixing within domains has a strong influence on the overall phase separation in PTU and PU elastomers.

2.3.5 Mechanical Properties

Figure 2.6 shows the temperature dispersion of dynamic viscoelastic functions (dynamic storage modulus (E'), dynamic loss modulus (E''), and loss tangent (tan δ)) of the PTUs and PUs. The E' and tan δ inflection point were detected at approximately -70 °C due to α_a-absorption arised from micro-Brownian segmental motion of amorphous PTMG associated with the glass

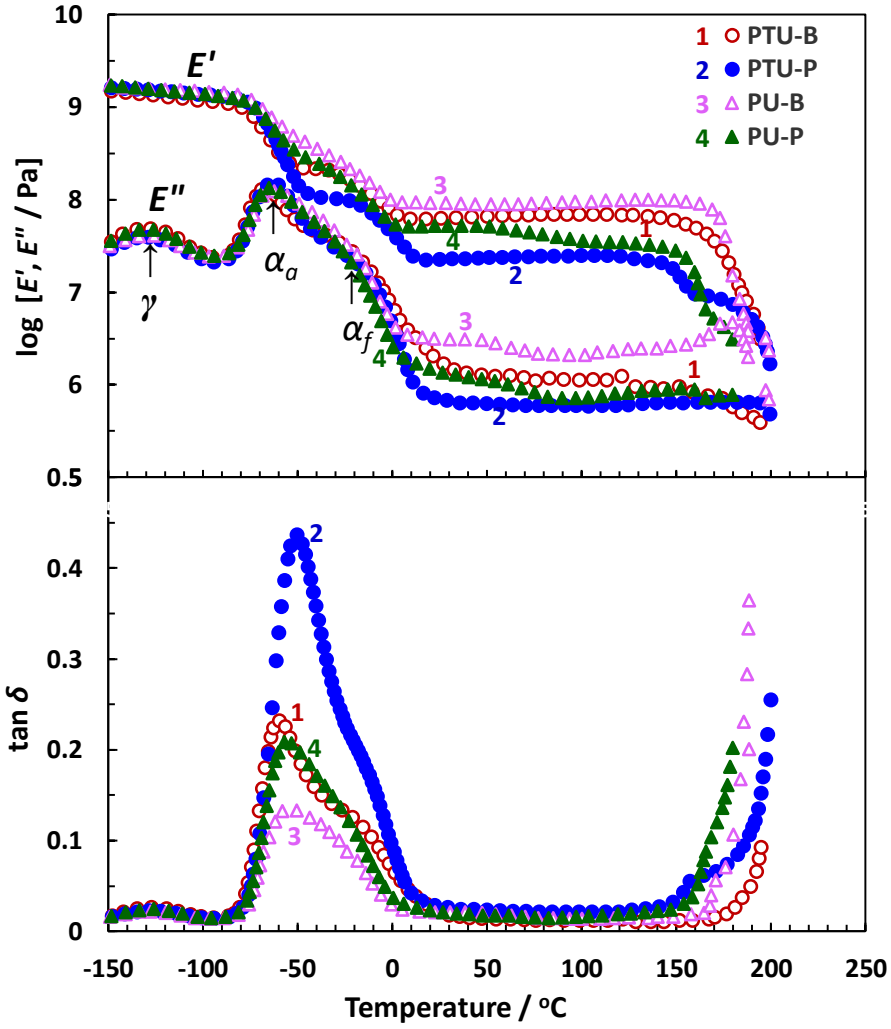

Figure 2.6 E', E'', and tan δ-temperature relationship for the PTUs and PUs measured at 11 Hz.

transition,[2-34~36] which for PTUs is slightly lower than for PUs, indicating a stronger degree of microphase separation. This result corresponds well with the value obtained by DSC measurement.

Figure 2.7 (a) shows master curves of the loss modulus for the α_a-relaxation process drawn by horizontal and vertical shifts of each frequency dependence loss modulus curves. The reference temperature, T_R, of 210 K was taken. The time-temperature superposition principle can be applied to the relaxation process of PTUs and PUs. Assuming that the relationship between shift factor, a_T, and measuring temperature

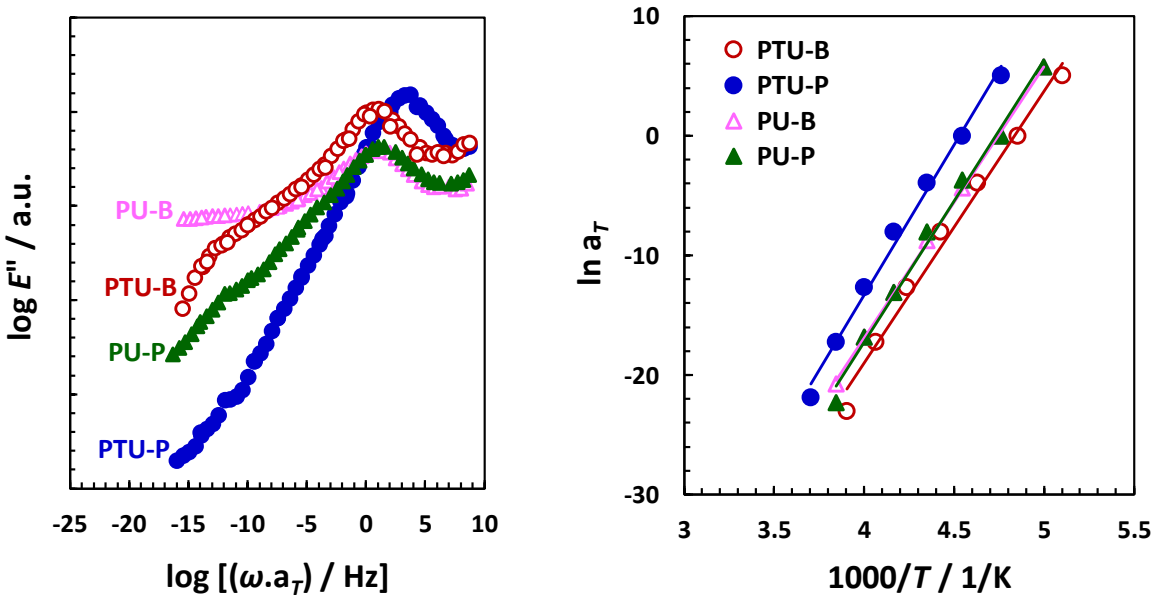

Figure 2.7 (a) Master curves of the loss modulus and (b) temperature dependence of the shift factor, a_T, for α_a-relaxation process for PTU and PU elastomers at reference temperature 210 K.

is Arrhenius type, the apparent activation energy for the α_a-relaxation process, ΔH_α^*, can be calculated from the slope of Arrhenius plot (Figure 2.7 (b)), according to equation

$$\ln a_T = \frac{\Delta H^*}{R}\left(\frac{1}{T} - \frac{1}{T_0}\right) \quad (2.10)$$

where R is the gas constant and T and T_0 are the measuring and the reference temperatures, respectively. The activation energy for the α_a-relaxation process for PTU-B and PTU-P are 200 and 208 kJ.mol^{-1}, respectively. Whereas, the activation energy for the α_a-relaxation process for PU-B and PU-P are 189 and 196 kJ.mol^{-1}, somewhat smaller than for PTUs. These values were in excellent accordance with ΔH_α^* of MDI-based PU.[2-37~39)]

The γ peak observed in PTUs and PUs is assigned to a local motion of the methylene sequences of PTMG. The α_f-absorption was observed as a shoulder on the higher temperature side of the α_a peak for PTUs and PUs, at approximately -20 °C. This peak is related to the melting process of the crystalline phase of PTMG.[2-37)] This shoulder was clearly observed for PTUs, which is consistent with a large exothermic peak in DSC. On the other hand, a shoulder that appears in PUs was smaller than in PTUs. As heating continues, a rubbery plateau was observed from 5 to 145 °C. The magnitude of E' at the rubbery plateau region for PTUs was slightly lower than for PUs. This is because the

ordering of the hard segment chains in PTUs is lower than in PUs. Therefore, the hard segment did not work well as physical crosslinking points in PTUs.

A decrease in the rubbery modulus at approximately 70 °C was observed for PU-P. This is because the increase in entropy with increasing temperature causing the decrease in the force due to the atoms being held together in bonds, as the bond length increases. On the other hand, PU-B showed a slight increase in the rubbery plateau region because of the softening of amorphous hard segment domains, remaining the semicrystalline hard segment domains with a more ordered structure.[2-37] Thus, it seems reasonable to conclude that the effect of the chain extender on the mechanical properties for PU is stronger than for PTUs. Moreover, the terminal temperature of PTUs is lower than that of PUs with the same type of chain extender, with an additional weak plateau observed for PTUs, indicating a thermally less stable hard segment because of the lower ordering of the hard segment chains. This is very consistent with the $T_{m,H}$ obtained by DSC.

The physical properties of PTU and PU elastomers were evaluated with tensile testing. Figure 2.8 represents the stress-strain curves for PTUs and PUs, and Table 2.3 summarizes their mechanical properties. The Young's modulus for PTUs was

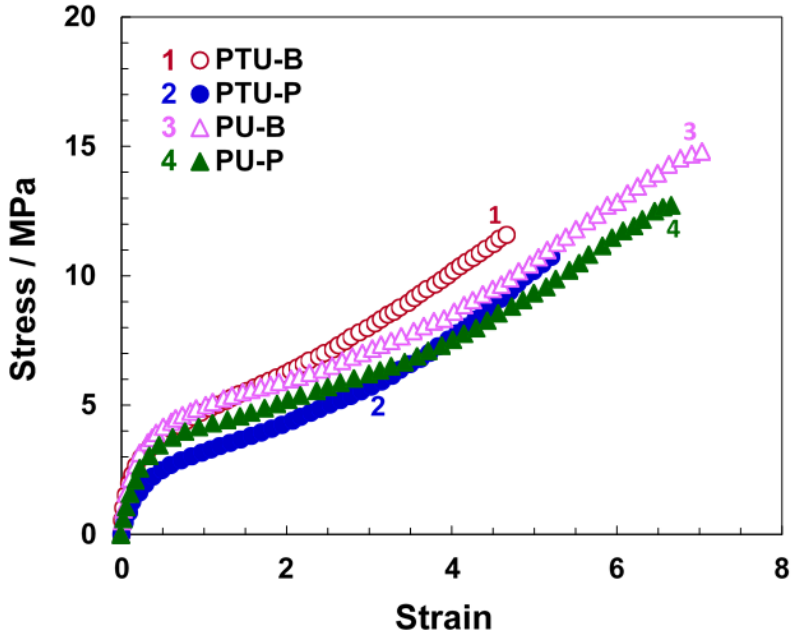

Figure 2.8 Stress-strain curves for the PTU and PU elastomers measured at 25°C.

slightly lower than for PUs. This trend corresponds well to the *E'* at the rubbery plateau region. This is because the hard segment chains ordering in PTUs is lower than in PUs, as was already mentioned above. The tensile strength difference for both PUs is greater than that for PTUs, indicating that the

Table 2.3 Mechanical properties for the PTU and PU elastomers obtained from the stress-strain relations shown in Figure 2.7.

Elastomers	Young's modulus / MPa	Tensile strength / MPa	Strain at break
PTU-B	54.8 ± 5.7	11.6 ± 0.3	4.7 ± 0.3
PTU-P	28.1 ± 3.0	10.7 ± 0.4	5.2 ± 0.2
PU-B	61.4 ± 6.9	14.8 ± 0.6	7.1 ± 0.4
PU-P	41.7 ± 3.8	12.7 ± 0.5	6.7 ± 0.3

influence of the chain extender on the mechanical properties for PU is stronger than that for PTU.

Figure 2.9 shows a schematic representation of the microdomain structure of PTU and PU elastomers. The PTUs possess a stronger degree of overall phase separation, less phase mixing within domains, and a wider boundary thickness in comparison with PUs. On the other hand, the ordering and lamella thickness of the hard segment of PTUs is lower and smaller than for PUs. In addition, the effect of the chain extender on the microdomain structure and mechanical properties in PU is stronger than in PTU.

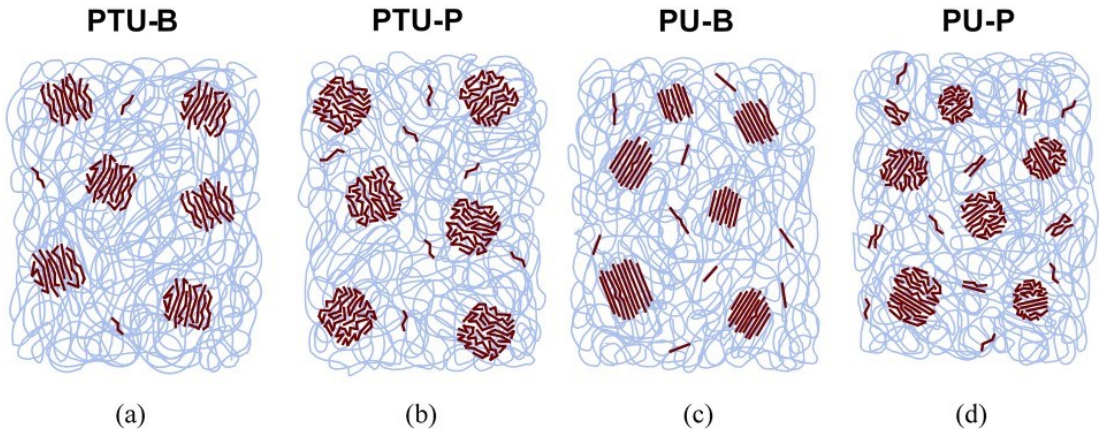

Figure 2.9 Schematic representation of the microphase-separated structure for (a) PTU-B, (b) PTU-P, (c) PU-B, and (d) PU-P elastomers.

2.4 Conclusions

The microphase-separated structure and mechanical

properties of 1,4-H_6XDI-based PTU elastomers were investigated. PTU and PU elastomers were prepared from PTMG, 1,4-H_6XDI and BDT, PDT, BD, and PD. By using the dithiol chain extender instead of the diol, elastomers with a stronger degree of microphase separation and less domain mixing were produced. As a result, the PTU showed a better low-temperature property, i.e., low T_g for the soft segment chain. However, since the ordering of the hard segment domains in the PTUs is lower than that for the PUs, they did not work well as physical crosslinking points, resulting in a mechanical property for PTUs that is comparable with PUs. Elastomers with a PD-based chain extender exhibited a lower degree of microphase-separated structure and mechanical property in comparison with elastomers with a BD-based chain extender. The influence of the methylene length of the chain extender on the microphase-separated structure and mechanical properties for PU is much stronger than that for PTU. PTU shows a weaker influence of the methylene length due to the stronger degree of microphase separation and lower domain mixing compared to PU. It is expected that the improvement of the mechanical properties of PTU can be achieved by fine-tuning the thermal history and hard segment content. The knowledge obtained in this study is useful for molecular structure design of PTUs for various applications.

References

2-1) N. Kihara, T. Endo, *J. Polym. Sci., Part A: Polym. Chem.*, **31**, 2765-2773, (1993).

2-2) H. Tomita, F. Sanda, T. Endo, *J. Polym. Sci., Part A: Polym. Chem.*, **39**, 3678-3685, (2001).

2-3) H. Tomita, F. Sanda, T. Endo, *J. Polym. Sci., Part A: Polym. Chem.*, **39**, 851-859, (2001).

2-4) E.K. Leitsch, G. Beniah, K. Liu, T. Lan, W.H. Heath, K.A. Scheidt, J.M. Torkelson, *ACS Macro Lett.*, **5**, 424-429, (2016).

2-5) S. Cao, S. Li, M. Li, L. Xu, H. Ding, J. Xia, M. Zhang, K. Huang, *Polym. J.*, **49**, 775, (2017).

2-6) J.Y. Jang, J.Y. Do, *Polym. J.*, **46**, 349, (2014).

2-7) A. Ohno, M. Hayashi, A. Takasu, *Polym. J.*, **50**, 959-966, (2018).

2-8) W. Li, X. Jiang, R. Wu, W. Wang, *Polym. J.*, **49**, 263-271, (2017).

2-9) C. Lü, Z. Cui, Z. Li, B. Yang, J. Shen, *J. Mater. Chem.*, **13**, 526-530, (2003).

2-10) M. Tanaka, S. Kuma, M. Funaya, S. Kobayashi, *US 20050131203A1*, (2005).

2-11) Q. Li, H. Zhou, D.A. Wicks, C.E. Hoyle, D.H. Magers, H.R. McAlexander, *Macromolecules*, **42**, 1824-1833, (2009).

2-12) J. Shin, H. Matsushima, J.W. Chan, C.E. Hoyle, *Macromolecules*, **42**, 3294-3301, (2009).

2-13) M. Rogulska, A. Kultys, E. Olszewska, *J. Therm. Anal. Calorim.*, **114**, 903-916, (2013).

2-14) M. Fedurco, M. Ribezzo, A. Delfino, *US 20160122460-A1*, (2016).

2-15) H. Masunaga, H. Ogawa, T. Takano, S. Sasaki, S. Goto, T. Tanaka, T. Seike, S. Takahashi, K. Takeshita, N. Nariyama, H. Ohashi, T. Ohata, Y. Furukawa, T. Matsushita, Y. Ishizawa, N. Yagi, M. Takata, H. Kitamura, K. Sakurai, K.

Tashiro, A. Takahara, Y. Amamiya, K. Horie, M. Takenaka, T. Kanaya, H. Jinnai, H. Okuda, I. Akiba, I. Takahashi, K. Yamamoto, M. Hikosaka, S. Sakurai, Y. Shinohara, A. Okada, Y. Sugihara, *Polym. J.*, **43**, 471-477, (2011).

2-16) K. Kojio, K. Matsuo, S. Motokucho, K. Yoshinaga, Y. Shimodaira, K. Kimura, *Polym. J.*, **43**, 692-699, (2011).

2-17) M.M. Coleman, K.H. Lee, D.J. Skrovanek, P.C. Painter, *Macromolecules*, **19**, 2149-2157, (1986).

2-18) A. Nagai, B. Ochiai, T. Endo, *J. Polym. Sci., Part A: Polym. Chem.*, **43**, 1554-1561, (2005).

2-19) N.G. Ireni, R. Narayan, P. Basak, K. Raju, *Polymer*, **97**, 370-379, (2016).

2-20) N.G. Ireni, M. Karuppaiah, R. Narayan, K. Raju, P. Basak, *Polymer*, **119**, 142-151, (2017).

2-21) H.S. Lee, Y.K. Wang, S.L. Hsu, *Macromolecules*, **20**, 2089-2095, (1987).

2-22) C. Brunette, S. Hsu, W. MacKnight, *Macromolecules*, **15**, 71-77, (1982).

2-23) S. Nozaki, S. Masuda, K. Kamitani, K. Kojio, A. Takahara, G. Kuwamura, D. Hasegawa, K. Moorthi, K. Mita, S. Yamasaki, *Macromolecules*, **50**, 1008-1015, (2017).

2-24) K. Kojio, S. Nakashima, M. Furukawa, *Polymer*, **48**, 997-1004, (2007).

2-25) J. Blackwell, M. Nagarajan, T. Hoitink, *Polymer*, **23**, 950-956, (1982).

2-26) K. Kojio, T. Fukumaru, M. Furukawa, *Macromolecules*, **37**, 3287-3291, (2004).

2-27) K. Kojio, M. Furukawa, Y. Nonaka, S. Nakamura, *Materials*, **3**, 5097-5110, (2010).

2-28) M. Furukawa, Y. Mitsui, T. Fukumaru, K. Kojio, *Polymer*, **46**, 10817-10822, (2005).

2-29) L. Born, H. Hespe, J. Crone, K. Wolf, *Colloid. Polym. Sci.*, **260**, 819-828, (1982).

2-30) C. Vonk, *J. Appl. Crystallogr.*, **6**, 81-86, (1973).

2-31) R. Bonart, E.H. Müller, *J. Macromol. Sci., Phys.*, **10**, 345-357, (1974).
2-32) J.T. Koberstein, R.S. Stein, *J. Polym. Sci., Part B: Polym. Phys.*, **21**, 1439-1472, (1983).
2-33) Z. Ophir, G.L. Wilkes, *J. Polym. Sci., Part B: Polym. Phys.*, **18**, 1469-1480, (1980).
2-34) K. Kojio, S. Nakamura, M. Furukawa, *J. Polym. Sci., Part B: Polym. Phys.*, **46**, 2054-2063, (2008).
2-35) A. Takahara, J. Tashita, T. Kajiyama, M. Takayanagi, *J. Biomed. Mater. Res.*, **19**, 13-34, (1985).
2-36) K. Kojio, M. Furukawa, S. Motokucho, M. Shimada, M. Sakai, *Macromolecules*, **42**, 8322-8327, (2009).
2-37) D.S. Huh, S.L. Cooper, *Polym. Eng. Sci.*, **11**, 369-376, (1971).
2-38) K. Tanaka, A. Takahara, T. Kajiyama, *Macromolecules*, **33**, 7588-7593, (2000).
2-39) T. Kajiyama, K. Tanaka, N. Satomi, A. Takahara, *Macromolecules*, **31**, 5150-5151, (1998).

Appendix

In order to achieve a better comprehension of hard segment crystal structure, the crystal structure solutions were determined from powder WAXD pattern of hard segment models. Crystal data and structure refinement details are summarized in Table 2A.1. Powder WAXD pattern indexing was carried out using McMaille indexing program[2A-1)] available in EXPO2014.[2A-2)] The figures of merit Mc20 for all samples are larger than 20, which means the indexing results are reliable. The best-estimated space group for all hard segments was triclinic $P\bar{1}$, with 2 molecules per unit cell. Furthermore, the starting molecular model which were optimized using universal force field is used for crystal structure solution using a simulated annealing approach. Finally, Rietveld refinement was performed for non-structural parameters using the Le Bail

Table 2A.1 Crystal data and structure refinement of the hard-segment models.

	1,4-H_6XDI-BDT	1,4-H_6XDI-PDT	1,4-H_6XDI-BD	1,4-H_6XDI-PD
Space group	$P\bar{1}$	$P\bar{1}$	$P\bar{1}$	$P\bar{1}$
a	0.505	0.513	0.518	0.500
b	0.949	0.957	0.929	0.957
c	2.099	2.166	1.746	1.841
α	107.7	108.2	107.2	105.9
β	113.7	114.2	99.1	100.2
γ	98.7	96.8	112.1	108.3
Z	2	2	2	2
Density	1.26	1.24	1.31	1.29
R_p	1.506	1.320	1.587	2.105
R_{wp}	2.022	1.773	1.981	3.080

method and peak shape function using Pearson VII.

The crystal packing results are presented in Figure 2A.1. All hard segment model represent planar zigzag conformation with hydrogen bonding between neighboring chain.[2A-3~5)] For 1,4-H_6XDI-BDT, 1,4-H_6XDI-BD, and 1,4-H_6XDI-PD, hydrogen bonds are performed between NH and carbonyl adjacent chains, with the bond length approximately 0.27 nm. Whereas, for 1,4-H_6XDI-PDT, hydrogen bonds are performed not only between NH and carbonyl, but also between NH and thioether sulfur. For 1,4-H_6XDI-BDT and 1,4-H_6XDI-BD, carbonyl groups of adjacent chains are nearly antiparallel to form hydrogen bonds, while for 1,4-H_6XDI-PDT and 1,4-H_6XDI-PD, carbonyl groups of adjacent chains are in a parallel position. The interchain distance perpendicular to the hydrogen bonds is 0.427 and 0.404 nm for PTUs and PUs, respectively, which is appropriate with van der Waals distance between methylene groups.

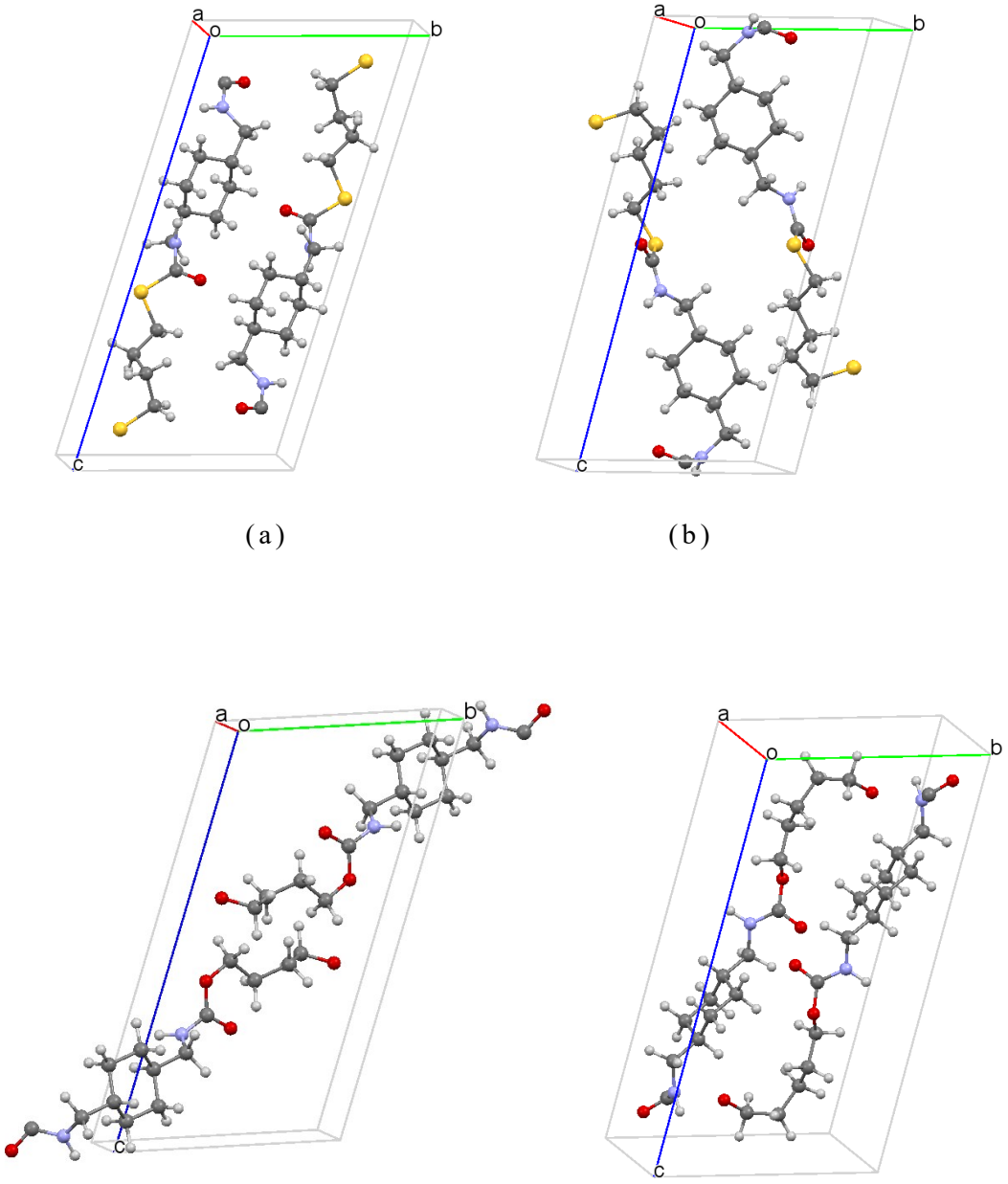

Figure 2A.1 The hard-segment models, (a) 1,4-H_6XDI-BDT, (b) 1,4-H_6XDI-PDT, (c) 1,4-H_6XDI-BD, and (d) 1,4-H_6XDI-PD.

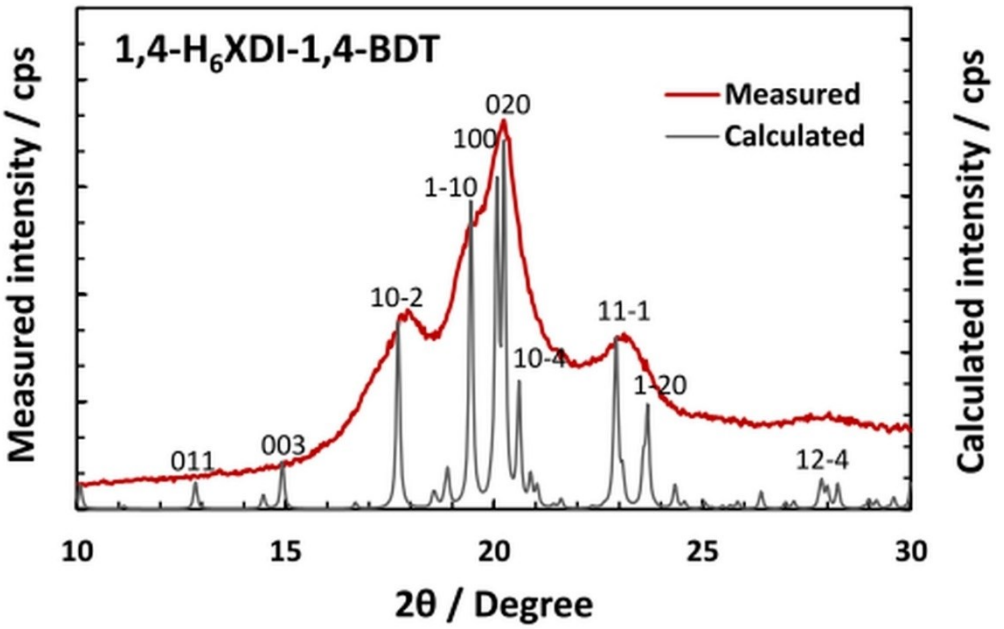

(a) 1,4-H_6XDI-BDT

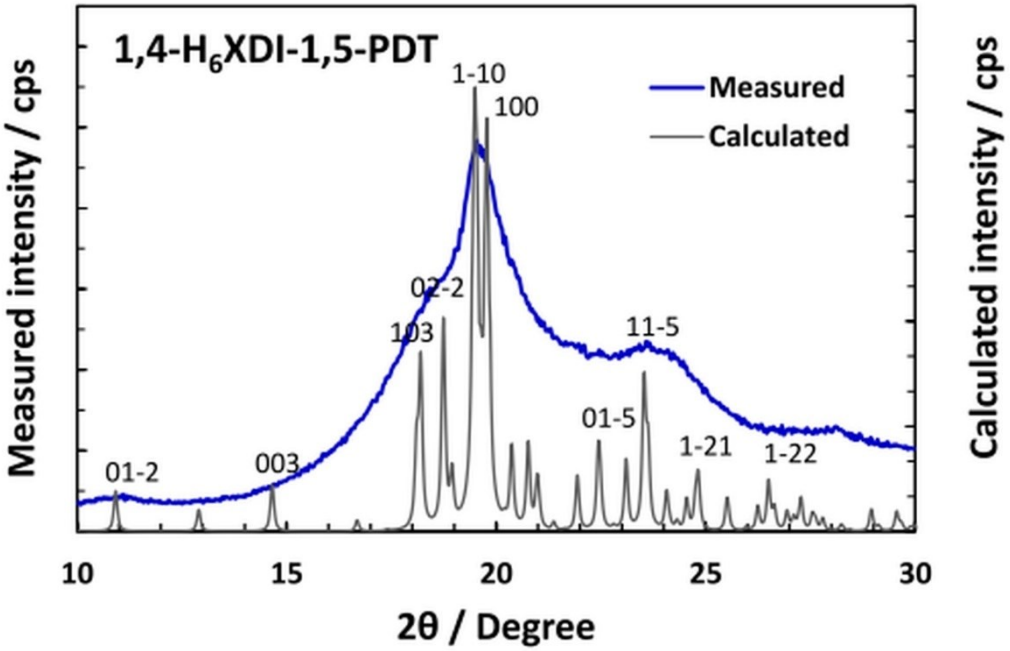

(b) 1,4-H_6XDI-PDT

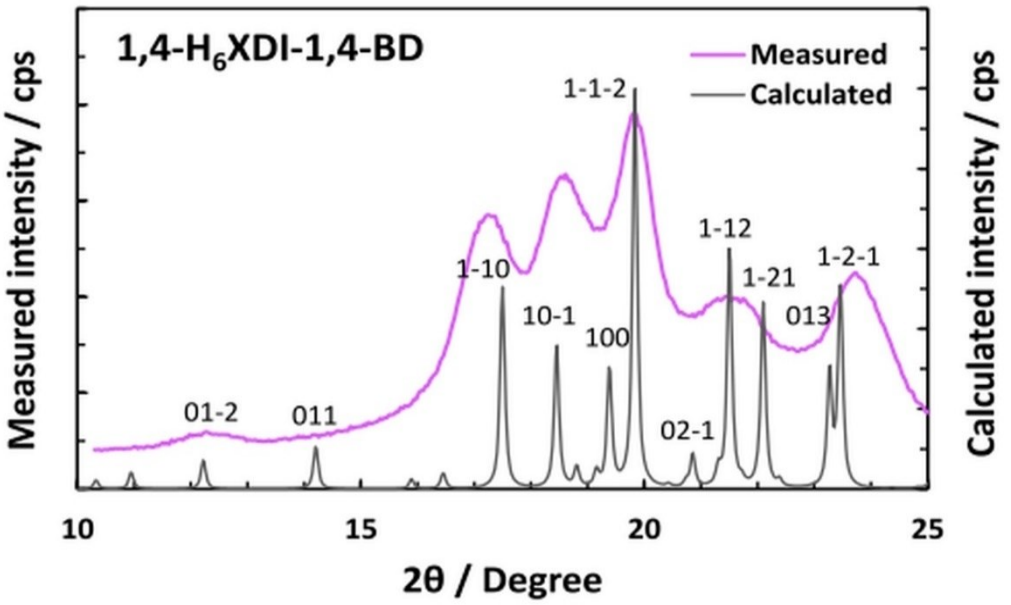

(c) 1,4-H_6XDI-BD

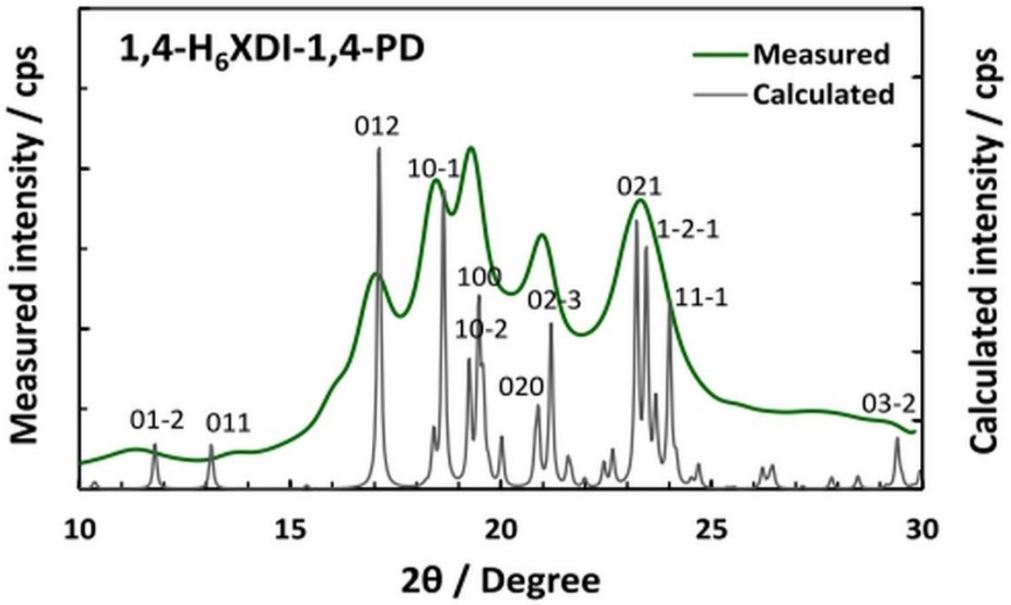

(d) 1,4-H_6XDI-PD

Figure 2A.2 Powder XRD of the hard-segment models, (a) 1,4-H_6XDI-BDT, (b) 1,4-H_6XDI-PDT, (c) 1,4-H_6XDI-BD, and (d) 1,4-H_6XDI-PD.

References

2A-1) A. Le Bail, *Powder Diffr.*, **19**, 249-254, (2004).

2A-2) A. Altomare, F. Ciriaco, C. Cuocci, A. Falcicchio, F. Fanelli, *Powder Diffr.*, **32**, S123-S128, (2017).

2A-3) C.E. Fernández, M. Bermúdez, S. Muñoz-Guerra, S. León, R.M. Versteegen, E.W. Meijer, *Macromolecules*, **43**, 4161-4171, (2010).

2A-4) Y. Saito, S. Nansai, S. Kinoshita, *Polym. J.*, **3**, 113-121, (1972).

2A-5) S. Nozaki, S. Masuda, K. Kamitani, K. Kojio, A. Takahara, G. Kuwamura, D. Hasegawa, K. Moorthi, K. Mita, S. Yamasaki, *Macromolecules*, **50**, 1008-1015, (2017).

Chapter 3

Investigation of Deformation Behavior of Thiourethane Elastomers using X-ray Scattering, Diffraction and Absorption Methods

3.1 Introduction

Polyurethane (PU) is one of the most well-known polymers which has been extensively explored and used in a wide range of applications, including, among others, household appliances, electronic devices, medical implants, and automotive parts. The vast majority of the existing literature on PUs has mainly focused on studying the structure-property relationship in order to obtain more superior materials.[3-1~10] Such studies involve a comprehensive analysis of structural change of hard and soft segment of PU during deformation by relying on small-angle X-ray scattering (SAXS), wide-angle X-ray diffraction (WAXD), and infrared dichroism method. For instance, Bonart et al.[3-1,2] investigated the deformation behavior in PUs with polyether and polyester-based soft segment using SAXS and WAXD. They found that the deformation behavior of the hard segment domains in PUs is highly influenced by the nature of the hard segment, exhibiting orientation of hard segments along the elongation direction, which is likely due to the local torque force from the oriented soft segment. Furthermore, Cooper and co-workers[3-11,12] studied the orientation of hard and soft segments in the polyether and polyester urethane under uniaxial deformation using infrared dichroism. They found that the orientation of hard segments is affected mainly by the hard

segment length, while soft segment orientation is less affected by polymer composition. Moreover, the hard segment orientation is also influenced by the type of ordering inside the hard segment domains. In addition, the hard segment domains have a tendency to retain a partially oriented conformation after the stress is removed, whereas the soft segments return to an unoriented state. Furthermore, Lee et al.[3-13] reported the uniaxial deformation of PU elastomers using Fourier transform infrared (FTIR) and synchrotron SAXS methods and found that the deformation behavior of PU elastomers depends on the orientation of the hard segment domains in the initial state. The hard segment domains with a parallel orientation to elongation direction underwent increasing spacing of hard segment domains at low strain, whereas the ones with perpendicular orientation showed decreasing propensity.

The abovementioned literature on deformation behavior of PUs which relies mainly on SAXS, WAXD and FTIR focuses on identifying the changes in the orientation and spacing of hard segment domains, strain-induced crystallization of soft segment, and orientation of functional groups. However, such studies provide no structural information of the short-range order in the vicinity of the absorbing atom. Therefore, the extended X-ray absorption fine structure (EXAFS) method, which enables us to

obtain a set of structural parameters in the range below 0.5 nm, is required as a complement for SAXS, WAXD, and FTIR analysis. EXAFS is a method which has been extensively utilized to investigate the molecular structure of the material, such as determining the vicinity of the cation in ionomers[3-14~16] and molecular structure behavior under uniaxial deformation.[3-17] The ability of EXAFS spectra to observe the changes in the short-range order, make it suitable for investigating the degree of order at this level, which is essential for studying the deformation behavior of polymers. Despite its potential contribution, only a few studies have been utilized EXAFS for deformation behavior analysis. For instance, Grady et al.[3-17] investigated the uniaxial deformation in sulfonated polystyrene by using EXAFS and found different patterns of bond vectors alignment and degree of order during uniaxial deformation. However, for the case of PUs, although it has not been used for studying the deformation behavior, EXAFS method has been used for studying the changes in the degree of order due to variations in degree of neutralization in polyurethane ionomers.[3-18]

Polythiourethanes (PTUs) are sulfur analogs of PUs, which are produced from the reaction between polyol, diisocyanate, and dithiol chain extender. As well as PUs, PTUs are comprised of the soft and hard segments, where the hard

segments act as physical crosslinks between the soft segments. Due to their thermodynamic incompatibility, the hard and soft segments tend to form a microphase-separated structure in the nanometer scale which strongly affects the mechanical properties of PTUs.[3-19~22] Despite their potential elastomeric properties, the deformation induced structural changes in the PTUs has not been comprehensively investigated. This paper aims to investigate the deformation behavior of PTUs related to the microphase-separated structure. The microphase-separated structure of PTU elastomers during uniaxial elongation will be studied using in situ SAXS, WAXD measurements, whereas the degree of order will be investigated using the sulfur K-edge EXAFS. In addition, the effect of the methylene length of chain extender on the deformation behavior of PTUs will be evaluated.

3.2 Experimental

3.2.1 Materials

The chemical structures of PTU elastomers are shown in Figure 3.1. The polymer glycol and diisocyanate used in this study were poly(oxytetramethylene) glycol (PTMG: M_n = 1800, Asahi Kasei Chemicals Co., Ltd., Japan) and 1,4-bis(isocyanatomethyl) cyclohexane (FORTIMO^{TM} 1,4-H_6XDI, Mitsui Chemicals Inc.), respectively. Whereas, the chain

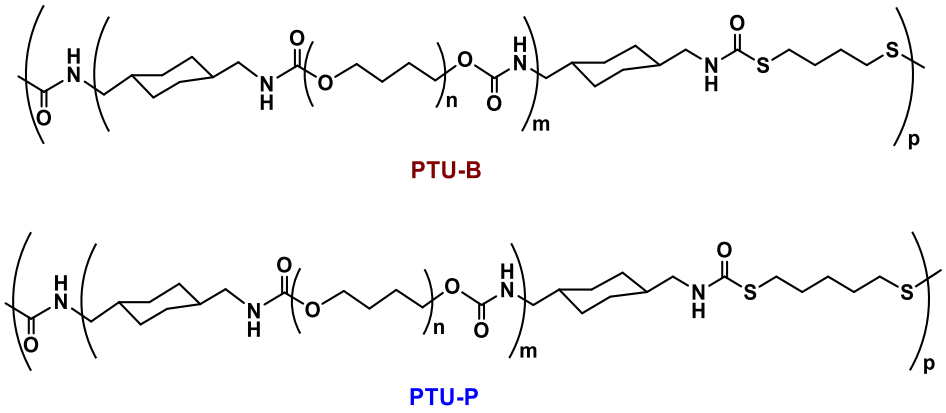

Figure 3.1 Chemical structures of PTU-B and PTU-P.

extenders used were 1,4-butanedithiol (BDT) and 1,5-pentanedithiol (PDT) (FUJIFILM Wako Pure Chemicals Co., Ltd., Japan), with a weight ratio of hard segment approximately 16%. The diisocyanate was used as received, while chain extenders were purified by distillation. The number average molecular weights (M_n), weight average molecular weight (M_w), and polydispersity index (M_w/M_n) for PTU-B are 53,000 g mol^{-1}, 171,000 g mol^{-1}, and 3.2, respectively, whereas, for PTU-P, M_n , M_w and M_w/M_n are 56,000 g mol^{-1}, 210,000 g mol^{-1}, and 3.8, respectively. The GPC curves for both PTUs are provided in Figure 3A.1.

3.2.2 Sample Preparation

The segmented PTUs were prepared by a two-step method in bulk, as described in the previous work.[3-22)] PTMG was dried under reduced pressure with dry nitrogen in the four-neck flask

and then 1,4-H_6XDI was added to the flask with the ratio of K = $[NCO]_{iso}/[OH]_{PTMG}$ = 1.40 and reacted under N_2 atmosphere for 3 h at 80 ℃. Dibutyltin dilaurate (DBTL, FUJIFILM Wako Pure Chemical Co., Ltd. Japan) was used as a catalyst. The prepolymer reaction was monitored by using an amine equivalent method and stopped when the NCO group reaction ratio exceeds 90%. Moreover, the prepolymer was degassed in a vacuum, followed by the addition of the chain extender. The relative amount of the chain extender to NCO groups in the prepolymer was $[NCO]_{pre}/[SH]$ = 1.02. After agitating, the product was molded and heated at 110 ℃ for 24 h to perform polymerization.

3.2.3 In-situ SAXS-WAXD measurements

In-situ SAXS-WAXD measurements were carried out at the SPring-8 facility, Frontier Softmaterial Beamline (FSBL, BL03XU), Japan.[3-23,24)] The size and wavelength of the X-ray beam were 150 μm x 150 μm and 0.1 nm, respectively. The samples were elongated at a certain rate and scattering patterns were measured with an exposure time of 200-500 ms. The scattering in the small-angle region was obtained using A PILATUS 1 M detector (DECTRIS, Ltd., the pixel size of 172 μm x 172 μm) with approximately 4 m camera length. Whereas, a flat panel detector was operated for the wide-angle region, at 74 mm

camera length. Data processing were performed using the FIT-2D (Andy Hammersley/ ESRF, France).

The stress-strain curves for PTUs were obtained by a tensile testing machine at room temperature. The dimension of the samples was 100 mm x 5 mm x 2 mm. The initial length and elongation rate were 25 mm and 0.82 mm s^{-1}, respectively. Engineering strain and stress were used in this study. Engineering strain and stress were calculated by elongation divided by initial length and force divided by initial cross-section. True strain and stress were also plotted in Figure 3A.2. True strain and stress were calculated from force divided by cross-sectional area at a certain time by elongation divided by length at a certain time.

3.2.4 XAFS measurements

Figure 3.2 shows the schematic setup for XAFS measurements during the elongation process of PTU. XAFS measurements were carried out at Saga Synchrotron Light Research Center, Kyushu University Beamline (BL06), Japan with the storage ring operating at energy of 1.4 GeV. The energy range of this light source (bending magnet) is 2.1-23 keV. A silicon (111) double-crystal monochromator was used to obtain the incident X-ray beam. The typical photon flux is 10^{10} photons/s. The

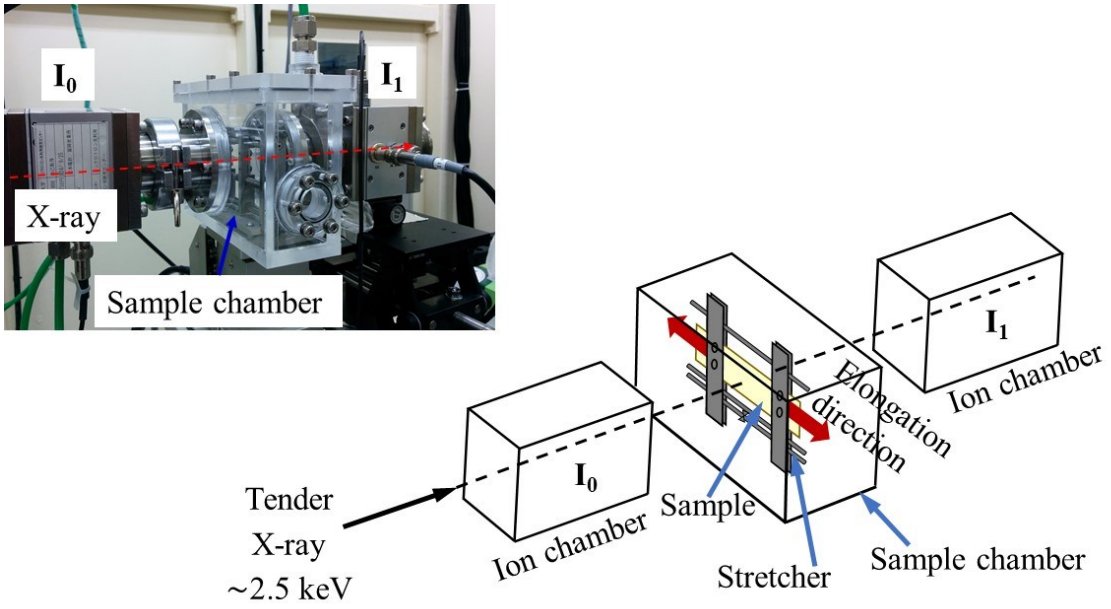

Figure 3.2 Schematic setup for XAFS measurements during the elongation process of PTU.

intensities of the incident beam and the transmitted beam were monitored using ionization chambers detector filled with He gas. The XAFS spectra of the PTUs was measured with a transmission mode at room temperature using sulfur K-edge and the absorption peak was calibrated using sodium thiosulfate standard, with the lowest energy of 2469 eV and the maximum of the first pre-edge is 2472 eV. It took ca. 5 minutes to sweep energy and measurements were conducted at a certain strain. The dimension of the sample was 30 mm x 5 mm x 0.1 mm.

3.2.5 EXAFS data analysis

In this study, the EXAFS $\chi(k)$ spectrum is the

superposition of sinusoidal wave functions (equation (1)) of the sulfur neighboring atoms in the PTU hard segments. This spectrum is Fourier transformed from wavenumber (nm^{-1}) to radial distance (nm) in order to filter the frequency.[3-25,26] The FT magnitude, $|\chi(R)|$, is the most common way to present the data, hiding the oscillation in the complex $\chi(R)$, since the FT makes $\chi(R)$ a complex function, with real and imaginary part. The FT magnitude is related to radial distribution function, which account the contribution of multiple-scattering paths, k-weighting, disorder, dependence of scattering amplitude on k, an infinite mean free path and so on. The positions of the peaks are related to the distance between the absorber and the neighboring atoms, whereas the magnitude or size of the peaks is related to the numbers and types of the neighboring atoms.

$$\chi(k) = \frac{\mu(E) - \mu_0(E)}{\mu_0(E)}$$

$$= \sum_j S_0^2(k)\, N_j \frac{F_j(k)}{kr_j^2}\, e^{-2\sigma_j^2 k^2}\, e^{-2r_j/\lambda_j} \sin[2k\, r_j + \phi_{ij}(k)] \quad (3.1)$$

The $\mu(E)$ is the measured absorption coefficient and $\mu_0(E)$ is a background correspond to absorption of an isolated atom. k is the wave vector, which obtained from:

$$k = \sqrt{\frac{2m}{\hbar^2}(E - E_0)} \quad (3.2)$$

where E_0 is the edge energy, m is an electron mass, and $\hbar$ is the

Planck's constant divided by 2π. N_j is the number of neighboring atoms of type j in the j^{th} shell, $S_0^2(k)$ is the amplitude reduction factor due to excitations of electrons other than 1-s, $F_j(k)$ is the backscattering amplitude, and $\delta_j(k)$ is the phase shift of the photoelectron from the N_j atom. r_j is the root mean square distance between absorbing atom (sulfur) and neighboring atom, λ_j is the mean free path of photoelectron. σ_j^2 correspond to the mean-square relative displacement, which also known as the EXAFS Debye-Waller factor, is the variation in the distance of atoms from absorbing atom:

$$\sigma^2 = \langle (r - \bar{r})^2 \rangle \qquad (3.3)$$

An individual path will have contributions from scattering pairs that are closer or farther than the average due to the static and or thermal disorder. The EXAFS Debye-Waller factor is, therefore, a measure of both kinds of disorder.[3-26~28)]

EXAFS curves were analyzed to obtain the structural parameters, i.e. the distance to neighboring atom, the number of neighboring atoms, EXAFS Debye-Waller factor, edge energy, and amplitude reduction factor. All parameters left free for the initial state, with the coordination number followed the crystal structure which is obtained from powder WAXD. Data processing, including background removal, edge calibration, data

normalization, Fourier-transforms, and statistical analysis was performed by using ATHENA and ARTEMIS.[3-29] The model structures used in the calculations were obtained from the crystal structure solutions of powder WAXD pattern of the hard segment models.[3-22]

The R-factor, defined as

$$R = \frac{\sum_i^{N data}\left[y_i^{data} - y_i^{model}(x)\right]^2}{\sum_i^{N data}\left[y_i^{data}\right]^2} \quad (3.4)$$

is used to determine the misfit relative of the model and data. This value is typically found to below 0.05 or so for good fits, and often found to be much better than that.[3-26]

3.3 Results and Discussion

The stress-strain curves for PTU elastomers during uniaxial elongation is provided in Figure 3.3 and the true stress-true strain curves for PTUs during uniaxial elongation is provided in Figure 3A.2. The Young's modulus and tensile strength for PTU chain extended with butanedithiol (PTU-B) were greater than for PTU chain extended with pentanedithiol (PTU-P) due to the stronger degree of phase separation and higher hard segment chains ordering. Whereas, the elongation at break for PTU-P was larger than for PTU-B, indicating that the packing of the soft segment chains in PTU-P was more difficult.[3-

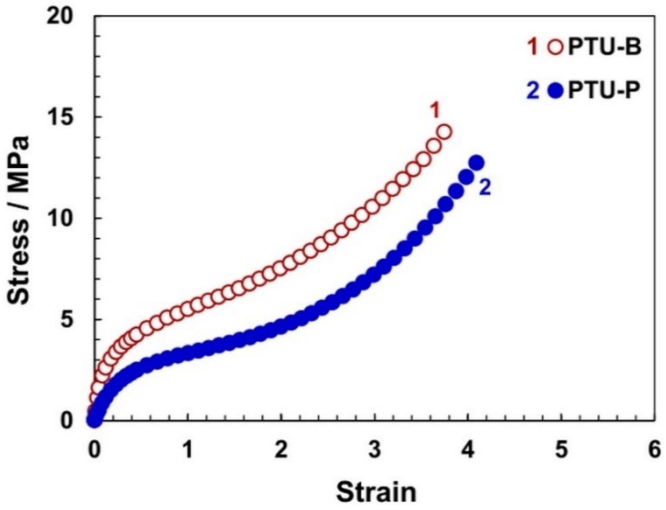

Figure 3.3 Stress-strain curves for PTU elastomers during uniaxial elongation measured at 25°C.

[22] The hard segment domains of PTU-B are spherical in shape with the spacing between hard segment domains and the degree of phase separation is 19.1 nm and 0.35, respectively. The degree of phase separation for PTU-B is higher than that for PTU-P, which possesses overall degree of phase separation 0.26. In addition, the spacing between hard segment domains for PTU-P is 24.5 nm. This spacing between hard segment domains was determined from three-dimensional correlation function (γ_3 (r)) analysis.[3-30]

3.3.1 In-situ SAXS-WAXD

Figure 3.4a shows the 2D-SAXS patterns for PTU-B during uniaxial elongation. Figure 3.4b exhibits the 1D meridional and equatorial SAXS profiles, and Figure 3.4c depicts

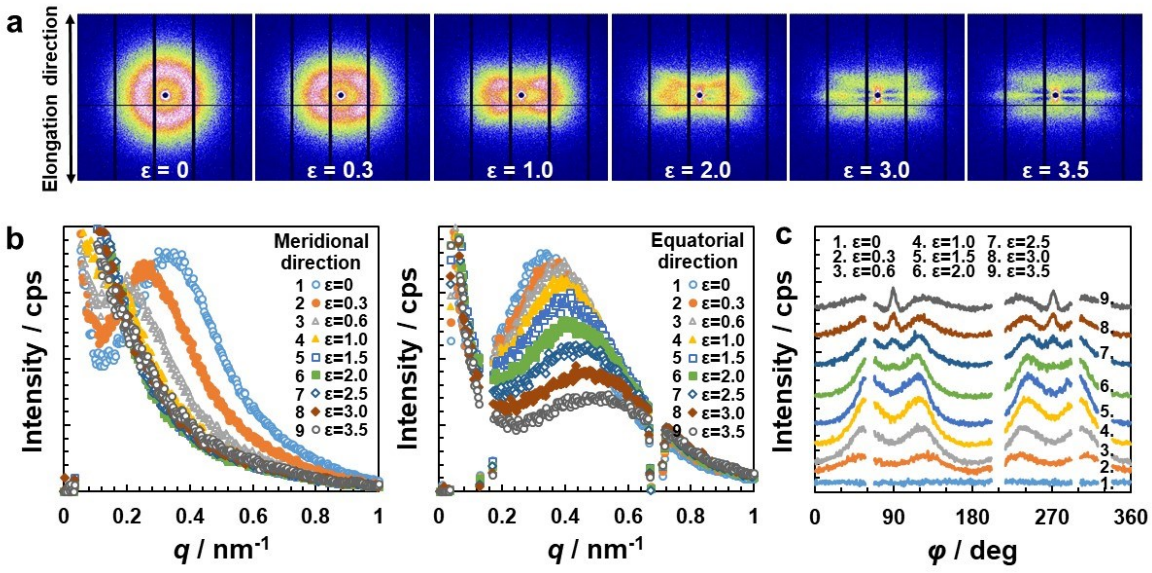

Figure 3.4 (a) 2D-SAXS patterns, (b) 1D meridional and equatorial SAXS profiles, and (c) azimuthal profiles of 2D-SAXS pattern at q=0.26-0.33 nm^{-1} for PTU-B at various strains.

the azimuthal intensity profiles of 2D-SAXS patterns at q 0.26-0.33 nm^{-1} at various strains for PTU-B. The elongation direction corresponds to the meridional direction in the 2D-SAXS patterns. At the initial state, one can see the ring-shaped 2D-SAXS pattern, suggesting the random orientation of the hard segment domains, with long-range correlation as a result of the microphase separation. This pattern becomes elliptical at the initial stage of elongation, indicating that the spacing between hard segment domains increased and decreased in the direction parallel and perpendicular to the elongation direction, respectively. At strain 0.3, a four-point scattering was observed at approximately 45° from the elongation direction (Figure 3.4b and 3.4c), which is

attributable to the tilted hard segment domains and crystals along the elongation direction. This four-point pattern caused by shearing mechanisms due to the local stress concentration induced by soft segment chains alignment. As strain increased, the four-point pattern tilted to 60° from the elongation direction, as shown in Figure 3.4c. At this stage, the hard segment domains and crystals inclination progressed and the periodic correlation of the hard segment domains is shifted.[3-31,32] The hard segment domains and crystals inclination continued until the soft segment extremely elongated. Furthermore, the equatorial streak occurred at strain 2.5, which is observed as a sharp peak at 90° and 270° in Figure 4c, suggesting a random correlation of scattering objects aligned in the direction of elongation, which is an indication of nanofibrils formation.[3-33~34] The decrease in the scattering intensity with increasing strain suggesting the decrease in population of scattering objects due to the hard segment domains fragmentation (see Figure 3.4b).[3-13] The strain dependence of orientation function for PTU elastomers is provided in Figure 3A.3. The hard segment domains and crystals of PTU-B shows random orientation at the initial state, which changes to parallel orientation to elongation direction with increasing strain.

Figure 3.5a shows the 2D-SAXS patterns for PTU-P during

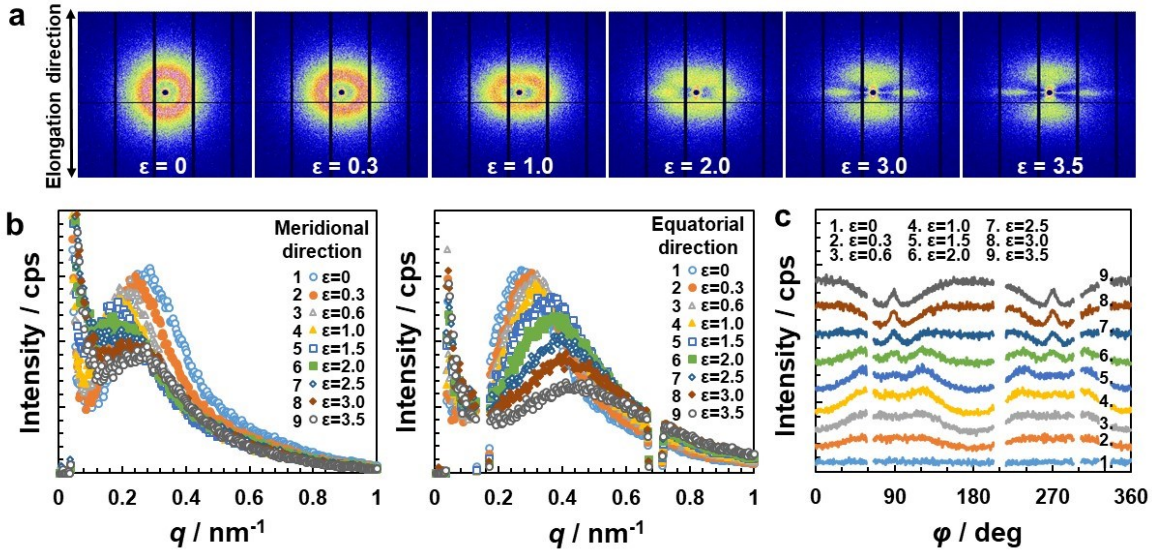

Figure 3.5 (a) 2D-SAXS patterns, (b) 1D meridional and equatorial SAXS profiles, and (c) azimuthal profiles of 2D-SAXS pattern at q=0.26-0.33 nm^{-1} for PTU-P at various strains.

uniaxial elongation. Figure 3.5b exhibits the 1D meridional and equatorial SAXS profiles, and Figure 3.5c exhibits the azimuthal intensity profiles of 2D-SAXS patterns at q 0.26-0.33 nm^{-1} at various strains for PTU-P. At the initial state, one can see the ring-shaped 2D-SAXS pattern, suggesting the random orientation of the hard segment domains. This pattern becomes elliptical with increasing strain, as presented in Figure 3.5a. At strain 1.0, a four-point pattern was observed at approximately 50° from the elongation direction (Figure 3.5b and 3.5c) and continued with increasing strain, indicating the tilted hard segment domains and crystals from the elongation direction. As strain increased, the four-point pattern tilted to 60° from the elongation direction, as

shown in Figure 3.5c. When the strain increased further, the equatorial streak occurred at strain 2.0, with its intensity increased with increasing strain. As well as PTU-B, it is also seen that the scattering intensity decreased with increasing strain (Figure 3.5b), suggesting the fragmentation of the hard segment domains. The shift of the scattering peak to higher q region after a gradual shift to lower q region can be explained as follows. Spacing of hard segment domains are observed, with the most frequent type possesses longer spacing with increasing strain up to strain 1.5. The peak shifted to higher q region with increasing strain, indicating that the hard segment domains with longer spacing undergo disruption.[3-35] Furthermore, PTU-P shows a gradual increase of the orientation of hard segment domains in the direction parallel to elongation direction, with a slightly lower magnitude compared to PTU-B. (Figure 3A.3).

Figure 3.6 shows the relation between film strain and strain obtained from spacing of hard segment domains of PTUs, $\Delta d/d$ during uniaxial elongation. d and d_s is the spacing of hard segment domains at the initial state and at a certain strain, respectively. Whereas, Δd is the change of spacing of hard segment domains, equal to d_s - d. Both PTU elastomers show increasing and decreasing trend in the $\Delta d/d$ with strain along meridional and equatorial directions, respectively. PTU-B

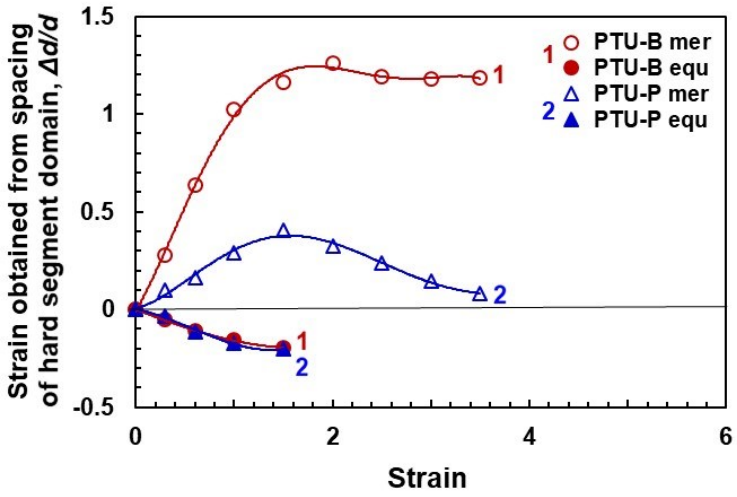

Figure 3.6 Strain obtained from spacing of hard segment domains, $\Delta d/d$ for PTU elastomers obtained from 1D-SAXS profiles at various strains, calculated using three-dimensional correlations functions.

exhibits an increment of the $\Delta d/d$ along the meridional direction which remains constant afterward. It is possibly that the hard segment domains maintained their aggregation structure due to the well-developed hard segment crystallites in PTU-B. On the other hand, PTU-P exhibits a decreasing trend in the $\Delta d/d$ along the meridional direction after reaching its peak at strain 1.5, suggesting significant fragmentation of hard segment domains due to the less ordered hard segment crystalline.[3-22] In addition, the equatorial $\Delta d/d$ decreased gradually with increasing strain for both PTU elastomers. This is because the hard segment domains tend to come closer toward each other, as a result of the hard segment domains destruction.[3-36]

In the WAXD patterns of PTU-B, the diffraction of hard

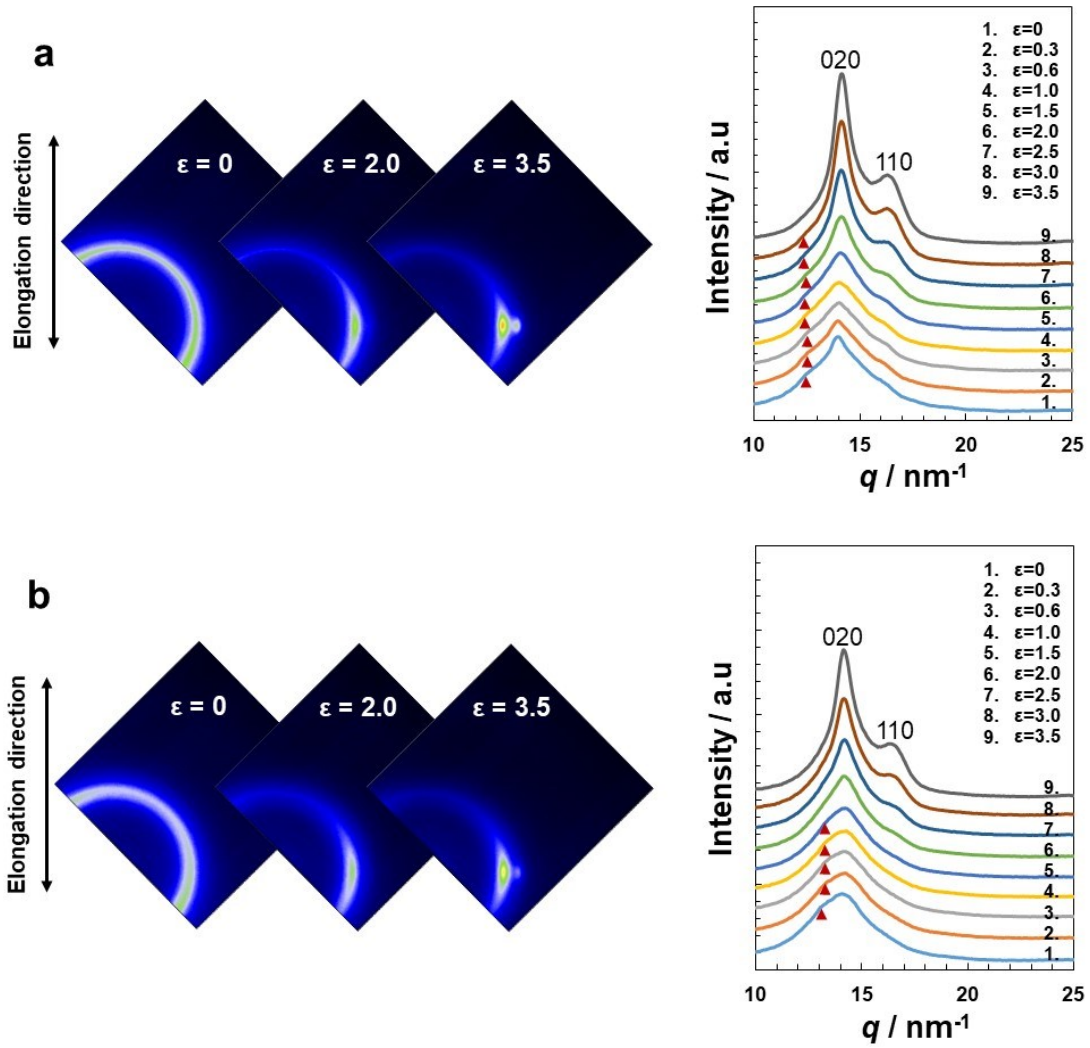

Figure 3.7 2D-WAXD patterns and 1D-WAXD profiles for (a) PTU-B, (b) PTU-P at various strains.

segment domains was observed at the initial state, namely at q=12.5, 14.2, and 16.4 nm^{-1}. They can be assigned to (10-2), (020), and (11-1) in the triclinic cell, respectively. Moreover, the strain-induced crystallization of soft segment chains occurred at around elongation 1.5. Two peaks assigned to crystallized PTMO chains were observed at q=14.2 and 16.8 nm^{-}

[1], which correspond with (020) and (110) in the monoclinic cell, respectively.[3-37] During uniaxial elongation, the diffraction peak of the (10-2) plane of hard segment domains in the PTU-B at q = 12.5 nm^{-1} became weaker at strain above 3.0. In contrast, the (020) and (11-1) lattice diffractions of PTU-B hard segment domains at q = 14.2 nm^{-1} and 16.4 nm^{-1}, respectively, were overlap with the crystallized PTMO chains, thus they cannot be observed. The change in the (10-2) inter-planar spacing suggesting the fragmentation of hard segment domains. This result correspond well with EXAFS data mentioned in the later section. The S-N_1 (r_3) distance shows remarkable change at strain 3.0 and 4.0.

On the other hand, at the initial state, PTU-P showed an amorphous halo and shoulder at q = 14.2 and 13.1 nm^{-1}, respectively, as shown in Figure 7b. This indicates the less ordered crystalline hard segment chains compared to PTU-B. The strain-induced crystallization of soft segment for PTU-P occurred at strain 2.0, with a lower intensity of diffraction peak than for PTU-B. This is due possibly to the lower alignment capability of the soft segment chains due to weak aggregation force of hard segment chains in PTU-P. [3-24,38,39]

After elongation, SAXS patterns returned to the initial state without intensity and WAXD patterns totally recover to the

initial state. Therefore, it is likely to consider that the hard segment domains had a small change in structure and the soft segment returned to the unoriented state after elongation.

3.3.2 XANES and EXAFS

To probe the atomic arrangement in the hard segment of PTUs, the XAFS measurements were conducted at various strains. Figure 3.8a shows the normalized sulfur K-edge X-ray absorption near-edge structure (XANES) spectra of PTU-B. The intense absorption peaks, called white lines, are shown in the sulfur K-edge XANES spectra of PTU-B at 2472 eV. These peaks correspond to the transition from S 1s to σ^*(S-C) with contribution from π^* character of the thiourethane carbonyl group.[3-40] An increase in the intensity of the white line and a slight shift of the absorption threshold (edge region) to lower energy with increasing strain were observed until strain 3.0. This can be associated with a rearrangement in the vicinity of sulfur and change in the S-C bond length, respectively,[3-41,42] with the most ordered structural arrangement of sulfur neighborhood achieved at strain 3.0.

Figure 3.8b shows the FT magnitude of experimental sulfur K-edge EXAFS spectra and the best fit model for PTU-B at various strains. The sulfur K-edge EXAFS spectra and

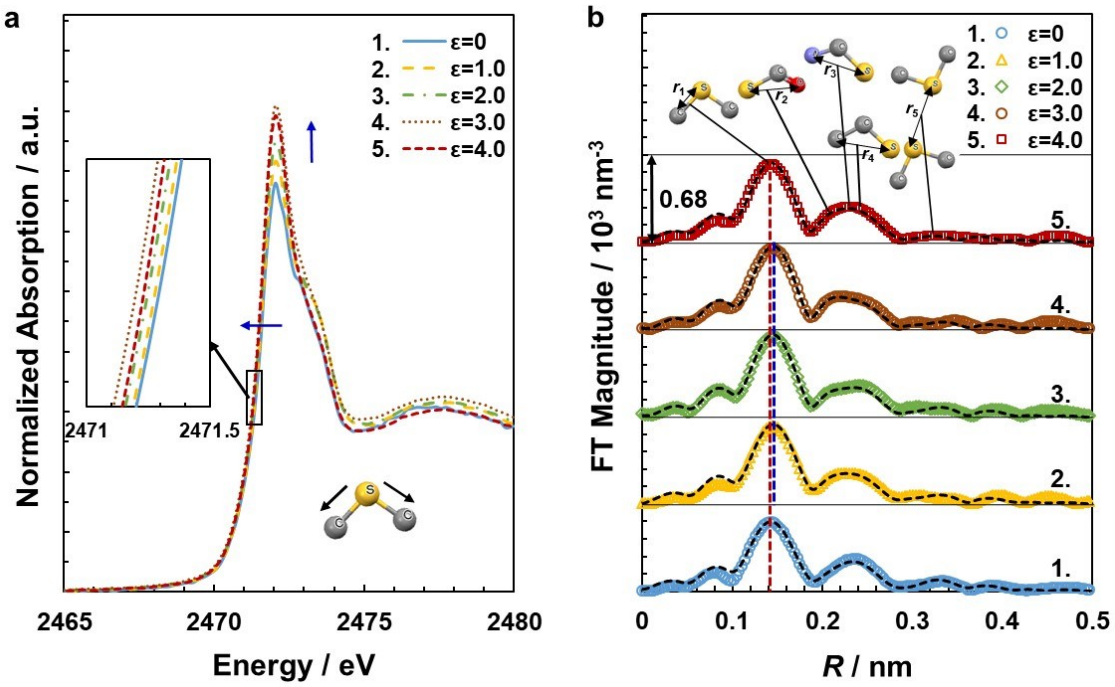

Figure 3.8 Sulfur K-edge (a) XANES and (b) EXAFS spectra (open symbol) and best fit model (dotted line) for PTU-B at various strains, measured at 25 °C.

individual scattering contribution for PTU-B can be seen in Figure 3A.4 a-e. To estimate the type of atoms that contribute to the EXAFS spectra and determine the reasonable values of the structural parameters, the hard segment crystal structure of 1,4-H_6XDI-1,4-BDT (Figure 3A.5a) was utilized. The obtained structural parameters for PTU-B are shown in Table 3A.1. The main peak of the PTU-B EXAFS spectra reflects the sulfur first coordination shell, with the position and magnitude related to the S-C bond length and disorder within this coordination shell, respectively.[3-41,43] As the strain increased to 3.0, a slight shift to higher *R* region and the gradual increase in the first peak

magnitude were observed. This is because the uniaxial elongation induces rearrangement in the vicinity of sulfur, thus decreasing the disorder within the first coordination shell. In other words, the uniaxial elongation increases the degree of ordered structure in the vicinity of sulfur. Since it is difficult to distinguish the modification of S-C bond length, the distribution of bond length is preferred to express as a static-disorder contribution to the EXAFS Debye-Waller factor. The EXAFS fitting results show a decrease in the EXAFS Debye-Waller factor with elongation until strain 3.0. Furthermore, at strain 4.0, the EXAFS Debye-Waller factor increased, indicating that the sulfur neighboring atoms can no longer maintain their ordered structure.

For the case of second coordination shell of sulfur, there are three single scatterings are involved, namely sulfur to oxygen carbonyl (S-O, r_2), sulfur to nitrogen (S-N, r_3), and sulfur to second-nearest carbon of methylene (S-C2, r_4). The uniaxial elongation not only affects the peak position and magnitude but also the shape of the second coordination shell. Although the number of scatterers that contributes to this peak is the same, the peak area of this second curve increased with increasing strain. The change in the peak position, magnitude, and shape are due to the change in the distance and angle between

sulfur and scattering atoms, which the distribution is not exactly in phase. Besides, the multiple scattering might give an additional contribution. It is to be mentioned that the FT is not same with a radial distribution function, for the reason that the number of scatterers would not be directly reflected the area under the curve due to the presence of the scattering factor $F_j(k)$, exponential damping factor ($e^{-2\sigma_j^2 k^2}$ and e^{-2r_j/λ_j}), and phase shift ($\delta_j(k)$) about -0.05 nm.[3-27,44,45] The increase in the magnitude of the second coordination shell with increasing strain is likely to occur due to the formation of a more ordered structure. However, the peak becomes poorly defined because of the magnitude attenuation. The EXAFS Debye-Waller factor tend to decrease until strain 3.0. It is, therefore, reasonable to conclude that uniaxial elongation increases the degree of ordered structure in the vicinity of the sulfur atom until strain 3.0. The third coordination shell of sulfur is contributed from sulfur to sulfur (S-S, r_5) single scattering, other single scattering and multiple scattering with lower contributions. However, the damping function at high r attenuates the amplitude exponentially, resulting in a very low magnitude of the FT.

Figure 3.9a shows the normalized sulfur K-edge XANES spectra of PTU-P. The white lines are observed at 2472 eV, indicating the transition from S 1s to σ*(S-C) with contribution

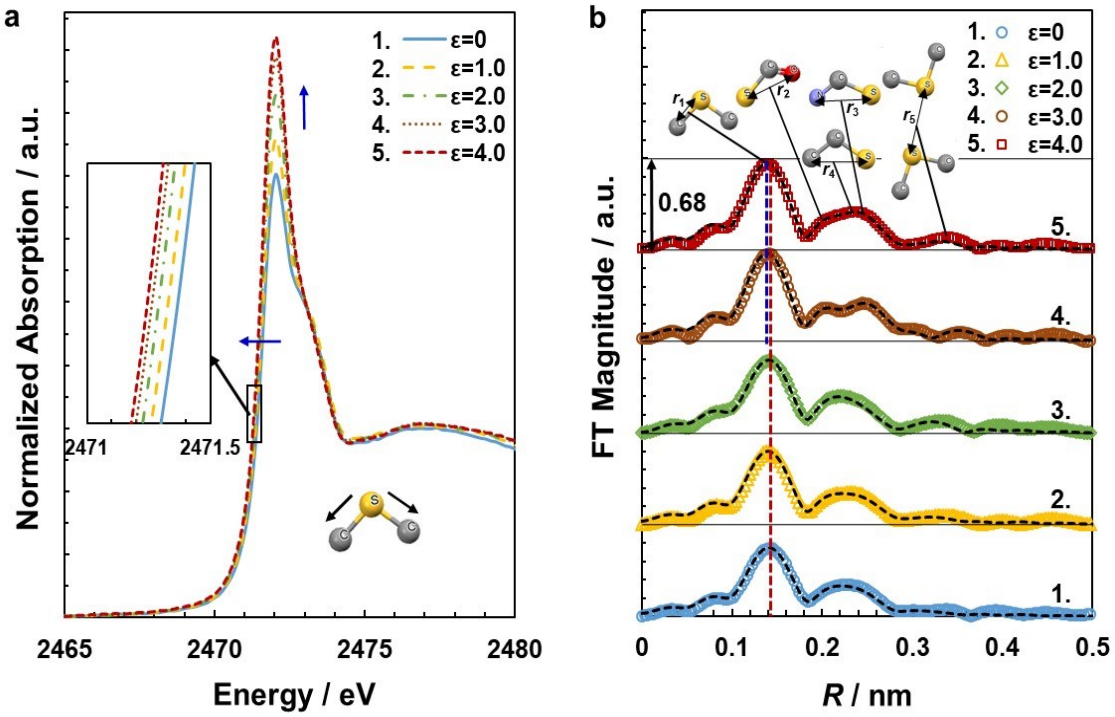

Figure 3.9 Sulfur K-edge (a) XANES and (b) EXAFS spectra (open symbol) and best fit model (dotted line) for PTU-P at various strains, measured at 25 °C.

from π^* character of the thiourethane carbonyl group. An increment in the intensity of white line and shift of the absorption threshold were greater than that for PTU-B. This can be explained that the lower degree of the ordered structure in the sulfur neighborhood of PTU-P becomes more ordered with increasing strain.

The FT magnitude of sulfur K-edge EXAFS spectra and the best fit model of PTU-P at various strains are shown in Figure 3.9b. The sulfur K-edge EXAFS spectra and individual scattering contribution for PTU-P can be seen in Figure 3A.4 f-j. The hard

segment crystal structure of 1,4-H_6XDI-1,5-PDT and the obtained structural parameters for PTU-P are provided in Figure 3A.5b and Table 3A.2, respectively. The main peak of the EXAFS spectra of PTU-P represents the sulfur first coordination shell. As the strain increased, a gradual increase in the first peak magnitude and a slight shift to lower *R* were observed, with more noticeable changes were detected at strain 3.0 and 4.0. This indicates an increase in the degree of ordered structure and change in the S-C bond length within the sulfur first coordination shell. PTU-P shows relatively higher values of EXAFS Debye-Waller factor for the first coordination shell of sulfur compared to PTU-B, which can be seen in Figure 3.10. This signifies that PTU-P possesses a less ordered structure in the sulfur nearest neighbor in comparison with PTU-B.

Moreover, the second coordination shell of sulfur is contributed from single scattering of sulfur to oxygen carbonyl (S-O, r_2), sulfur to nitrogen (S-N, r_3), and sulfur to second-nearest carbon of methylene (S-C2, r_4). The most obvious feature is the increase in peak magnitude and peak splitting at strain 3.0. This is because the rearrangement of the sulfur neighboring atoms leads to the more ordered structure of sulfur second coordination shell, which is confirmed by the decrease in Debye-Waller factor and increase in the high *R* distribution of sulfur

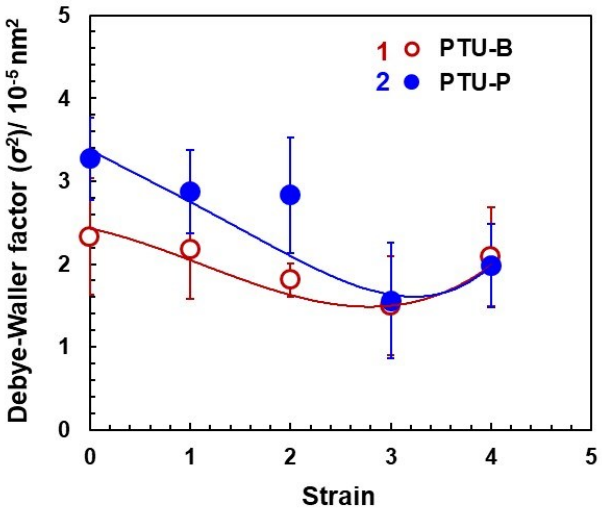

Figure 3.10 Strain dependence of EXAFS Debye-Waller factor for the first coordination shell of sulfur for PTU elastomers.

and scattering atoms. Furthermore, at strain 4.0, the sulfur neighboring atoms become less ordered, which is confirmed by the increase in the Debye-Waller factor. This is possibly due to the fragmentation of the hard segment domains. The third coordination shell of sulfur is contributed from sulfur to sulfur (S-S, r_5) single scattering, other single scattering and multiple scattering with lower contributions.

The schematic illustration as a proposed model for the molecular aggregation structure of PTUs during uniaxial elongation is provided in Figure 3.11. PTU-B exhibited random orientation of the hard segment domains at the initial state, with a rather shorter spacing of hard segment domains compared to PTU-P. As strain increased to 2.0, the hard segment domains of

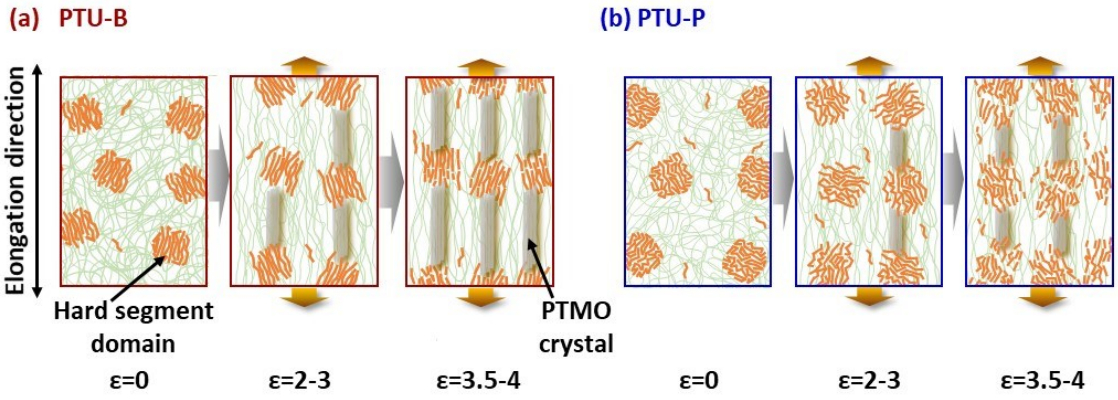

Figure 3.11 Schematic illustration of (a) PTU-B and (b) PTU-P during uniaxial elongation.

PTU-B shows parallel orientation to elongation direction. The spacing between hard segment domains in the direction parallel to elongation direction increased and remains constant after strain 2.0, whereas the spacing between hard segment domains in the direction perpendicular to elongation direction gradually decreased. On the other hand, PTU-P showed random orientation of hard segment domains at the initial state, which changes slightly with increasing strain up to 1.5. The spacing between hard segment domains in the direction parallel to elongation direction slightly increased and then decreased after reaching its peak at strain 1.5, whereas the spacing between hard segment domains in the direction perpendicular to elongation direction gradually decreased. At strain above 2.0, the orientation of hard segment domains of PTUs in the direction parallel to elongation direction increased, with higher magnitude observed in PTU-B.

The strain-induced crystallization of soft segment chains occurred at elongation of approximately 2.0. And finally, fragmentation of the hard segment domains is likely to occur as an indication of permanent deformation.

3.4 Conclusions

The deformation behavior of PTU elastomers was investigated using *in situ* synchrotron SAXS, WAXD, and XAFS spectroscopy. PTU elastomers (PTU-B or PTU-P) were prepared from PTMG, 1,4-H_6XDI and BDT or PDT. SAXS measurement revealed that the spacing of hard segment domains of PTUs increased in the directions of parallel to elongation direction and showed constant value above strain of 2. The strain obtained from the spacing of the hard segment domains for PTU-B was larger than for PTU-P, and Young's modulus and tensile strength of PTU-B were larger than for PTU-P, suggesting that well-developed hard segment domains were formed for PTU-B. The crystalline peaks were observed along perpendicular direction to elongation direction in WAXD patterns and Debye-Waller factor decreased at around strain of 2-3. Therefore, it seems reasonable to consider that ordering of hard segment chains occurred and then strain-induced crystallization of the soft segments subsequently occurred during the elongation process.

References

3-1) R. Bonart, *J. Macromol. Sci., Phys.,* **2**, 115-138, (1968).

3-2) R. Bonart, L. Morbitzer, G. Hentze, *J. Macromol. Sci., Phys.*, **10**, 345-357, (1974).

3-3) S.L. Cooper, A.V. Tobolsky, *J. Appl. Polym. Sci.*, **10**, 1837-1844, (1966).

3-4) "Polyurethane Elastomers", C. Hepburn, 2nd ed., Elsevier Applied Science, New York, (1992).

3-5) Z.S. Petrovic, J. Ferguson, *Prog. Polym. Sci.*, **16**, 695-836, (1991).

3-6) J.W.C. Bogart, P.E. Gibson, S.L. Cooper, *J. Polym. Sci., Part B: Polym. Phys.,* **21**, 65-95, (1983).

3-7) A. Takahara, J. Tashita, T. Kajiyama, M. Takayanagi, W.J. MacKnight, *Polymer*, **26**, 987-996, (1985).

3-8) S. Nozaki, S. Masuda, K. Kamitani, K. Kojio, A. Takahara, G. Kuwamura, D. Hasegawa, K. Moorthi, K. Mita, S. Yamasaki, *Macromolecules*, **50**, 1008-1015, (2017).

3-9) K. Kojio, M. Furukawa, S. Motokucho, M. Shimada, M. Sakai, *Macromolecules*, **42**, 8322-8327, (2009).

3-10) I. Yilgör, E. Yilgör, G.L. Wilkes, *Polymer*, **58**, A1-A36, (2015).

3-11) R.W. Seymour, A. Allegrezza Jr, S.L. Cooper, *Macromolecules*, **6**, 896-902, (1973).

3-12) G. Estes, R. Seymour, S.L. Cooper, *Macromolecules*, **4**, 452-457, (1971).

3-13) H.S. Lee, S.R. Yoo, S.W. Seo, *J. Polym. Sci., Part B: Polym. Phys.*, **37**, 3233-3245, (1999).

3-14) Y.S. Ding, R.A. Register, C.-z. Yang, S.L. Cooper, *Polymer*, **30**, 1221-1226, (1989).

3-15) H.K. Pan, D.J. Yarusso, G.S. Knapp, M. Pineri, A. Meagher, J.M.D. Coey, S.L. Cooper, *J. Chem. Phys.*, **79**, 4736-4745, (1983).

3-16) R.A. Register, M. Foucart, R. Jerome, Y.S. Ding, S.L. Cooper, *Macromolecules*, **21**, 1009-1015, (1988).

3-17) B. Grady, S.L. Cooper, *Macromolecules*, **27**, 6635-6641, (1994).
3-18) D.J. Yarusso, Y.S. Ding, H.K. Pan, S.L. Cooper, *J. Polym. Sci., Part B: Polym. Phys.*, **22**, 2073-2093, (1984).
3-19) J. Shin, H. Matsushima, J.W. Chan, C.E. Hoyle, *Macromolecules*, **42**, 3294-3301, (2009).
3-20) A. Kultys, M. Rogulska, S. Pikus, *J. Polym. Sci., Part A: Polym. Chem.*, **46**, 1770-1782, (2008).
3-21) M. Rogulska, A. Kultys, E. Olszewska, *J. Therm. Anal. Calorim.*, **114**, 903-916, (2013).
3-22) R. Rahmawati, S. Nozaki, K. Kojio, A. Takahara, N. Shinohara, S. Yamasaki, *Polym. J.*, **51**, 265-273, (2019).
3-23) H. Masunaga, H. Ogawa, T. Takano, S. Sasaki, S. Goto, T. Tanaka, T. Seike, S. Takahashi, K. Takeshita, N. Nariyama, H. Ohashi, T. Ohata, Y. Furukawa, T. Matsushita, Y. Ishizawa, N. Yagi, M. Takata, H. Kitamura, K. Sakurai, K. Tashiro, A. Takahara, Y. Amamiya, K. Horie, M. Takenaka, T. Kanaya, H. Jinnai, H. Okuda, I. Akiba, I. Takahashi, K. Yamamoto, M. Hikosaka, S. Sakurai, Y. Shinohara, A. Okada, Y. Sugihara, *Polym. J.*, **43**, 471-477, (2011).
3-24) K. Kojio, K. Matsuo, S. Motokucho, K. Yoshinaga, Y. Shimodaira, K. Kimura, *Polym. J.*, **43**, 692-699, (2011).
3-25) D.E. Sayers, E.A. Stern, F.W. Lytle, *Phys. Rev. Lett.*, **27**, 1204, (1971).
3-26) M. Newville, *Rev. Mineral. Geochem.*, **78**, 33-74, (2014).
3-27) "EXAFS: basic principles and data analysis", B.K. Teo, Springer Science & Business Media, (2012).
3-28) "XAFS for Everyone", S. Calvin, CRC Press, Boca Raton, (2013).
3-29) B. Ravel, M. Newville, *J. Synchrotron Radiat.*, **12**, 537-541, (2005).
3-30) J.T. Koberstein, R.S. Stein, *J. Polym. Sci., Part B: Polym. Phys.*, **21**, 1439-1472, (1983).
3-31) D.J. Blundell, G. Eeckhaut, W. Fuller, A. Mahendrasingam,

C. Martin, *J. Macromol. Sci., Phys.*, **43**, 125-142, (2006).
3-32) R.S. Waletzko, L.T.J. Korley, B.D. Pate, E.L. Thomas, P.T. Hammond, *Macromolecules*, **42**, 2041-2053, (2009).
3-33) F. Yeh, B.S. Hsiao, B.B. Sauer, S. Michel, H.W. Siesler, *Macromolecules*, **36**, 1940-1954, (2003).
3-34) C.R. Desper, N.S. Schneider, J.P. Jasinskit, J.S. Lin, *Macromolecules*, **18**, 2755-2761, (1985).
3-35) A. Stribeck, X. Li, A. Zeinolebadi, E. Pöselt, B. Eling, S. Funari, *Macromol. Chem. Phys.*, **216**, 2318-2330, (2015).
3-36) X. Li, Y. Lu, H. Wang, E. Pöselt, B. Eling, Y. Men, *Eur. Polym. J.*, **97**, 423-436, (2017).
3-37) K. Imada, T. Miyakawa, Y. Chatani, H. Tadokoro, S. Murahashi, *Macromol. Chem. Phys.*, **83**, 113-128, (1965).
3-38) Y. Higaki, K. Suzuki, Y. Oniki, K.L. White, N. Ohta, A. Takahara, *Polymer*, **78**, 173-179, (2015).
3-39) Y. Higaki, K. Suzuki, N. Ohta, A. Takahara, *Polymer*, **116**, 458-465, (2017).
3-40) E.D. Risberg, F. Jalilehvand, B.O. Leung, L.G. Pettersson, M. Sandström, *Dalton Trans.*, 3542-3558, (2009).
3-41) A.Y. Ramos, N.M. Souza-Neto, H.C. Tolentino, O. Bunau, Y. Joly, S. Grenier, J.-P. Itié, A.-M. Flank, P. Lagarde, A. Caneiro, *Europhys Lett.*, **96**, 36002, (2011).
3-42) N. Trcera, S. Rossano, K. Madjer, D. Cabaret, *J. Phys.: Condens. Matter*, **23**, 255401, (2011).
3-43) H.C. Choi, S.Y. Lee, S.B. Kim, M.G. Kim, M.K. Lee, H.J. Shin, J.S. Lee, *J. Phys. Chem. B*, **106**, 9252-9260, (2002).
3-44) "XAFS techniques for catalysts, nanomaterials, and surfaces", Y. Iwasawa, K. Asakura, M. Tada, Springer, (2017).
3-45) J.E. Penner-Hahn, *Coord. Chem. Rev.*, **190**, 1101-1123, (1999).

Appendix

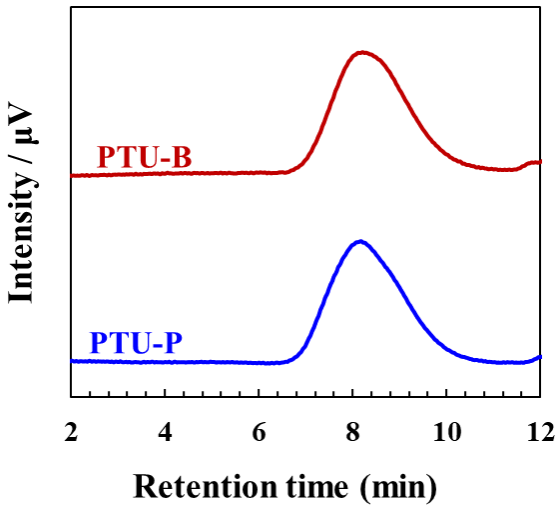

Figure 3A.1 GPC curves for PTU elastomers.

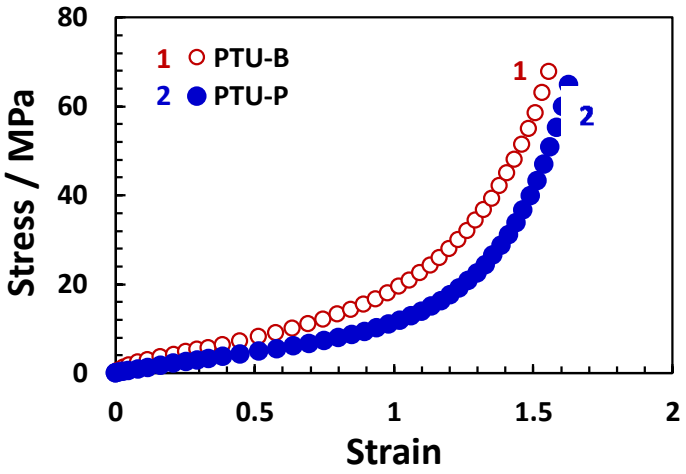

Figure 3A.2 True stress-true strain curves for PTUs during uniaxial elongation measured at 25 °C.

The orientation function, f, is calculated from the following equation:

$$f = \frac{3(cos^2\emptyset) - 1}{2}$$

where

$$(cos^2\emptyset) = \frac{\int_0^{\pi/2} I(\emptyset)\sin(\emptyset)cos^2(\emptyset)\, d\emptyset}{\int_0^{\pi/2} I(\emptyset)\sin(\emptyset)\, d\emptyset}$$

$I(\phi)$ and ϕ is the azimuthal intensity distributions and angle between a crystal axis and the deformation direction.

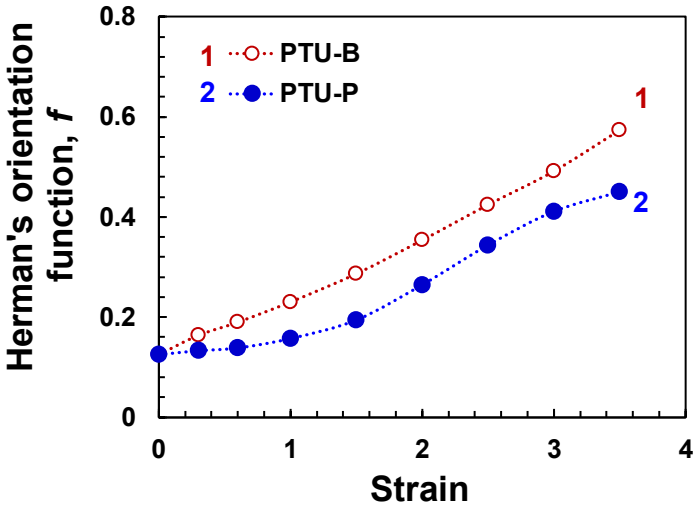

Figure 3A.3 Herman's orientation function for PTU elastomers obtained from azimuthal profiles of 2D-WAXD pattern at q=12.0-16.0 nm^{-1}.

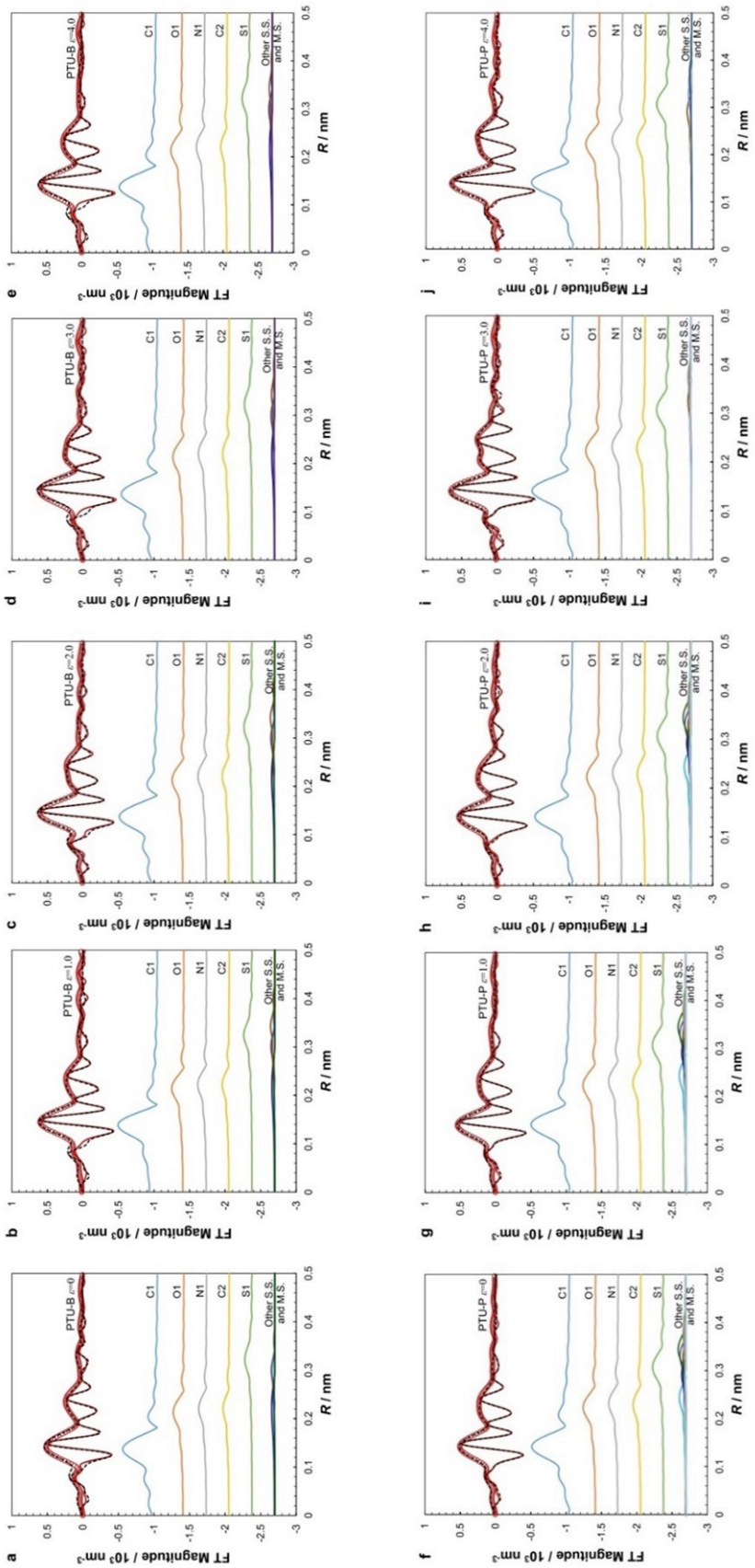

Figure 3A.4 Sulfur K-edge EXAFS spectra and individual scattering contribution for (a-e) PTU-B and (f-j) PTU-P.

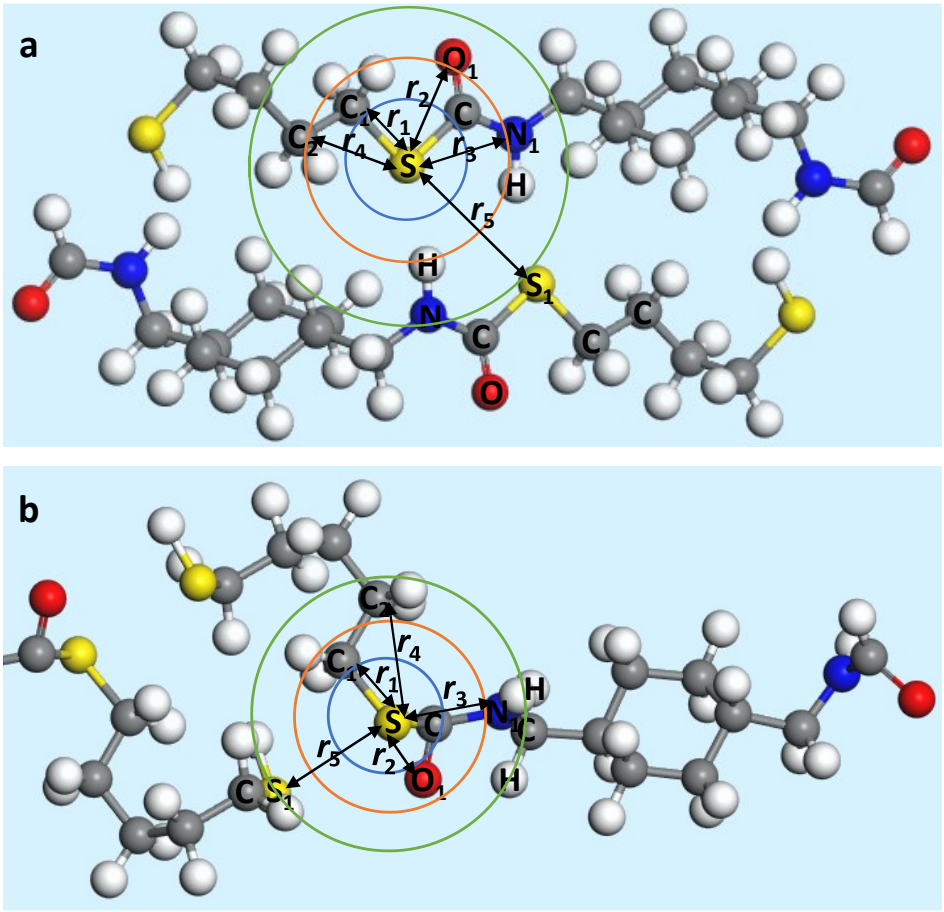

Figure 3A.5 Structure and structural changes with elongation for (a) 1,4-H_6XDI-1,4-BDT and (b) 1,4-H_6XDI-1,5-PDT hard segment.

Table 3A.1 Best-fit values determined for the S K-edge data for PTU-B obtained from EXAFS fitting. (5 most important scattering paths that contribute to PTU-B EXAFS spectra).

Sample	Path[a]	Degeneracy[b]	ΔR[c] (nm^{-1})	σ^2[d] (x10^{-5} nm^2)	
PTU-B ε=0	S-C1 (r_1)	2	0.184±0.001	2.33±0.7	ΔE_1[e]=9.6±1.9
	S-O1 (r_2)	1	0.262+0.009	8.61±0.9	ΔE_2=-2.4±1.7
	S-N1 (r_3)	1	0.264+0.009	2.38±0.6	S_0^2[f] = 0.8
	S-C2 (r_4)	1	0.269+0.007	2.33±0.7	
	S-S1 (r_5)	1	0.417+0.008	11.23±1.0	R-factor=0.019
PTU-B ε=1.0	S-C1 (r_1)	2	0.185±0.001	2.18±0.6	ΔE_1 = 10.9±1.6
	S-O1 (r_2)	1	0.257+0.007	8.23±0.9	ΔE_2 = -4.4±1.0
	S-N1 (r_3)	1	0.259+0.006	2.94±0.6	
	S-C2 (r_4)	1	0.270+0.007	2.18±0.6	
	S-S1 (r_5)	1	0.404+0.008	9.79±0.8	R-factor=0.022
PTU-B ε=2.0	S-C1 (r_1)	2	0.185±0.001	1.81±0.2	ΔE_1 = 11.6±1.8
	S-O1 (r_2)	1	0.253+0.008	8.27±1.0	ΔE_2 = -1.9±1.4
	S-N1 (r_3)	1	0.264+0.011	2.24±0.5	
	S-C2 (r_4)	1	0.271+0.008	1.81±0.2	
	S-S1 (r_5)	1	0.405+0.010	9.16±0.9	R-factor=0.025
PTU-B ε=3.0	S-C1 (r_1)	2	0.184±0.001	1.50±0.6	ΔE_1 = 9.3±1.2
	S-O1 (r_2)	1	0.256+0.010	4.88±0.4	ΔE_2 = -8.1±1.1
	S-N1 (r_3)	1	0.277+0.006	0.45±0.2	
	S-C2 (r_4)	1	0.262+0.004	1.50±0.6	
	S-S1 (r_5)	1	0.385+0.005	10.02±0.8	R-factor=0.015
PTU-B ε=4.0	S-C1 (r_1)	2	0.182±0.001	2.09±0.6	ΔE_1 = 8.1±1.4
	S-O1 (r_2)	1	0.256+0.006	1.81±0.3	ΔE_2 = -5.8±1.1
	S-N1 (r_3)	1	0.278+0.007	1.67±0.4	
	S-C2 (r_4)	1	0.265+0.006	2.09±0.6	
	S-S1 (r_5)	1	0.388+0.005	9.14±0.6	R-factor=0.014

[a] Path is defined as the photoelectron scattering path that originates at the absorbing atom (sulfur, S), continues to one or more neighboring atoms, and then returns to the absorbing atom. A single scattering path from the S atom to the 1st nearest neighboring C atom and then back to the original S atom is denoted as S-C1.

[b] The degeneracy of the path was held to the value obtained from X-ray diffraction of 1,4-H_6XDI-1,4-BDT hard segment.

[c] ΔR is the change in the half path length. A single scattering path has a half path length value equal to the distance between the absorbing atom and the neighboring atom.

[d] σ^2 is the mean-square relative displacement of the half path length. This value is a measure of the deviation or disorder for equivalent paths.

[e] ΔE is a shift to the photoelectron wave number.

[f] The amplitude reduction factor was fixed at 0.8.

Table 3A.2 Best-fit values determined for the S K-edge data for PTU-P obtained from EXAFS fitting. (5 most important scattering paths that contribute to PTU-P EXAFS spectra).

Sample	Path	Degeneracy[a]	ΔR (nm^{-1})	σ^2 (x10^{-5} nm^2)	
PTU-P ε=0	S-C1 (r_1)	2	0.183±0.001	3.27±0.5	ΔE_1 = 8.1±1.5
	S-O1 (r_2)	1	0.250+0.007	12.49±1.4	ΔE_2 = -9.8±1.0
	S-N1 (r_3)	1	0.260+0.007	3.40±0.4	S_0^2 [b] = 0.8
	S-C2 (r_4)	1	0.254+0.004	3.27±0.5	
	S-S1 (r_5)	1	0.321+0.003	5.95±0.2	R-factor=0.009
PTU-P ε=1.0	S-C1 (r_1)	2	0.183±0.001	2.87±0.5	ΔE_1 = 8.0±1.7
	S-O1 (r_2)	1	0.246+0.008	11.38±1.1	ΔE_2 = -8.6±1.9
	S-N1 (r_3)	1	0.261+0.007	2.25±0.4	
	S-C2 (r_4)	1	0.255+0.005	2.87±0.5	
	S-S1 (r_5)	1	0.323+0.004	5.88±0.3	R-factor=0.011
PTU-P ε=2.0	S-C1 (r_1)	2	0.183±0.001	2.83±0.7	ΔE_1 = 9.9±1.6
	S-O1 (r_2)	1	0.257+0.013	16.20±1.3	ΔE_2 = -3.8±1.4
	S-N1 (r_3)	1	0.261+0.005	2.61±0.6	
	S-C2 (r_4)	1	0.256+0.007	2.83±0.7	
	S-S1 (r_5)	1	0.326+0.005	7.23±0.6	R-factor=0.017
PTU-P ε=3.0	S-C1 (r_1)	2	0.181±0.001	1.56±0.7	ΔE_1 = 7.3±1.6
	S-O1 (r_2)	1	0.249+0.006	3.09±0.8	ΔE_2 = -4.6±1.6
	S-N1 (r_3)	1	0.264+0.007	1.53±0.1	
	S-C2 (r_4)	1	0.272+0.007	1.56±0.7	
	S-S1 (r_5)	1	0.327+0.003	3.29±0.3	R-factor=0.020
PTU-P ε=4.0	S-C1 (r_1)	2	0.182±0.001	1.98±0.5	ΔE_1 = 7.9±1.3
	S-O1 (r_2)	1	0.247+0.006	8.43±1.1	ΔE_2 = -5.7±1.8
	S-N1 (r_3)	1	0.263+0.004	1.06±0.5	
	S-C2 (r_4)	1	0.259+0.009	1.98±0.5	
	S-S1 (r_5)	1	0.326+0.005	3.85±0.3	R-factor=0.009

[a] The degeneracy of the path was held to the value obtained from X-ray diffraction of 1,4-H_6XDI-1,5-PDT hard segment.

[b] The amplitude reduction factor was fixed at 0.8.

Chapter 4

Structure-Property Relationship in Carboxylated Polyurethane Ionomers Based on Cycloaliphatic Diisocyanate

4.1 Introduction

Polyurethane ionomers (PUIs) have attracted considerable attention due to their potential use for adhesives, dental cement, coatings, and sealants. Besides, PUIs have also received research interest as conductive polymers and biomedical elastomers.[4-1~7] PUIs were prepared from polyol, diisocyanate, and at least one ion-containing diol chain extender. The energetic incompatibility between polar ionic groups and the nonpolar polymer back bond generates aggregation of ionic groups into ionic rich domains, called ion multiplets, which may grow larger become ion clusters. This aggregates act as reinforcing fillers, thermally reversible crosslinks, and ion transport pathways that have a prominent effect on the mechanical and transport properties of PUIs.[4-8~11] To attain rationale engineering and design of the above-mentioned polymer for specific applications, a comprehensive understanding of structure-properties relationship is highly desired.

In this investigation, cycloaliphatic diisocyanate-based PUIs bearing carboxylic acid groups were employed. Neutralization of these acid groups with metal salts drives specific interactions between ionic groups that contribute to microphase separation. The objective of this work is to study the effect of degree of neutralization on the aggregation structure

and mechanical properties of these PUIs.

4.2 Experimental

4.2.1 Materials

Poly(oxytetramethylene) glycol (PTMG: M_n = 1800, Asahi Kasei Chemicals Co., Ltd., Japan) and 1,4-bis(isocyanatomethyl)cyclohexane (FORTIMO^{TM} 1,4-H_6XDI, produced by Mitsui Chemicals Inc.) were employed as polyol and diisocyanate, respectively. 2,2-bis(hydroxymethyl) propionic acid (DMPA) and 1,4-butanediol (BD) (FUJIFILM Wako Pure Chemicals Co., Ltd., Japan) were used as chain extenders. BD chain extenders were purified by distillation, whereas 1,4-H_6XDI was used without further purification. Figure 4.1 shows the chemical structures of PTMG, 1,4-H_6XDI, DMPA, and BD.

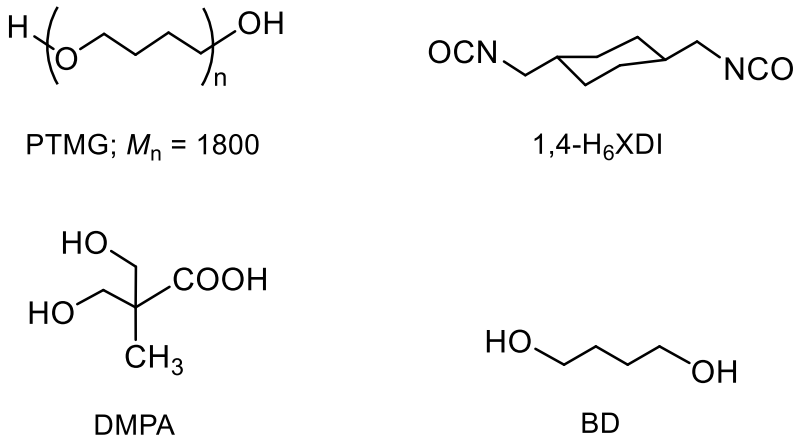

Figure 4.1 Chemical structures of PTMG, 1,4-H_6XDI, DMPA, and BD.

4.2.2 Synthesis of PU Ionomers

Figure 4.2 shows the reaction scheme for PUI using a two-step method and the chemical structure of PUI-DMPA-Zn. PUIs were prepared by a two-step method under a nitrogen atmosphere. PTMG was dried at 80 °C for 3 hours under reduced pressure prior to use. Initially, PTMG and 1,4-H_6XDI were reacted in acetonitrile solution at 75 °C with a dibutyltin dilaurate (DBTL, FUJIFILM Wako Pure Chemical Co., Ltd. Japan) as a catalyst and

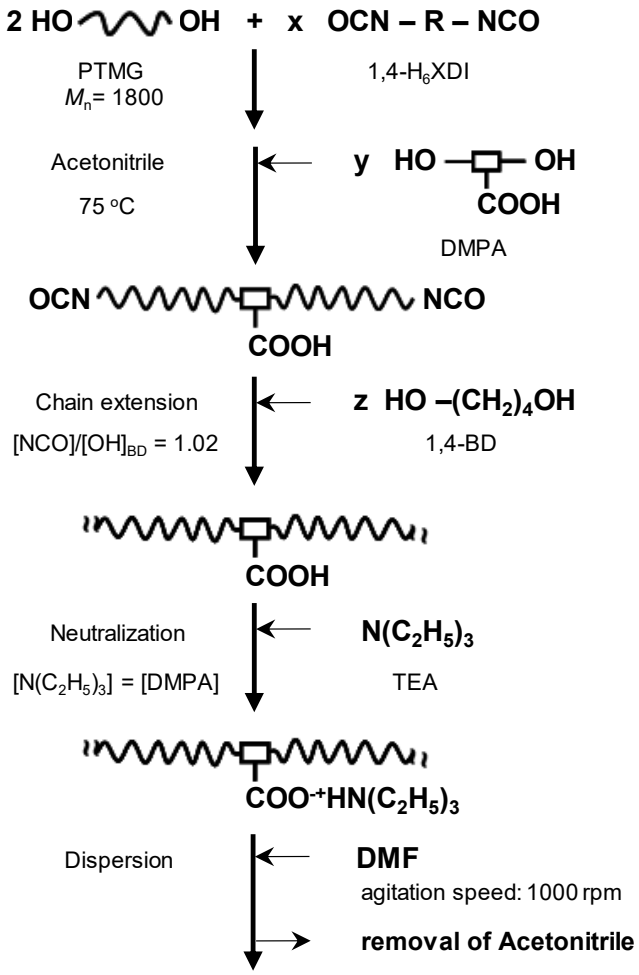

Figure 4.2 Reaction scheme for PUI using a two-step method.

stirred with a mechanical stirrer. DMPA was dissolved in acetonitrile and added into the flask. A total amount of PTMG, 1,4-H_6XDI, DMPA, and BD was approximately 40 wt%. The fractions of the hard segment were ca. 22 wt%. The NCO value during the reaction was observed using an amine equivalent method, and, then, stopped when the reaction ratio for the NCO groups reached over 90%. Furthermore, polymer chains were extended using BD, followed by the addition of triethylamine to neutralize DMPA acidic groups. The obtained polymer was dispersed in DMF with agitation speed 1000 rpm followed by removal of acetonitrile. The PUI with M_n = 50,000 g mol^{-1} contained 11.8 mol % DMPA units in the backbone, therefore the average number of backbone carbons between two neighboring COOH groups is approximately 43. A series of carboxylated-PUIs were prepared by using Zn^{2+} as a neutralizing cation.

4.2.3 Evaluation of Gel Fraction and Degree of Swelling

The gel fraction and degree of swelling were evaluated using N,*N*-dimethylacetamide (DMAc) and toluene as a polar and nonpolar solvent, respectively. The gel fraction, G, was defined as $G = W_b/W$, where W is the initial weight, and W_b is the dried weight after swelling with a solvent. The degree of swelling, Q, was defined as $Q = 1 + [(W_a - W_b)/d_s/(W_b/d_p)]$, where W_a, d_s, and d_p

is the weight of the samples swollen to an equilibrium state, density of the solvent and density of the elastomers, respectively.

4.2.4 Evaluation of Ionic Aggregation Structure

The hydrogen bonding state of the PU ionomers was assessed by a Fourier transform infrared (FT-IR) spectroscopic measurement. A Spectrum One FT-IR spectrometer (PerkinElmer), Mercury cadmium telluride (MCT) detector, and attenuated total reflectance (ATR) accessory (Ge crystal, 45°) were employed for measurements. All FT-IR spectra were acquired at a resolution of 4 cm^{-1} with 32 scans.

Differential scanning calorimetric (DSC) thermograms were obtained using a DSC (DSC6220, SII EXSTAR 6000, Seiko Instruments) from -130 to 250 °C with a heating rate of 10 °C min^{-1} under a N_2 atmosphere.

The synchrotron radiation X-ray at the Frontier Softmaterial Beamline (FSBL, BL40XU) in the SPring-8 facility Japan was utilized to evaluate the ionic aggregation structure.[4-12,13)] The wavelength and size of the X-ray beam was 0.1 nm and 250 μm x 40 μm. A PILATUS 1 M (DECTRIS, Ltd., pixel size of 172 μm) was used to obtain scattering in the small-angle region with a camera length of ca. 2 m. A flat panel detector was employed for WAXD measurements with a camera length of 84

mm. Scattering patterns were measured with an exposure time of 200-500 ms. Data were processed using the FIT-2D (Ver. 12.077, Andy Hammersley/ ESRF, Grenoble, France).

4.2.5 Evaluation of Mechanical Properties

Temperature dependence of dynamic viscoelastic functions were obtained with a dynamic viscoelastometer (RHEOVIBRON DDV-01FP, ORIENTEC). Measurements were performed from -150 to 150 °C with a heating rate of 1 °C min^{-1} under N_2 atmosphere. The dimension of the specimens used was 30 mm x 5 mm x 0.3 mm. The applied frequency was 11 Hz.

Tensile testing was carried out with EZ-Graph (Shimadzu, Japan) at room temperature. The dimension of the samples was 50 mm x 5 mm x 0.3 mm. The initial length and elongation rate were 30 mm and 10 mm min^{-1}, respectively.

4.3 Results and Discussion

4.3.1 Gel Fraction and Degree of Swelling

The abbreviation of the PUIs denotes the polymer, ionic chain extender, and metal cation and its weight fraction, respectively. Table 4.1 shows the density, gel fraction, and degree of swelling of the PU ionomers. The swelling test was performed to evaluate the network structure of PUIs. When a

Table 4.1 Density, Gel Fraction, and Degree of Swelling of PU Ionomers

Sample[a]	Density ($g\ cm^{-3}$)	Gel fraction, G (%)		Degree of swelling, Q	
		Toluene	DMAc	Toluene	DMAc
PUI-DMPA-Zn0.0wt%	1.04	97.2±0.3	Soluble	5.8±0.04	Soluble
PUI-DMPA-Zn0.6wt%	1.04	97.8±0.5	Soluble	4.5±0.04	Soluble
PUI-DMPA-Zn1.1wt%	1.04	97.6±0.4	Soluble	4.3±0.05	Soluble

[a] Zn0.0, Zn0.6, and Zn1.1 denotes metal cation and its weight fraction.

polymer is immersed in a certain solvent, the solvent molecules slowly diffuse into the polymer and the swelling of the polymer can take place. The degree of swelling means how much solvent that can be absorbed by PUIs. Whereas, the gel fraction means how much molecules are integrated into the network structure. The gel fraction of all ionomers swollen by toluene was approximately 97%, indicating that the physical crosslinking network is well-developed. Whereas, all samples were soluble in DMAc, implying the existence of physical crosslinks that undergo dissociation in the polar solvent. The degree of swelling in toluene decreased with increasing zinc content, resulting in the formation of well-developed domains.

4.3.2 Ionic Aggregation Structure

Figure 4.3 shows the ATR-FT-IR spectra for the PU ionomers. The NCO stretching band at 2260 cm^{-1} was not

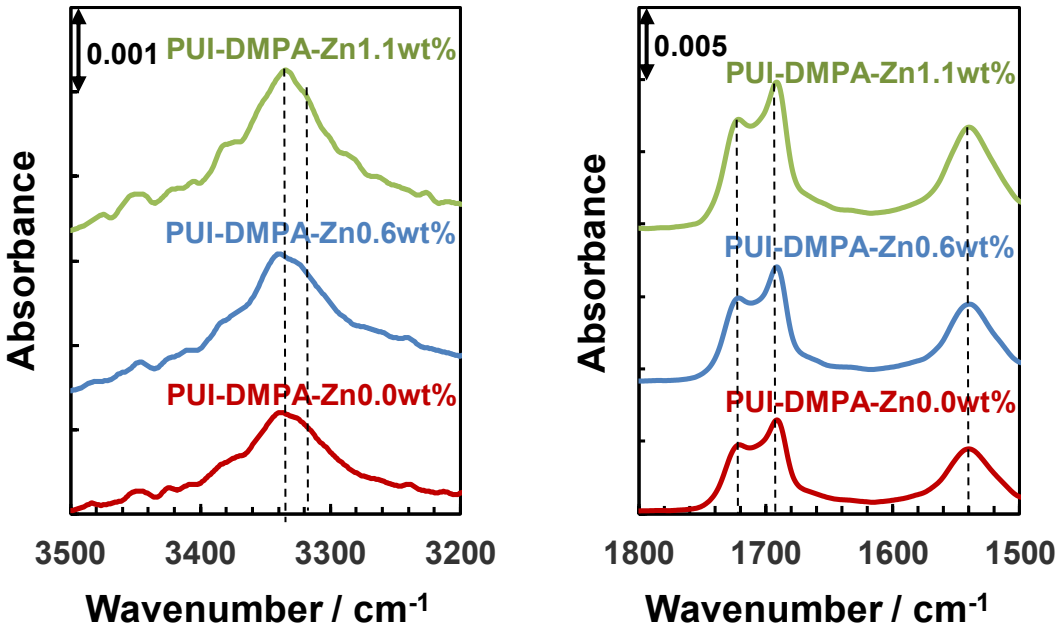

Figure 4.3 ATR-FT-IR spectra of PU ionomers. (a) NH stretching (ν(NH), (b) C=O stretching (ν(C=O) and carboxylate (ν(COO-)) ions bands.

observed in all spectra, suggesting that the reaction occurred properly. Absorption bands at approximately 1720, 1690, and 1535 cm^{-1} correspond to urethane carbonyl free ($\nu(C=O)_{U\text{-}free}$), hydrogen-bonded carbonyl groups of urethane ($\nu(C=O)_{U\text{-}H\text{-}bond}$) stretching vibrations, and asymmetric carboxylate stretching vibration ($\nu(COO^-)$) of the tetrahedral structure of the tetra-coordinated zinc carboxylate multiplet, respectively, as can be seen in Figure 4.4. The absorption of ($\nu(COO^-)$) stretching vibrations increase, indicating more tetra-coordinated zinc carboxylate formed with increasing zinc content. Ion incorporation has a slight effect on the hydrogen bonding

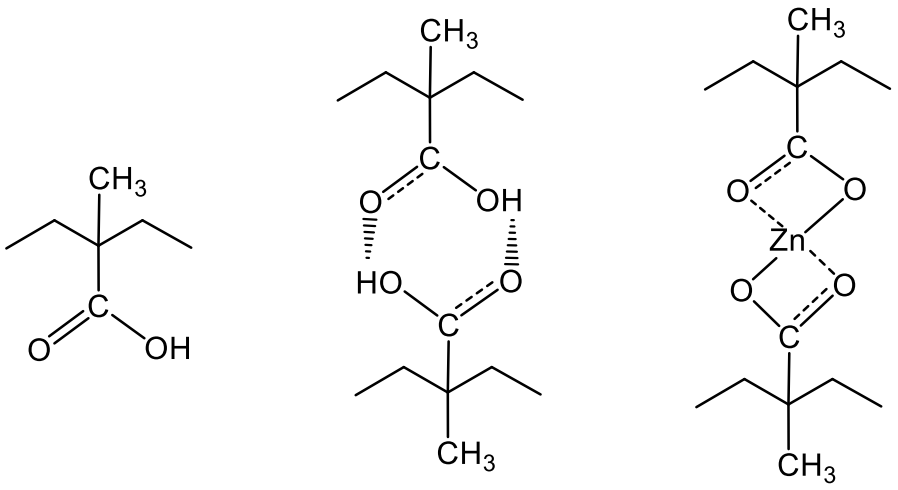

Figure 4.4 Schematic representation of structures near carbonyl groups. (a) urethane carbonyl free, (b) hydrogen-bonded carbonyl groups of urethane, and (c) tetra-coordinated zinc carboxylate.

characteristic of PUI-DMPA-Zn. In the region 3200-3500 cm^{-1}, the NH band seems almost totally hydrogen bonded. The stretching vibrations of NH-bonded ($\nu(NH)_{U\text{-}H\text{-}bond}$) at approximately 3340 cm^{-1} appears in the majority, whereas the NH-free (ν(NH)free) is hardly recognizable.[4-14~16)]

DSC thermograms for PUIs are shown in Fig. 4.5. The glass transition temperature of the soft segment chains was observed in the range -69 to -74 °C. The T_g of the soft segment decreased with increasing zinc content, suggesting that the degree of microphase separation becomes stronger. The variation in the T_g of soft segment reflects changes in the extent of microphase separation, because the short sequences of the hard

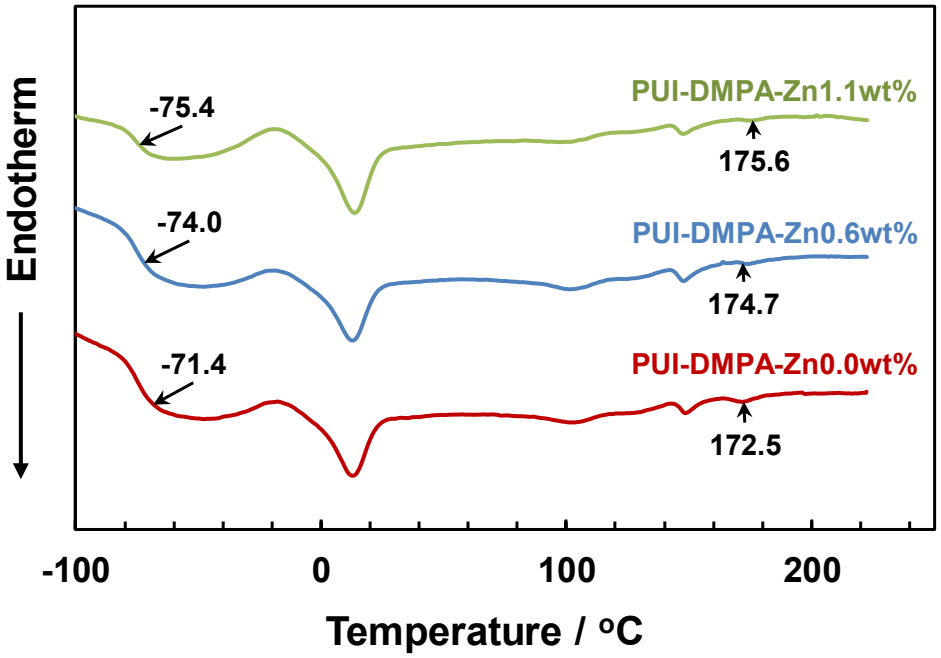

Figure 4.5 DSC thermograms for the PU ionomers.

segment may dissolve in the soft segment and raise its T_g. The broad endotherm peak at 90-110 °C can be assigned to the dissociation of noncrystalline hard segment aggregates. This is because the existence of a methyl side group of DMPA does not allow compact ordering of hard segment.[4-17] Two melting temperature of the hard segment domains were observed at 150 and 170 °C, which corresponds to the melting of the crystallized hard segment domains and ionic clusters. Increasing zinc content improves ionic aggregation, as indicated by the endotherm peak moving to higher temperatures.[4-14]

The scattering data of PUI-DMPA-Zn were modeled with a combination of two functions:

$$I(q) = I_{YC}(q) + L(q) \quad (4.1)$$

where $I_{YC}(q)$ is the Yarusso-Cooper modified hard-sphere model[4-18] used to interpret the ionomer peak, and $L(q)$ is the Lorentzian function used to fit the non-ionic hard segment peak. The Levenberg-Marquardt algorithm[4-19] in R programming language[4-20] was used for curve fitting. The Yarusso-Cooper modified hard-sphere model[4-18] treats the ionic aggregates as spherical particles with an ionic core having radius R_1. In this case, the ionic aggregates are not allowed to interact with each other. The mobility of ionic aggregates is restricted by a shell with radius R_{CA} defined from the center of each aggregate, where the closest approach distance between two aggregates is $2R_{CA}$. The average sample volume per aggregate is defined as V_p. The X-ray scattering intensity is depicted by

$$I(q) = I_e(q)V\frac{1}{V_p}V_1^2\rho_1^2\phi^2(qR_1)\frac{1}{1+(8V_{CA}/V_p)\epsilon\phi(2qR_{CA})} \quad (4.2)$$

$$V_{CA} = \frac{4}{3}\pi R_{CA}^3 \quad (4.3)$$

$$V_1 = \frac{4}{3}\pi R_1^3 \quad (4.4)$$

$$\phi(x) = 3\frac{sinx - x\,cosx}{x^3} \quad (4.5)$$

where $I(q)$ is the observed intensity and $I_e(q)$ is the intensity scattered by a single electron under the experimental conditions, V is the volume of the sample, ρ_1 is the electron density

difference between the matrix and the ionic aggregate, and ϵ is a constant close to unity. Since $I_e(q)$ can be regarded as a constant, the term $I_e(q)V\rho_1^2$ can be considered as a single adjustable parameter. Thus, the model has four fitting parameters, namely R_1, R_{CA}, V_p, and $I_e(q)V\rho_1^2$. By fitting calculated scattering data to the experimental data, a combination of ionic aggregates parameters can be determined. Whereas, the Lorentzian function which accounts for the non-ionic hard segment domains contribution is described by

$$y = \frac{A_L.\kappa^2}{(q-q')^2+\kappa^2} \tag{4.6}$$

where A_L is the peak amplitude, q' is the peak position, and κ is the half-width at half-maximum. The R-squared parameter (a measure of how well a model fits the scattering data, equation 4.7) is approximately 0.99. This reveals that the scattering data and model are in a good agreement.

$$R^2 \equiv 1 - \frac{\sum_i (y_i - f_i)^2}{\sum_i (y_i - \bar{y})^2} \tag{4.7}$$

The SAXS data for PU ionomers and fits to the combined Yarusso-Cooper-Lorentzian model are shown in Figure 4.6 and the obtained parameters are presented in Table 4.2. The radius of the ionic core, R_1, somewhat change with increasing degree of neutralization, whereas, the more notable increase was observed

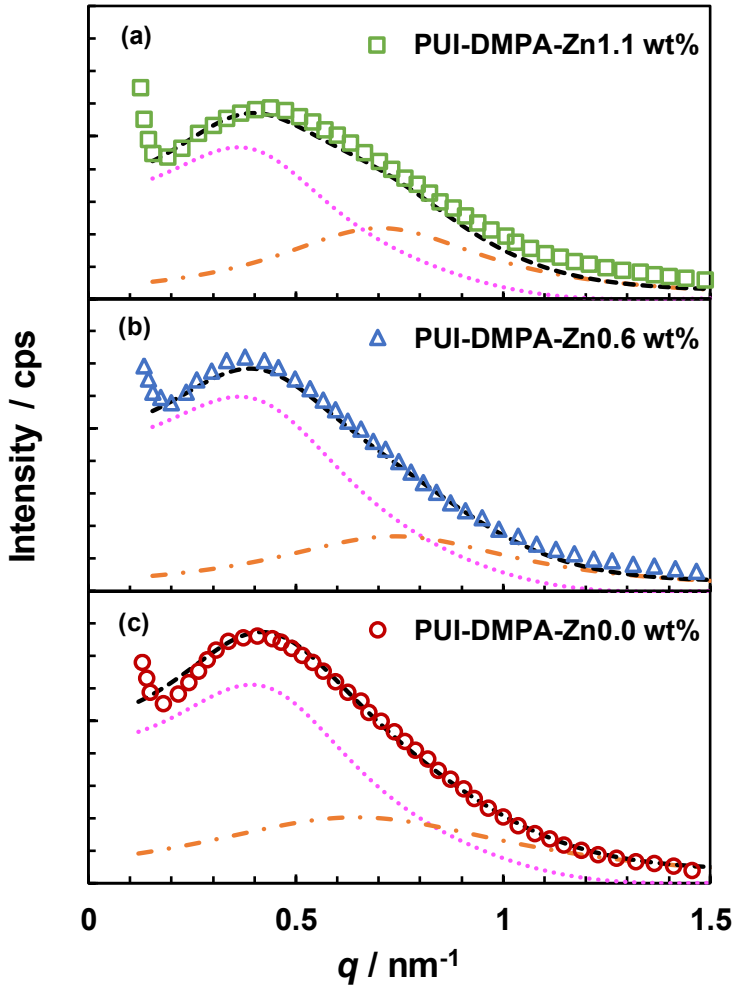

Figure 4.6 SAXS data for PU ionomers. (a) PUI-DMPA-Zn1.1wt%, (b) PUI-DMPA-Zn0.6 wt%, and (c) PUI-DMPA-Zn0.0 wt%. Open symbols are experimental data, black dashed lines are fits to combined YC-Lorentzian model, pink dotted lines are YC contributions, and orange dashed and dotted lines are Lorentzian contributions.

in the R_{CA}. V_p becomes larger with increasing degree of neutralization, as well as the increase in R_1 and R_{CA}. The increase in the R_1 reflects the increase in the number of ions forming the ionic aggregates. On the other hand, the hydrocarbon

layer surrounding ionic aggregates become thicker with increasing R_1.

Table 4.2 Best-Fit Parameters of the combined Yarusso-Cooper-Lorentzian Model for the PUIs

Sample	R_1 / nm	R_{CA} / nm	V_p / nm^3	q' / nm^{-1}
PUI-DMPA-Zn0.0wt%	3.15	5.58	6.30 x 10^3	0.65
PUI-DMPA-Zn0.6wt%	3.25	5.71	7.09 x 10^3	0.74
PUI-DMPA-Zn1.1wt%	3.37	6.10	7.50 x 10^3	0.70

This indicates that the size of ionic aggregates become larger with increasing degree of neutralization. The non-ionic hard segment domains show a slight change in the spacing between hard segment domains with increasing degree of neutralization, suggesting that the addition of Zn^{2+} not only affects the ionic aggregation structure but also the non-ionic microphase-separated structure.

4.3.3 Mechanical Properties

The storage modulus, loss modulus, and tan δ are plotted as a function of temperature for PUIs in Figure 4.7. The γ-relaxation is observed at approximately -120°C, which is attributed to the relaxation of the methylene sequences of PTMG. A fast decrease in storage modulus and a peak in the loss modulus

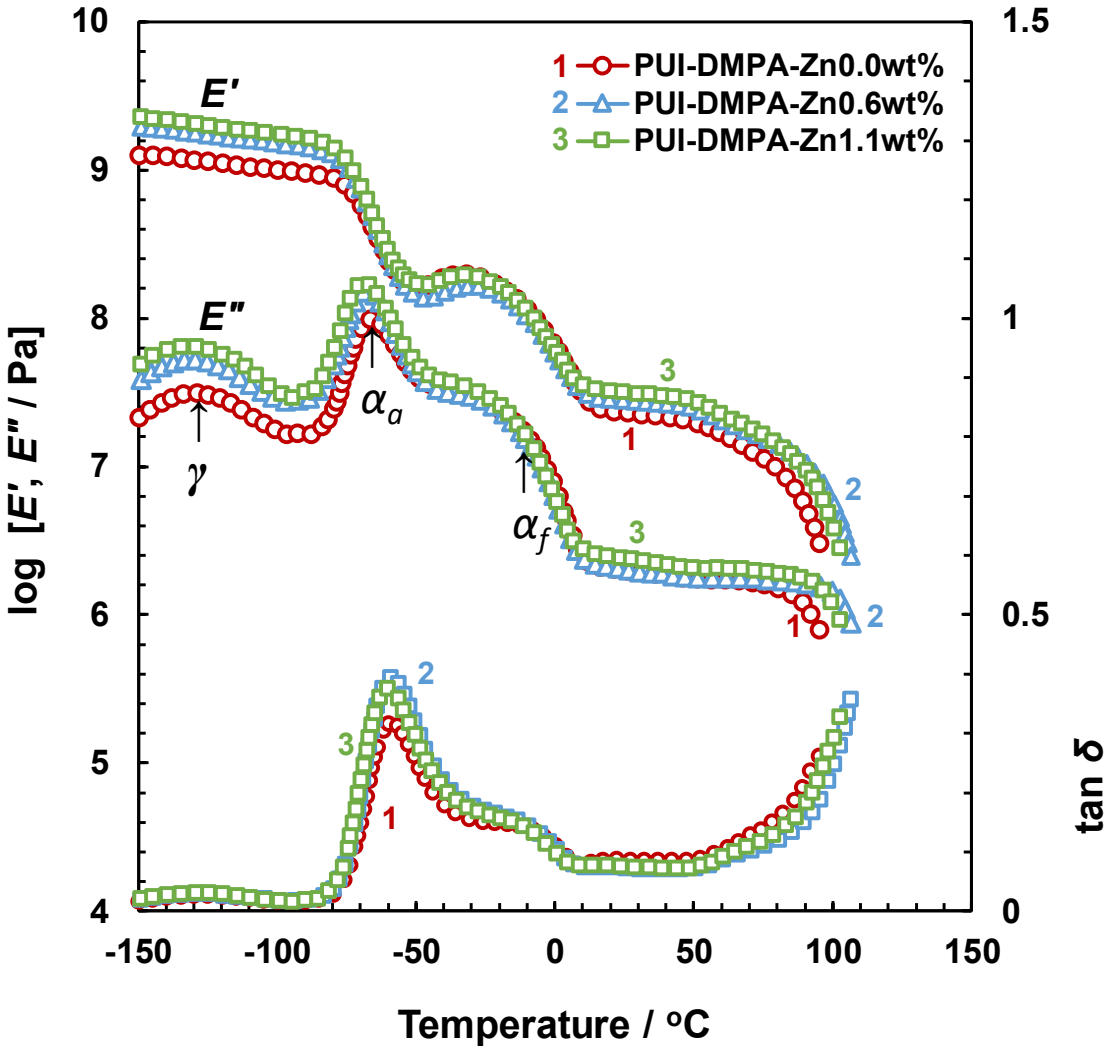

Figure 4.7 Dynamic viscoelastic properties of the PU ionomers measured at 11 Hz.

are assigned to α_a-absorption arised from micro-Brownian segmental motion of amorphous PTMG associated with the glass transition. Assuming that the relationship between shift factor, a_T, and measuring temperature is Arrhenius type, the apparent activation energy for the α_a-relaxation process, ΔH_α^*, can be calculated from the slope of Arrhenius plot as mentioned in

chapter 2. The activation energy for the α_a-relaxation process for PUIs is 187-201 kJ.mol^{-1}, which was in excellent accordance with ΔH_α^* of 1,4-HXDI-based PU and MDI-based PU. The α_f-absorption was observed as a shoulder on the higher temperature side of the α_a peak for PTUs and PUs, at approximately -20 °C. This peak is related to the melting process of the crystalline phase of PTMG.[4-21~22)]

The glass transition temperature of the soft segment decrease with increasing degree of neutralization, which is attributed to increasing phase separation. All samples exhibit a rubbery plateau region ranging from approximately 10 to 90 °C. This plateau region extends and the plateau modulus rises with increasing degree of neutralization, indicating an enhancement of the ionic aggregation and physical crosslinking.[4-14,23)] These results are in good agreement with the DSC data.

The stress-strain curves for PU ionomers are presented in Figure 4.8. The modulus of these ionomers increases with increasing degree of neutralization, which is consistent with the magnitude of *E'* at the rubbery plateau region. Tensile strength and extensibility of PUIs are improved with increasing degree of neutralization.

The reason for the properties of PUIs is attributed to the development of ionic aggregates acting as physical crosslinking points. The upturn in stress at large strain suggesting that the strain-induced crystallization of soft segment occurred.

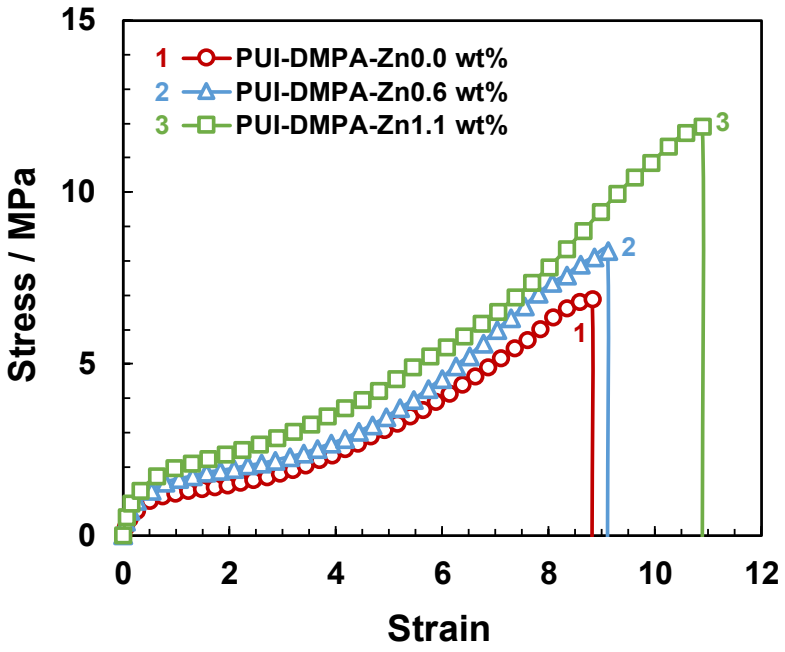

Figure 4.8 Stress-strain curves for PU ionomers measured at 25 °C.

Figure 4.9 shows the schematic representation of the ionic aggregation structure of PU ionomers. Increasing degree of neutralization in PUIs increased the size of ionic aggregates, the thickness of the restricted mobility layer, and enhanced the ionic aggregation structure.

Besides, the spacing between non-ionic hard segment domains slightly changes with increasing degree of neutralization. Both ionic and non-ionic phase-separated structure influence the mechanical properties of PU ionomers.

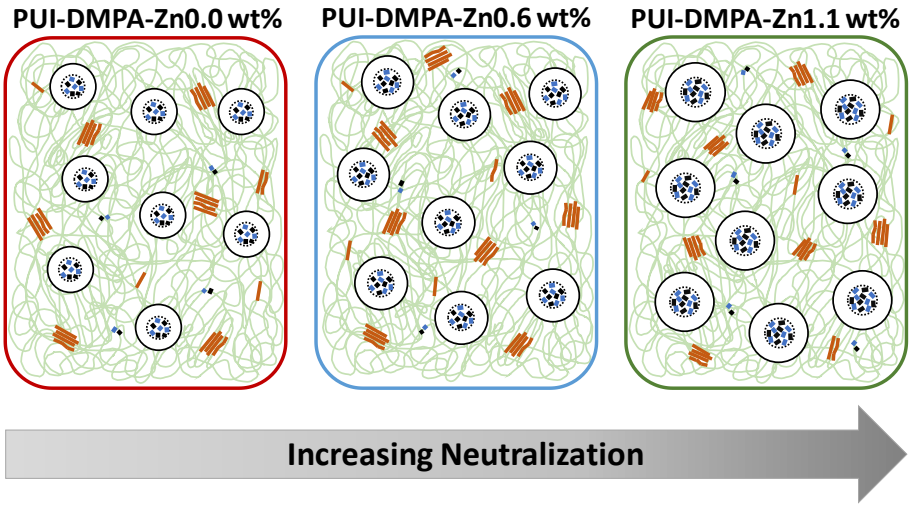

Figure 4.9 Schematic illustration of the ionic aggregation structure in PUIs.

4.4 Conclusions

The cycloaliphatic diisocyanate-based PUIs bearing carboxylic acid groups was successfully synthesized with the different zinc content. The neutralization of these acid groups with metal salts contributes to the ionic aggregation structure. Increasing degree of neutralization resulted in the larger ionic aggregates and improvement of the phase separation, which in turn enhance the mechanical properties of PU ionomers.

References

4-1) S. Hsu, H. Xiao, H. Szmant, K. Frisch, *J. Appl. Polym. Sci.*, **29**, 2467-2479, (1984).

4-2) "Advances in urethane ionomers", K.C. Frisch, H. Xiao, Technomic Publishing, Lancaster, (1995).

4-3) B.K. Kim, Y.M. Lee, *J. Macromol. Sci., Pure Appl. Chem.*, **29**, 1207-1221, (1992).

4-4) R.B. Dickinson, J.A. Nagel, R.A. Proctor, S.L. Cooper, *J. Biomed. Mater. Res.*, **36**, 152-162, (1997).

4-5) P. Król, B. Król, L. Subocz, P. Andruszkiewicz, *Colloid. Polym. Sci.*, **285**, 177-183, (2006).

4-6) G. Polizos, G. Georgoussis, A. Kyritsis, V.V. Shilov, V.V. Shevchenko, Y.P. Gomza, S.D. Nesin, N.S. Klimenko, S. Wartewig, P. Pissis, *Polym. Int.*, **49**, 987-992, (2000).

4-7) V. Shilov, V. Shevchenko, P. Pissis, A. Kyritsis, G. Georgoussis, Y.P. Gomza, S. Nesin, N. Klimenko, *Mol. Crys. Liq. Crys. Sci. Tech. Mol. Cryst. Liq. Cryst.*, **361**, 269-274, (2001).

4-8) A. Eisenberg, *Macromolecules*, **3**, 147-154, (1970).

4-9) Y.S. Ding, R.A. Register, C.-z. Yang, S.L. Cooper, *Polymer*, **30**, 1221-1226, (1989).

4-10) Y.S. Ding, R.A. Register, C.-z. Yang, S.L. Cooper, *Polymer*, **30**, 1204-1212, (1989).

4-11) H.S. Xu, C.Z. Yang, *J. Polym. Sci., Part B: Polym. Phys.*, **33**, 745-751, (1995).

4-12) H. Masunaga, H. Ogawa, T. Takano, S. Sasaki, S. Goto, T. Tanaka, T. Seike, S. Takahashi, K. Takeshita, N. Nariyama, H. Ohashi, T. Ohata, Y. Furukawa, T. Matsushita, Y. Ishizawa, N. Yagi, M. Takata, H. Kitamura, K. Sakurai, K. Tashiro, A. Takahara, Y. Amamiya, K. Horie, M. Takenaka, T. Kanaya, H. Jinnai, H. Okuda, I. Akiba, I. Takahashi, K. Yamamoto, M. Hikosaka, S. Sakurai, Y. Shinohara, A. Okada, Y. Sugihara, *Polym. J.*, **43**, 471-477, (2011).

4-13) K. Kojio, K. Matsuo, S. Motokucho, K. Yoshinaga, Y.

Shimodaira, K. Kimura, *Polym. J.*, **43**, 692-699, (2011).
4-14) K. Hwang, T. Speckhard, S.L. Cooper, *J. Macromol. Sci., Phys.*, **23**, 153-174, (1984).
4-15) M.M. Coleman, J.Y. Lee, P.C. Painter, *Macromolecules*, **23**, 2339-2345, (1990).
4-16) E. Andreeva, V. Nikitin, Y.M. Boyartchuk, *Macromolecules*, **9**, 238-243, (1976).
4-17) T. Speckhard, K. Hwang, C. Yang, W. Laupan, S.L. Cooper, *J. Macromol. Sci., Phys.*, **23**, 175-199, (1984).
4-18) D.J. Yarusso, S.L. Cooper, *Macromolecules*, **16**, 1871-1880, (1983).
4-19) J.J. Moré, The Levenberg-Marquardt algorithm: implementation and theory. In Numerical analysis, Springer, 105-116, (1978).
4-20) R.C. Team, R: A language and environment for statistical computing. R Foundation for Statistical Computing, Vienna, Austria. 2012. URL http://www. R-project. org (2018).
4-21) A. Takahara, J. Tashita, T. Kajiyama, M. Takayanagi, *J. Biomed. Mater. Res.*, **19**, 13-34, (1985).
4-22) D.S. Huh, S.L. Cooper, *Polym. Eng. Sci.*, **11**, 369-376, (1971).
4-23) K.K. Hwang, C.Z. Yang, S.L. Cooper, *Polym. Eng. Sci.*, **21**, 1027-1036, (1981).

Chapter 5

Conclusions

The strong relationship between the microphase-separated structure and mechanical properties of polythiourethanes, polyurethanes, and polyurethane ionomers has become the subject of long-running discussion within the researchers. This paper aimed to contribute to the literature by using the cycloaliphatic diisocyanate-based polyurethane family as a proxy. For this purpose, this paper conducted an investigation of microphase-separated structure which involved static and dynamic state. Additionally, this paper also performed an analysis of structure-property relationship in polyurethane ionomers bearing carboxylic acid as a case study for ionic polymers. The results from this study are summarized as follows:

- PTU elastomers showed a stronger degree of microphase separation and less domain mixing in comparison with PUs. As a result, PTU showed a better low-temperature property for the soft segment chain. However, the ordering of the hard segment domains in the PTUs is lower than that for the PUs, resulting in a mechanical property for PTUs that is comparable with PUs.

- Elastomers with a PD-based chain extender exhibited a lower degree of microphase-separated structure and mechanical property in comparison with elastomers with a BD-based

chain extender. In addition, the influence of the methylene length of the chain extender on the microphase-separated structure and mechanical properties for PU is much stronger than that for PTU.

- During elongation process, the ordering of hard segment chains occurred and then strain-induced crystallization of the soft segments subsequently occurred. The SAXS measurement revealed that the spacing of hard segment domains of PTUs increased in the directions of parallel to elongation direction and showed constant value above strain of 2. The strain obtained from the spacing of the hard segment domains for PTU-B was larger than for PTU-P, and Young's modulus and tensile strength of PTU-B were larger than for PTU-P, suggesting that well-developed hard segment domains were formed for PTU-B. The crystalline peaks were observed along perpendicular direction to elongation direction in WAXD patterns and Debye-Waller factor decreased at around strain of 2-3.

- The neutralization of the carboxylic acid groups with zinc salts contributes to the ionic aggregation structure in PU ionomers. Increasing degree of neutralization resulted in the larger ionic aggregates and improvement of the phase

separation, which in turn enhance the mechanical properties of PU ionomers.

The discussion about the relationship between microphase-separated structure and mechanical properties of PTUs, PUs, and PUIs reveals important implications for molecular structure design of PU family for various applications.

ACKNOWLEDGEMENTS

With utmost sincerity and pleasure, I would like to express my profound gratitude to my advisor Prof. Atsushi Takahara for his active guidance, positive encouragement and continuous support during my doctoral study. His guidance helped me in all the time of research and writing of this thesis. Besides being an excellent academic supervisor he is also a good life tutor who has taught me a great deal about both academic and life in general. My doctoral life has been an amazing experience and it has been a great honor for me to become the part of his laboratory.

A very special gratitude also goes out to the Ministry of Research, Technology, and Higher Education of Indonesia for providing the scholarship and financial support through the Research and Innovation in Science and Technology Project (RISET-PRO). I am also indebted to the tremendous support from my office, the National Nuclear Energy Agency of Indonesia (BATAN), particularly to my supervisors and colleagues at the Center for Isotope and Radiation Application. This thesis is dedicated to support the development and further utilization of radiation in polymer science in Indonesia.

I would also like to extend thanks to all of those with whom I have had the pleasure to work during my doctoral study. I would like to acknowledge associate professor Ken Kojio for his kind support and assistance. I would also like to acknowledge the support from Takahara's Laboratory past and present assistance professor: Yuji Higaki, Tomoyasu Hirai, Masaru Mukai, Yoshifumi Amamoto, and Keisuke Matsuno. I am also hugely

appreciative to my co-authors Shuhei Nozaki, Shiori Masuda, Chao-Hung Cheng, Chigusa Nagano, and Kazutaka Kamitani. Special mention goes to the past and present members of Takahara's Laboratory that I have had the pleasure to work with: Nattanee Dechnarong, Zhang Yucheng, Li Linlin, Shiki Nojima, Wei Ma, Masanao Sato, Kaetsu Katsuhiro, Yudai Kiyoshima, Yusuke Nagae, Makoto Kido, Di Tao, Kyung-Lin Park, Naoki Okawa, Haruki Ichioka, Kento Fukada, Nobuhisa Takayama, Sakamaki, Shimamoto, Kato, Inutsuka. The kind supports received from Aiko Miyamoto, Motoko Teranishi, Keiko Higaki, Miki Shoiriki, Reiko Iki, Kubozono, Saburo Yamamoto, Tomoko Kajiwara, Aya Fujimoto, Kazutoshi Yokomachi, Mayumi Mizuta, Akiko Mitarai, Akiko Ishibasi, Michiyo Matsuura are also appreciated.

I would like to thank the members of my dissertation committee, Prof. Keiji Tanaka and Prof. Tsuyohiko Fujigaya for generously offering their time, support and guidance to this thesis. Their valuable comments greatly improved the quality of this thesis.

Nobody has been more important to me than my family. I would like to thank my parents for their endless love and prayers that always with me in whatever I pursue. Most importantly, I wish to thank my loving and supportive husband, Yogi Sugiawan, and my two wonderful sons, Fauzan and Fahmi, for their patience and emotional support. I am also grateful to my other family members and friends who have supported me along the way.